Heat Pipe technology based Divertor Plasma Facing Component concept for European DEMO

Zur Erlangung des akademischen Grades einer

DOKTORIN DER INGENIEURWISSENSCHAFTEN (Dr.-Ing.)

von der KIT-Fakultät für Maschinenbau des
Karlsruher Institut für Technologie (KIT)

genehmigte

DISSERTATION

von

M.Sc. Wen Wen

Hauptreferent: Prof. Dr.-Ing Xu Cheng
Korreferent: Prof. Dr.-Ing Jörg Starflinger

Tag der mündlichen Prüfung: 29.05.2024

Abstract

Heat pipes effectively transport heat from a heat source to a heat sink using capillary forces and a phase change of the internal working fluid. Due to their exceptional thermal conductivity, they are considered for plasma-facing components of DEMO fusion reactors, especially the divertor that removes impurities from the fusion process and must withstand a maximum heat flux of up to 20 MW/m^2. Compared to a current-cooled divertor target, using the heat pipe can enlarge the heat transfer area to the cooling circuit and enhance the reactor's safety.

A DEMO divertor target with water-based heat pipe (DIV-HP) that can transport heat fluxes up to 20 MW/m^2 is designed with mixed capillary structures according to a engineering analysis model. To validate the design of the DIV-HP on an unclear boiling limit, a experiment of the Heat Pipe for Evaluating the Evaporator (HPEE) is created, by using the same design approaches.

This experiment investigates the performance of HPEEs by analyzing the temperature measurements and the calorimetric heat flux transported through the HPEEs. Two mock-ups with different capillary porous evaporators are compared to evaluate the potential for improving the performance of HPEE evaporators. Additionally, the influence of liquid inventories and heat sink flow rates on the performance of HPEE evaporators is studied. The results of the experiment are then compared with the predicted value of the HPEE engineering analysis model.

The experimental results show that HPEEs with 2.0 ml of liquid inventory, particularly one with porous evaporator constructions with channels, can perform well up to 4.3 MW/m^2 with an evaporator temperature of 275 °C. The experiment has been stopped at this value because the heat source has reached its maximum operating temperature. HPEEs show the potential to transport a higher heat flux as there is no sign of dry-out. The average temperature of the evaporator measured in the experiment is much lower than the one estimated by the HPEE analysis model, suggesting that the actual performance of the HPEE is better than what the analysis model predicted.

These findings provide guidelines for the divertor heat pipe design using the same analysis model. It is concluded that the design of the divertor heat pipe is capable of operating at 20 MW/m^2. The performance of the divertor heat pipe can be improved by ensuring the right amount of liquid and optimizing the porous structure. Therefore, it offers a promising outlook for the use of water-heat pipes in DEMO divertor applications, or even in other high heat flux conditions.

Kurzfassung

Wärmerohre transportieren effektiv Wärme von einer Wärmequelle zu einer Wärmesenke unter Verwendung von Kapillarkräften und einem Phasenwechsel des internen Arbeitsfluids. Aufgrund ihrer außergewöhnlichen thermischen Leitfähigkeit werden sie für die Kühlung von plasma-nahen Komponenten des DEMO-Fusionsreaktors in Betracht gezogen, insbesondere für den Divertor, der Verunreinigungen aus dem Plasma entfernt, und mit einer maximalen Wärmestromdichte von bis zu 20 MW/m^2 belastet ist. Im Vergleich zum aktuellen Design der Divertor-Prallplatten kann die Verwendung von Wärmerohren die Wärmeübertragungsfläche zum Kühlkreislauf vergrößern und die Sicherheit des Reaktors verbessern.

Eine DEMO-Divertorprallplatte mit wasserbasiertem Wärmerohr (DIV-HP), die Wärmestromdichten bis zu 20 MW/m^2 mit gemischten kapillaren Strukturen transportieren kann, wird gemäß einem ingenieurtechnischen Analysemodell entworfen. Um das Design des Divertor-Wärmerohrs bei einer unklaren Siedegrenze zu validieren, wird unter Verwendung derselben Designansätze ein spezielles Experiment („Heat Pipe for Evaluating the Evaporator“, HPEE), aufgebaut.

In diesem Experiment wird die Leistung der HPEEs durch die Analyse von Temperaturmessungen und der kalorimetrischen Wärmestromdichte, die durch die HPEEs transportiert wird, untersucht. Es werden zwei Modelle mit verschiedenen kapillarporösen Verdampfern miteinander verglichen, um das Potenzial zur Verbesserung der Leistung von HPEE-Verdampfern zu bewerten. Zusätzlich wird der Einfluss des Flüssigkeitsinventars und der Durchflussraten der Wärmesenke auf die Leistung der HPEE-Verdampfer untersucht. Die Ergebnisse des Experiments werden anschließend mit den vorhergesagten Werten des HPEE-Engineering-Analysemodells verglichen.

Die experimentellen Ergebnisse zeigen, dass HPEEs mit einem Flüssigkeitsinventar von 2,0 ml, insbesondere solche mit porösen Verdampferkonstruktionen mit Kanälen, bis zu einer Wärmestromdichte von 4,3 MW/m^2 bei einer Verdampfertemperatur von 275 °C gut funktionieren. Das Experiment muss bei diesem Wert beendet werden, da die Wärmequelle ihre maximale Betriebstemperatur erreicht. HPEEs haben das Potenzial, eine höhere Wärmestromdichte zu transportieren, da keine Anzeichen für Trockenlauf vorliegen. Die durchschnittliche Temperatur

des Verdampfers, die im Experiment gemessen wird, ist signifikant niedriger als die vom HPEE-Analysemodell geschätzte, was darauf hinweist, dass die tatsächliche Leistung der HPEE besser ist als vom Analysemodell vorhergesagt.

Diese Erkenntnisse bieten Leitlinien für das Design von Divertor-Wärmerohren unter Verwendung desselben Analysemodells. Es wird geschlussfolgert, dass das Design des Divertor-Wärmerohrs in der Lage ist, bei 20 MW/m^2 zu arbeiten. Die Leistung des Divertor-Wärmerohrs kann durch Gewährleistung des richtigen Flüssigkeitsinventars und Optimierung der porösen Struktur verbessert werden. Der Ausblick auf den Einsatz von Wasser-Wärmerohren im DEMO-Divertor oder in anderen Anwendungen mit hoher Wärmestromdichte ist vielversprechend.

Contents

Acronyms

Symbol	Descriptions	Units
A	Surface Area	mm^2
d	Diameter	mm
D	The inner diameter of jet	mm
h	Specific enthalpy	J/kg
H	Distance between jet and bottom of FHP l jet to the condenser	mm
l	Length	mm
Lt	Jet-to-jet distance	mm
$\dot{m}$	Mass flow rate of coolant	kg/s
N	Number	
p	Pressure	Pa
P	Power	W
Q	Heat flux	W/m^2
r	Radius	mm
R	Thermal resistance	K/W
t	Time	s
T	Temperature	°C
u	Uncertainty	
U	Relative uncertainty	
v	Velocity	m/s
V	Volume	m^3
$\dot{V}$	Volume flow rate	l/h
w	Width	mm
Greek symbols		
α	Heat transfer coefficient (HTC)	W/m^2
β	Inclination angle	°
δ	Thickness	mm
Δ	Difference	-

Symbol	Descriptions	Units
η	Dynamic viscosity	Pa·s
ν	Kinematic viscosity	m^2/s
θ	The wetting angle	$^\circ$
λ	The specific thermal conductivity	W/(m·K)
ξ	Depth	mm
ρ	Density	Kg/m^3
σ	The surface tension	N/m
ϕ	Porosity	%
Numbers		
Nu	Nusselt number	
Pr	Prandtl number	
Re	Reynolds number	
Subscriptions		
$adia$	Adiabatic of the Heat Pipe	
ave	Average value	
b	Vapor nucleus of boiling	
$base$	Baseline coolant system	
$bundle$	Staggered arrangement Pipe bundles	
c	Capillary structure	
ch	Channel	
$cond$	Condenser of the Heat Pipe	
$crit$	Critical value	
cy	Cylinder part	
e	Environment	
eff	Effective value	
en	Envelope	
$evap$	Evaporator of the Heat Pipe	
g	Grooves	
i	Inner	
in	Inlet	
J	Jet	
l	Liquid	
lam	Laminar flow	

Symbol	Descriptions	Units
m	Mesh	
max	Maximum value	
min	Minimum value	
n	Nozzle	
o	Outer	
opt	Optimal value	
out	Outlet	
po	Particle of sintered porous	
pp	Sintered porous plate	
$stag$	Staggered arrangement	
Tur	Turbulence flow	
u	Uncertainty	
v	Vapor	
$W - cap$	Tungstun(W) Hexagonal cap	
Abbreviations		
CHF	Critical Heat Flux	
DIV	Divertor	
HEMJ	Helium-cooled modular concept with jet cooling	
HHF	High Heat Fluxes	
HP	Heat Pipe	
HPEE	Heat Pipe for Evaluating Evaporator	
HTC	Heat Transfer Coefficient	
HTCH	Heat Transfer Characteristic	
IVT	Inboard Vertical Target	
OVT	Outboard Vertical Target	

1 Introduction

1.1 Energy Production Option of Fusion

Fusion energy is presently regarded as one of the essential low-carbon development pathways, clean and sustainable. According to energy models, after the Uranium resources are exhausted, fission technologies will be replaced by fusion power plants that begin in 2070 and contribute significantly to global electricity production by 2100 [Cabal et al. 2012]. Furthermore, when producing the same amount of power, the generation of fusion power will require less land than photovoltaic and wind power plants [Bustreo et al. 2019], and unlike these two power plants, a fusion reactor is capable of producing high-power energy and hydrogen directly by high-temperature steam electrolysis [Gi et al. 2020].

To this end, the International Thermonuclear Experimental Reactor (ITER) is being constructed as a preliminary step towards producing plasma suitable for fusion power plants [Bigot 2022], which concentrates on plasma with limited objectives.

Therefore, the EUROfusion Power Plant Physics & Technology (PPPT) Work Programme seeks to bridge the gap between ITER and the first commercial plant by finishing the fusion reactor design. It is planning to construct a demonstration power station, known as DEMO, based on the experience gained from the ITER project. This power station will be used to assess the safety, environmental friendliness, and economic feasibility of potential commercial fusion projects [Matsuda and Tobita 2013] [Federici et al. 2016].

Based on the ITER concept, the higher quality design is to be improved for DEMO [Romanelli 2012]. First, DEMO is designed to provide the power grid with hundreds of megawatts of electricity. In contrast to ITER, which works with short plasma pulses that last around five minutes, DEMO needs two to four hours or even continuous plasma operation.

Therefore, the design of a heat exhaust system to address extremely high heat flux is a major focus of the DEMO reactor development. The heat exhaust system is accomplished by the utilization of the main chamber wall and the divertor region. The divertor, one of the components, is designed to properly handle heat exhaust, withstand high temperatures and particle flows in fusion power plants, and allow the core plasma to function with maximum efficiency.

1.2 The Functionality & Challenges of the DEMO Fusion Reactor Divertor

The current baseline DEMO divertor [Bonavolontà et al. 2020][Mazzone et al. 2020] sits in the lower region of the vacuum vessel, as in Figure 1.1 (a). It absorbs the fusion energy and impurities, reducing plasma pollution, and shields the nearby walls from thermal and neutron loads. In addition to a uniform loading of around 1 MW/m^2 on the targets due to plasma radiation, when plasma particles move through the scrape-off layer (SOL) and collide with the target surface, the thermal power density is concentrated on a band (strike point) of the targets due to the short characteristic power decay length of the SOL, causing a local peak in the heat flux density, as high as 10 to 15 MW/m^2. These high-power plasma particles must be continuously exhausted at the targets by active cooling to enable long-pulse operation.

The baseline DEMO Divertor referenced 2019 CAD model [Eurofusion 2019] is divided into 16 toroidal sectors associated with a lower port through which the feed pipeline is routed. Each sector equally comprises a set of three cassette modules (one central cassette and two side cassettes), 48 cassette modules arrayed symmetrically along the toroidal orientation. Each cassette is approximately 4 m long and 2 m high with a width of 0.7 to 1.2 m according to the toroidal diameter [You et al. 2022].

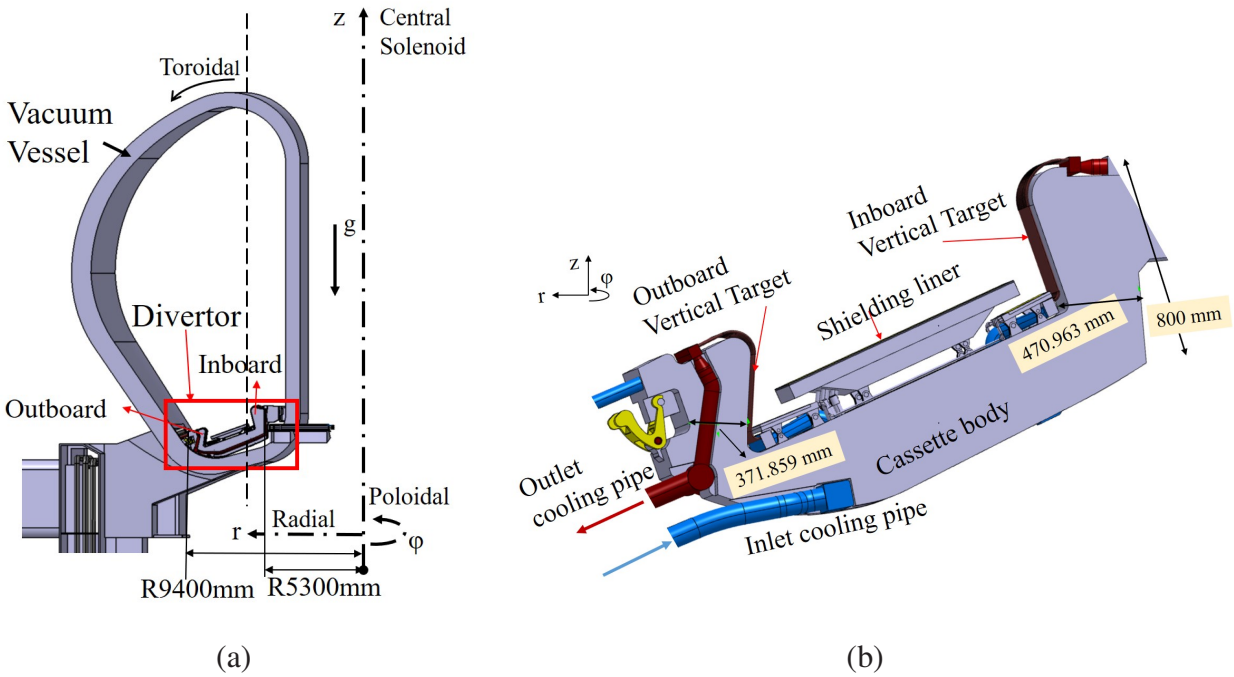

Figure 1.1: DEMO divertor referenced the 2019 CAD model [Eurofusion 2019] (a) position in the vacuum vessel, (b) clear view with measured dimensions of the thinnest areas in the outboard and inboard target regions.

Each cassette module comprises the following components, shown in Figure 1.1 (b):

- Two target plates: Inboard Vertical Target (IVT) and Outboard Vertical Target (OVT), blocking the plasma particles flowing in the scrape-off layer (SOL).
- The cassette body (CB), of which the structural material is ferritic steel EUROFER97 (E97), holds the targets and other shielding components
- Shielding components (shielding liner and reflector plates) that protect the vacuum vessel (VV) and pipes.
- Pipework of the cooling circuits.

1.3 Divertor Cooling Options

Based on the ITER-adopted solution, the DEMO baseline divertor has water-cooled targets operating at a coolant temperature below 150 °C, as shown in Figure 1.2. Each target consists of many parallel longitudinal arrays of rectangular tungsten armor monoblocks joined to a long water-cooling pipe (CuCrZr alloy) running through the center bore of the blocks as the heat sink. A swirl flow is produced by inserting a twist tap into the pipe to increase the heat transfer coefficient. However, due to special plasma-facing working environments, the baseline target is still being developed to improve the high temperature strength and corrosion resistance of water-cooled heat sinks by studying composite materials and improved structure [You et al. 2016][You et al. 2018].

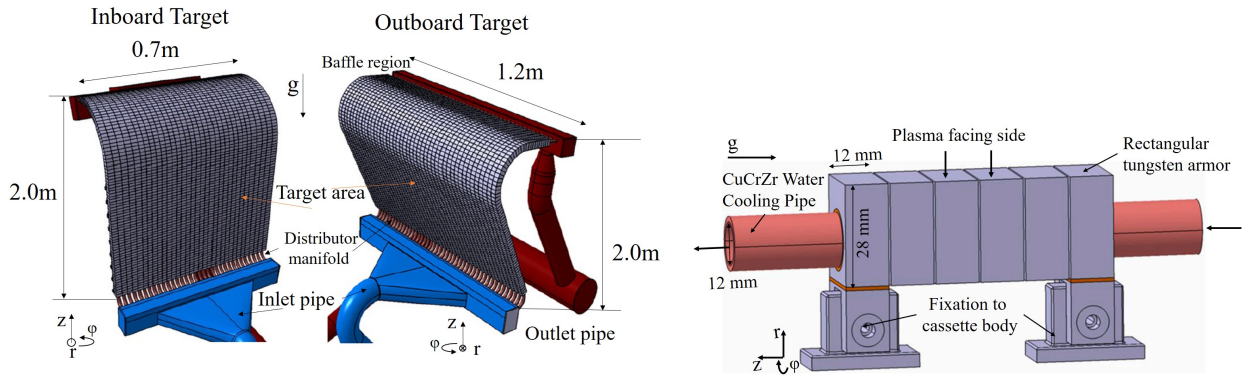

(a) (b)

Figure 1.2: DEMO divertor baseline water-cooled targets [You et al. 2022] (a) arrangement for inboard and outboard targets, (b) one coolant tube with rectangular tungsten armor monoblocks.

In addition to the baseline water-cooled target, another low-temperature water-cooled target with hypervapotrons [Raffray et al. 1999] and a high-temperature coolant operation with helium-cooled modular concept with jet cooling (coolant: >500 °C) HEMJ-finger targets [Bonavolontà et al. 2020] are also being considered. However, all three coolant targets are based on the cooling channels embedded into the constrained plasma-facing wall with a tungsten armor. Therefore, when heat flux is applied from one side of the cooling channel (plasma-facing side), the heat transfer area to the external coolant is limited to a small portion of the pipe circumference, reducing the cooling efficiency. These options connect the external coolant system directly, allowing the coolant to flow through their cooling tubes. When target plasma-facing side is broken, all the water from the external cooling system enters the vacuum chamber via the baseline target cooling tube.

Over the years, to overcome the limitations of the baseline cooling solution, researchers have shown increasing interest in the design of alternative cooling targets. Heat pipes (HP) as passive two-phase capillary-driven devices with high capacity for heat transport are considered as an option. It is a closed system divided from the external cooling system that offers flexibility in changing the target structure of the heat pipe and expanding the heat transfer region.

Heat pipe typically consists of three primary components: an evaporator (where the heat load from the heat source is applied), an adiabatic section, and a condenser (where the heat is transmitted to the heat sink or the external cooling system). The heat pipe's envelope contains the capillary structure and working liquid, which creates a sealed chamber. The two-phase flow's evaporation and condensation transfer heat received from the evaporator through the condenser to the external coolant, giving them a highly effective thermal conductivity far superior to that of any metal.

The heat pipes, as closed systems, sit between the plasma-facing chamber and the external coolant system. When the heat pipe target is broken, only a small amount of water from the broken heat pipe leaks into the vacuum chamber. The integrity of the coolant circuit is not affected, preventing the continuous external coolant from entering the inner vacuum chamber of the fusion reactor. This reduces the damage caused when the target plasma-facing side breaks. Heat pipes can transfer heat over a great distance with a long condenser length, which also increases the contact cooling area with the external cooling system.

The use of heat pipes in plasma-facing components has already been studied, particularly with liquid metal as a working liquid for high-temperature applications, such as lithium [Rosenfeld and Lindemuth 1993]. Kovalenko [Kovalenko et al. 1995] suggested potassium HP and water HP to stabilize the temperature of the first wall with different requirements. Carlson [Carlson and Hoffman 1972] and Schwertz [Schwertz and Hoffman 1983] analyzed the possibility of using a liquid metal heat pipe to cool a pool of liquid lithium in the blanket of a tandem mirror fusion reactor. However, Makhankov [Makhankov et al. 1998] found that the transverse magnetic field can profoundly affect the performance capability of liquid metal heat pipes.

Water-based heat pipes were considered to handle heat fluxes as high as 2 MW/m^2 for fusion applications [Rosenfeld and Lindemuth 1993]. However, due to the limitation of the heater's capabilities, the maximum radial heat flux reached is 0.525 MW/m^2. As a result, an operating limit was never reached on the water heat pipes.

Liquid metal as the working fluid in heat pipes can transport high heat flux in fusion applications, but the magnetic field impact on the heat pipes' operation needs to be further analyzed. The water heat pipe is perceived to be safer to utilize in the fusion reactor. Due to the lack of research on the use of heat pipes in the DEMO divertor and the uncertain performance of water heat pipes under high heat flux conditions, the water-based divertor heat pipe is investigated in this dissertation.

1.4 Objectives of the Dissertation: Using Heat Hipe as a DEMO Divertor Target

This dissertation reports on the investigation of the use of a water-based heat pipe for divertor targets and their capability to remove high heat fluxes in a relatively low operating temperature range. This is the first research to study the feasibility of using the water-based heat pipe in high heat flux conditions, such as in a fusion reactor, and to identify optimization possibilities.

A specific divertor heat pipe that can be incorporated into the existing divertor cassette configuration with minimal modifications is initially designed and is capable of effectively transferring a high heat flux of approximately 20 MW/m^2.

According to the divertor heat pipe design, an in-depth analysis of the critical issues of the heat pipe, such as capillary and boiling limits, is planned using an experiment before delving into the DEMO diverter's heat pipe performance analysis. As a result, an experimental heat pipe mock-up is initially constructed and evaluated, based on the same engineering analysis design approaches as the divertor heat pipe. It focuses on the performance of the evaporator, which is significantly affected by critical issues. The engineering analysis model is built in the meantime to predict the performance of the experimental heat pipe mock-up.

Potential heat-pipe evaporator structures are examined to look into ways to enhance the heat-pipe's heat transfer capability. Apart from the structural aspects, research is conducted on how the liquid inventory and the heat sink's heat transfer coefficient impact the heat pipe's performance by analyzing temperature measurements and calorimetric heat flux transported.

Finally, a comparison is made between the experimental heat pipe results and the expected findings of the engineering analysis model. The outcomes can be utilized to evaluate the divertor heat pipe design and engineering analysis model's accuracy and viability, for future upgrades.

1.5 Structure of Thesis

This Introduction provides the related information of DEMO divertor, regarding to the objectives of using heat pipe in the divertor target. Chapter 2 introduces the specific divertor heat pipe design, which is based on the principle of the heat pipe design methodology and the DEMO divertor structure and coolant requirements. To validate the design, Chapter 3 examines the experiment with two heat pipe mock-ups, with the aim of evaluating and enhancing the performance of the divertor heat pipe evaporator. Additionally, the engineering analysis model is constructed. The data processing technique and uncertainty analysis are explained with a particular focus on the calorimetric power evaluation. Chapter 4 presents the results and a discussion of the influences of various evaporator structures, liquid inventories, and coolant flow rates in the heat sink on the performance of the heat pipe. Then, the temperature measurements in the experiments are compared with the value of the engineering analysis model. Chapter 5 concludes the work of this dissertation and points out the possible directions for future investigation.

2 Heat Pipe Design for DEMO Divertor Target (DIV-HP)

Taking advantage of the heat pipes' effective heat transport capability and safety features, the potential of using specific water-based heat pipes concepts for the DEMO divertor target, which refers to DIV-HP in the following discussion, is investigated. As a starting point, the principal functionality and operational considerations of a heat pipe are theoretically introduced based on the engineering technique. Then, the geometry of the cassette (version 2019) [Eurofusion 2019] and the target cooling conditions of the divertor are taken as boundary conditions of the DIV-HP design to ensure minimal changes to the baseline divertor cassettes and the target cooling. The final concepts of the divertor heat pipe are focused on the aforementioned conditions.

2.1 Principal Functionality of a Heat Hipe

The heat pipe is a heat transfer system typically based on closed two-phase (liquid-vapor) flow systems. It is a closed fluid container, as shown in Figure 2.1. The capillary structure that lines the interior of the closed container envelope is filled with liquid. The liquid at the heated end evaporates and partially retracts into the capillary structure. The vapor that is produced moves to the cold end of the container, where it condenses and fills the capillary structure. The capillary force draws the condensed liquid back to the evaporator. Thus, the two-phase loop is closed, transferring the latent heat from the evaporator near the heat source to the condenser near the heat sink. The adiabatic part is located between the evaporator and the condenser.

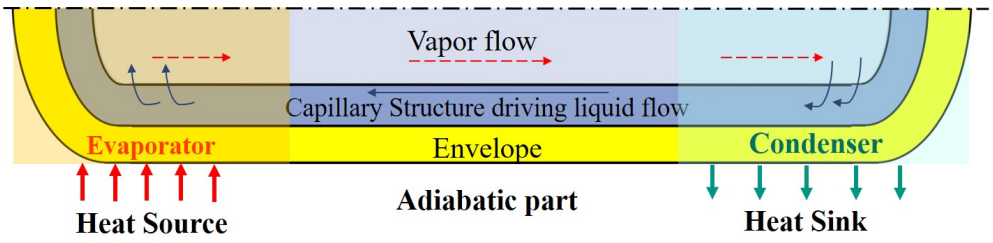

Figure 2.1: Principle functionality of a heat pipe.

The heat pipe has a high heat transport capability between heat sources and sinks while experiencing minimal temperature variation. The effective thermal conductivity can exceed the thermal conductivity of pure material by almost two orders of magnitude. Thanks to the capillary force, the condensed liquid can be moved in a way that isn't affected by gravity, or even against it. Fluid movement doesn't depend on moving parts and doesn't show any signs of wear, so it doesn't need any upkeep. Because of these features, it is possible to build a low-mass, small heat exchanger design, and the shapes can be very complicated.

For the heat pipe to have a circulated flow, the capillary structures should create high capillary pressure in the evaporator area. Along the main flow direction, there should be low resistance to liquid flow or pressure drop. In order to keep the capillary system from getting blocked, the structure is in sensitive to the generation and growth of vapor bubbles. And the shape of the capillaries should be able to hold a lot of liquid. Therefore, the selection of the capillary structure needs conciliation. Additionally, it is possible to have a complex one by mixing different types of capillary structures.

The most common capillary structures used in conjunction with the heat pipes are shown in Figure 2.2:

- Mesh/wick has the most uniform wick and high capillary pressure, so it works against gravity orientations when the evaporator is above the condenser.
- Sintered porous metal can handle high capillary pressure and works best when it's not facing gravity. Because it is metallically attached to the pipe wall, it is the best at moving heat from the pipe wall to the wick or the other way around.
- Grooves have the lowest capillary pressure, but they work best when the condenser is above the evaporator and gravity is helping the flow because they have a low flow resistance.

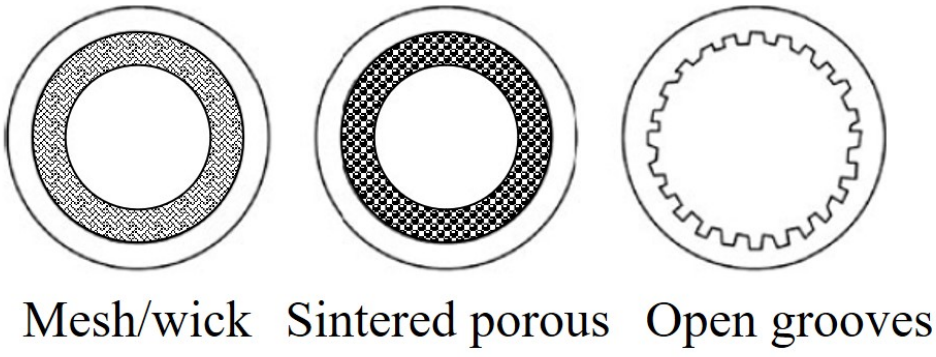

Figure 2.2: Commonly used capillary structures in heat Pipe design [Stephan 2010].

The mesh/wick and sintered porous structures have drawbacks in the form of high liquid flow resistance and are sensitive to vapor bubble production. While bubbles generated in the open grooves can move out to the vapor core.

Figure 2.3 shows the parameter that is considered when dimensionalizing a heat pipe. Besides the diameter of the envelope, capillary structure, and vapor space, the length of each heat pipe section is also important.

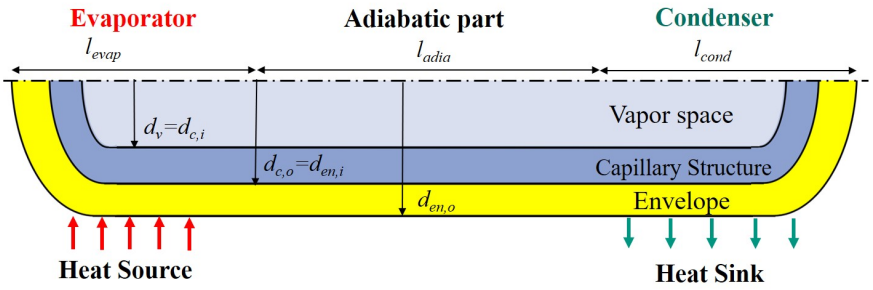

Figure 2.3: Dimension parameters for heat pipe design.

The parameters are listed in Table 2.3 are:

Table 2.1: Parameters of a heat pipe.

Parameters	**Description**
$d_{en,o}$	Outer diameter of the heat pipe envelope
$d_{en,i}$	Inner diameter of the heat pipe envelope
$d_{c,o}$	Outer diameter of the heat pipe capillary structure
$d_{c,i}$	Inner diameter of the heat pipe capillary structure
d_v	Diameter of the heat pipe vapor space
d_{evap}	Length of the heat pipe evaporator
d_{adia}	Length of the heat pipe adiabatic section
d_{cond}	Length of the heat pipe condenser

To find the right heat pipe material under different requirements, the heat pipe working fluid selection depends on the merit number, defined as $\mathrm{M} = \frac{\sigma \cdot \Delta h_v}{\nu_l}$ with a unit $\mathrm{W/m^2}$ or $\mathrm{kW/cm^2}$ [Stephan 2010]. It expresses that the heat pipe working fluid should have high latent heat of vaporization Δh_v, low viscosity ν_l, high surface tension σ, and usually high thermal conductivity and neither extremely low nor extremely high vapor pressure at the given operating temperature.

According to the merit number shown in Figure 2.4, the typical working liquids used in the heat pipes are different for a given application with a specified operating temperature range. The peak value of each curve indicates the fluid's optimal working temperature.

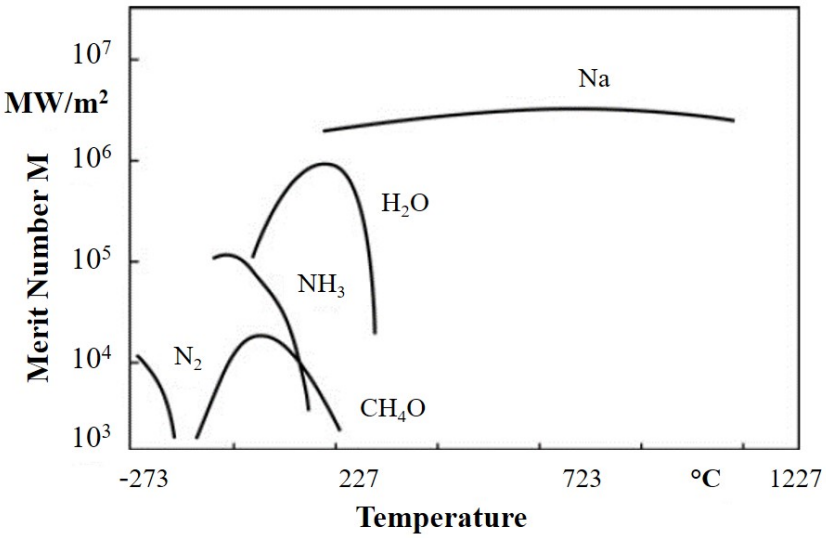

Figure 2.4: Figure of the Merit of the heat pipe working fluid (From Chapter N5 of the book Heat Atlas [Stephan 2010].

The selection of solid material for the container wall and capillary structure is determined by the heat conductivity, which should be significantly elevated. Meanwhile, the interaction between the solid and the fluid is also of utmost importance. The solid material must have excellent wetting characteristics and chemical stability in order to effectively avoid corrosion and the generation of non-condensable gases that may impede the functioning of the condenser area. Compatibility is also influenced by the production and post-cleaning procedures.

The choice of the combination of capillary structure/fluid/wall material, as well as the heat pipe dimension, is determined by computing the design's performance limits and comparing them to the performance criteria.

2.2 Operational Considerations of a Heat Pipe

Two main approaches to analyzing the heat transport capabilities of the heat pipes are based on the effective heat resistance and performance limits. After knowing the effective heat resistance, the working temperature of each heat pipe's sections is estimated when the heat flux is applied. Performance limitations, which take into account the size and construction of the heat pipe in various circumstances, assist in calculating the maximum heat flux the heat pipe can sustain.

Heat pipes can be considered as thermal conductors with effective heat resistance R_{HP} in [K/W]. The temperature difference between the evaporator and the condenser follows $\Delta T_{evap-cond} = P \cdot R_{HP}$. Figure 2.5 shows the simplified heat resistance model of the heat pipe system [Stephan 2010], with single heat resistances R_i acting as parallel or serial in the overall circuit.

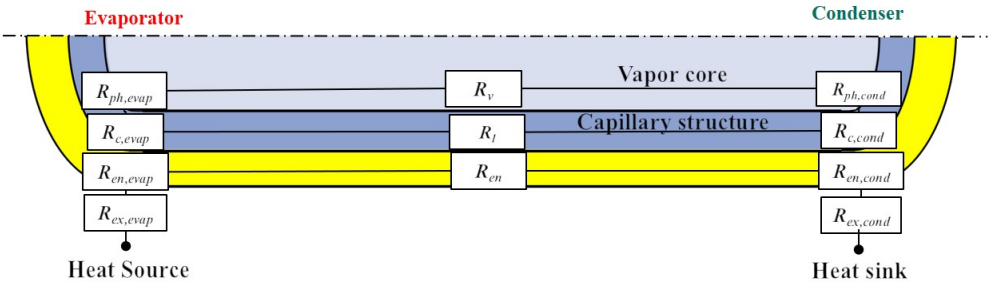

Figure 2.5: Effective heat resistances R_i in [K/W] in a heat pipe.

The single resistances listed in Table 2.2 are:

Table 2.2: Individual heat resistances with order of magnitude according to Asselman and Dreen [37].

Heat resistances	**Description**	**Magnitude [K/W]**
$R_{ex,evap}$	Radial heat resistance between the external heat source and outer evaporator wall	$> 10^{+1}$
$R_{en,evap}$	Radial heat resistance of the evaporator envelope	10^{-1}
$R_{c,evap}$	Radial heat resistance of the capillary structure in the evaporator	10^{+1}
$R_{ph,evap}$	Radial heat resistance of the liquid-vapor phase interface in the evaporator zone	10^{-5}
R_v	Axial heat resistance along the vapor flow	10^{-8}
$R_{ph,cond}$	Radial heat resistance of the liquid-vapor phase interface in the condenser zone	10^{-5}
$R_{c,cond}$	Radial heat resistance of the capillary structure in the condenser	10^{+1}
$R_{en,cond}$	Radial heat resistance of the condenser envelope	10^{-1}
$R_{ex,cond}$	Radial heat resistance between the outer condenser wall and external heat sink	$> 10^{+1}$
R_l	Axial heat resistance along the liquid flow in the capillary structure	10^{+4}
R_{en}	Axial heat resistance in the envelope	10^{+2}

The heat from the external heat source and the heat to the external heat sink can be transferred by conduction, convection, or radiation. The related heat resistance $R_{ex,evap}$ and $R_{ex,cond}$ is typically as high as or even higher than the overall internal heat resistance of a heat pipe, which is not discussed in detail here. For the effective resistance of the heat pipe R_{HP}, through the orders of magnitude in Table 2.2, R_l and R_{en} is negligible compared to R_v, as well as R_v, $R_{ph,evap}$, $R_{ph,cond}$ compared to $R_{en,evap}$, $R_{en,cond}$, $R_{c,evap}$, and $R_{c,cond}$. Therefore, the overall internal heat resistance of a heat pipe can be approximated by :

$$R_{HP} = R_{en,evap} + R_{c,evap} + R_{en,cond} + R_{c,cond}. \tag{2.1}$$

For DIV-HP, the radial heat resistance of the circular condenser envelope $R_{en,cond}$ follows from Fourier's law:

$$R_{en,cond} = \frac{\ln\left(d_{en,o}/d_{en,i}\right)}{2\pi \cdot l_{cond} \cdot \lambda_{en}}, \tag{2.2}$$

with the outer wall diameter $d_{en,o}$ the inner wall diameter $d_{en,i}$, the condenser length l_{cond}, and the thermal conductivity λ_{en} of the envelope material, and

$$R_{c,cond} = \frac{\ln\left(d_{c,o}/d_{c,i}\right)}{2\pi \cdot l_{cond} \cdot \lambda_{eff}}. \tag{2.3}$$

with the outer capillary diameter $d_{c,o}$ equals to $d_{en,i}$, the inner capillary diameter $d_{c,i}$, the condenser length l_{cond}, and the effective thermal conductivity λ_{eff} of the different capillary structures [Norajitra et al. 2007].

Calculating the effective heat resistance of the evaporator usually follows the same procedure as that of the condenser.

Meanwhile, another design approach is to analyze the performance limits of the heat pipe, which should be higher than the required heat flux. If not, the heat pipe will reach the performance limit and fail.

Typically, there are five performance limits:

- **Capillary limit:** is the most critical of the five performance limitations. It determines the maximum heat flux Q_max necessary to ensure that the sum of all pressure drops and differences throughout a single loop are zero in order for the 2-phase flow of the heat pipe to successfully circulate in a closed circuit.

$$0 = \Delta p_c + \Delta p_l + \Delta p_v, \tag{2.4}$$

where Δp_c is the capillary pressure difference between the liquid-vapor phase, driving the liquid from the condenser to the evaporator. And $\Delta p_l = \Delta p_{l,fric} - \Delta p_{l,stat}$ is the total pressure drop of the liquid flow, including the pressure loss due to friction $\Delta p_{l,fric}$ according to Hagen–Poiseuille equation and the hydrostatic pressure difference $p_{l,stat}$ influenced by gravity. Δp_v is the total vapor pressure drop only considering the hydrodynamic pressure drop at the friction and inertia part along the entire vapor flow.

To simplify, the maximum capillary pressure difference $\Delta p_{c,max} = 2\sigma/R_{eff,min} \cdot cos\theta$, with liquid surface tension σ, wetting angle θ and the minimum effective curvature radii of liquid-vapor menisci $R_{eff,min}$. Hence, the maximum heat flux can be estimated by

$$Q_{\max} = f\left(\Delta p_{c,\max} - (\Delta p_l + \Delta p_v) = 0\right), \tag{2.5}$$

- **Entrainment Limit:** the movement in the opposite direction of the vapor relative to the liquid flow generates shear stresses at the vapor-liquid interface that reduce the maximum amount of liquid flowing back to the evaporator and limit the amount of heat that can be transported; this limit can be estimated with the formula

$$Q_{entrainment} = \Delta h_v \cdot \sqrt{\frac{\sigma \cdot \rho_v}{2 \cdot r_{hydrulic,c}}}, \tag{2.6}$$

  where ρ_v is the vapor density,$r_{hydraulic,c}$ is the hydraulic radius of the capillary structure, and it is equal to groove width w (this has the most considerable contribution, the limit due to mesh or sintered structures being consistently superior to the one involving grooves); Δh_v is the latent heat of evaporation, and σ is the liquid surface tension.

- **Boiling limit:** at high heat fluxes, the strong enough wall superheat in the evaporator zone may activate potential nucleation boiling, resulting in the formation of vapor bubbles inside the capillary structure, which have a negative impact on the liquid-driven flow and generate localized dry-out; for open porous structures, meshes, or grooves, this limit is less relevant since the bubble can escape to the open vapor space. The critical power and temperature difference are given by

$$Q_{boiling} = \frac{\Delta T_{crit}}{A_{evap} \cdot R_{c,evap}}, \tag{2.7}$$

$$\Delta T_{crit} = \Delta T_{c,i,cond} - \Delta T_v = \frac{2 \cdot \sigma \cdot T_v}{\Delta h_v \cdot \rho_v} \cdot \left(\frac{1}{r_b} - \frac{1}{r_{eff}}\right), \tag{2.8}$$

  where, A_{evap} and $R_{c,evap}$ is the surface and heat resistance of the capillary structure in the evaporator. $r_b = \sqrt{\frac{2 \cdot \sigma \cdot T_v \cdot \lambda_l}{q_b \cdot \Delta h_v \cdot \rho_v}}$ is the radius of the vapor nucleus. r_{eff} is the effective radius of the capillary structure's curvature. The vapor temperature T_v is assumed to be the saturation

temperature. $T_{c,i,cond}$ is the inner side temperature of the capillary structure, next to the vapor nucleus. The bubbles are generated if the critical wall superheat ΔT_{crit} is exceeded.

- **Viscous limit:** this limit is primarily relevant for operating near the melting point when the vapor pressure and density are low, and the viscous effects dominate the vapor dynamic. This limit is irrelevant for our case since we operate at temperatures above 130 °C.

$$Q_{viscous} = \frac{d_v^2 \cdot \Delta h_v}{64 \cdot \eta_v \cdot l_{eff}} \cdot \rho_{v,evap} \cdot p_{v,evap}, \tag{2.9}$$

- **Sonic limit:** this limit is primarily relevant for high-temperature heat pipes using liquid metals; it is reached when the vapor velocity exiting the evaporator reaches the sonic speed; since water is used as a working fluid in this study, this limit is not relevant.

$$Q_{sonic} = 0.474 \cdot \Delta h_v \cdot \sqrt{\rho_{v,evap} \cdot p_{v,evap}}. \tag{2.10}$$

2.3 Integration of a Heat Pipe in a DEMO Divertor

The divertor heat pipe is integrated into the DEMO divertor cooling target. The defined working condition of the DEMO divertor is seen as the performance criteria of the divertor heat pipe, so that the structure and working condition of the DEMO divertor are changed as little as possible.

2.3.1 DEMO divertor target structure

The current baseline DEMO divertor [Bonavolontà et al. 2020][Mazzone et al. 2020] sits at the vacuum vessel's lower region. Along the toroidal direction, the divertor cassette body combined with the plasma-facing target is arranged symmetrically. The plasma-facing target contains the cooling system, which receives the plasma heat first. According to the fusion reactor structure, the outboard vertical target (OVT) is far from the center of the vacuum vessel and has an inclined angle between the gravity direction of 82.2°. The inboard vertical target (IVT) is close to the central core with an inclined angle between the gravity direction of 75.7°. Behind the OVT, the outboard region of the cassette body has the thinnest section, which is around 370 mm thick; and the inboard region of the cassette behind the IVT has the thinnest part, which is 470 mm thick, as shown in Figure 2.6. The evaporator is below the condenser when the heat pipe is integrated on both targets instead of the baseline water cooling. It means that when the angle between the gravity direction and the target is small, the liquid pressure loss is lower, so the heat pipe on IVT performance is better than OVT.

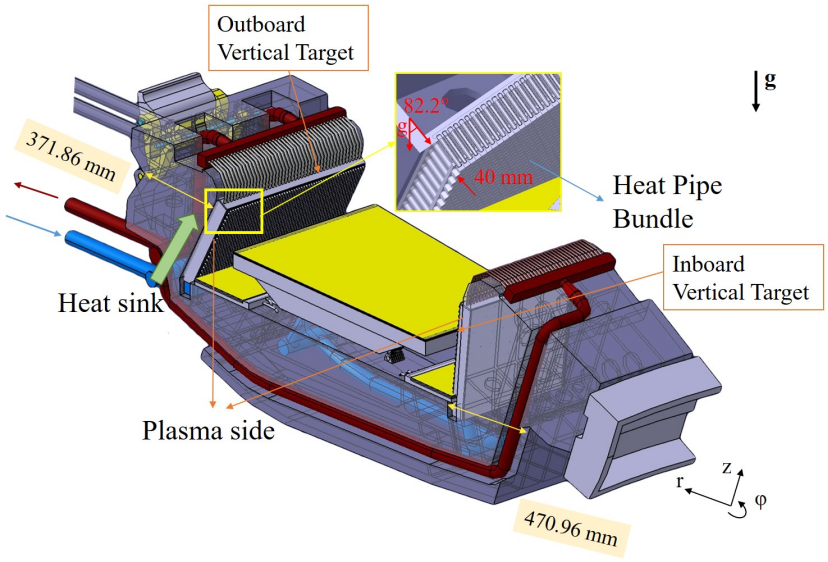

Figure 2.6: Divertor cassette assembly with a Heat Pipe-based divertor target cooling for the DEMO design [Eurofusion 2019].

In order to minimize modifying the structure of the divertor cassette body, plasma-facing target, and the coolant characteristics of the baseline water cooling circuits as little as possible, the specifications of the current coolant system, known as the baseline design, restrict the design of the heat pipe based divertor target coolant system.

The current baseline cooling system of the DEMO divertor plasma-facing target transports heat by imposing cooling liquid flow through a long pipe protected by a longitudinal array of rectangular tungsten blocks as the heat sink, as shown in Figure 2.7.

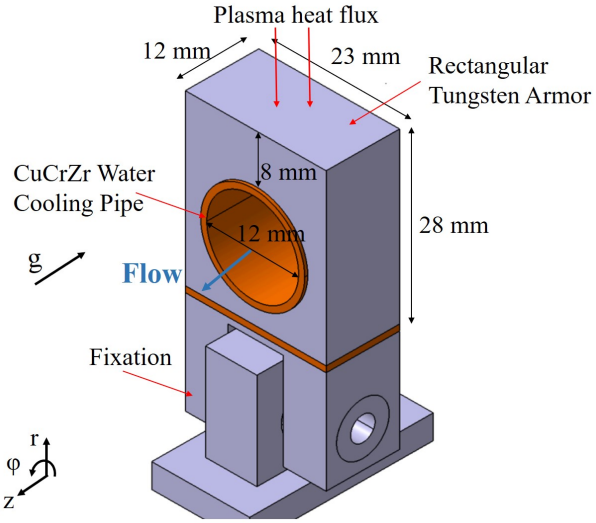

Figure 2.7: One base-line water coolant monoblock with dimensions of the original divertor cooling taget.

The tungsten blocks have an 8mm thickness from the plasma-facing side to the cooling pipe. They can protect the leading edge in handling areas of high heat flux and minimize the effects of melting during off-normal events [Hirai et al. 2016]. The section width of the armor blocks was set at 23 mm with one block thickness of 12 mm, making the width of the plasma-facing target plate segmented into several parallel rows, each row 23 mm wide. The target cooling is installed on the cassette body with fixation, so there is 40 mm between the tungsten monoblocs surface (plasma-facing side) and the cassette's body surface.

The 12 mm inner diameter water cooling pipe with a thickness of 1.5 mm (with swirl tape) is joined with a copper layer through the center of the tungsten blocks. The cooling liquid flowing through the baseline heat sink pipe is 5.3 m^3/h at 130 °C and 4MPa, corresponding to an average velocity of 13m/s. Since the present cooling flow conditions only apply to one 23 mm wide parallel longitudinal array of the baseline coolant blocks, it is necessary to convert an equivalent cooling area and efficiency when designing the DIV-HP heat sink with the same heat flux.

Under nominal operating conditions, when plasma hits the target, the maximum local heat flux concentrated on a band (strike point) is between 10 and 15 MW/m^2, which is assumed for regular operation (5000 pulses during lifetime) as a safety margin [You et al. 2022]. Meanwhile, as there are slow transients of power decay for several seconds, the local peak heat flux can reach 20 MW/m^2 (300 pulses), respectively. The low heat flux at the areas far from the hitting point of the divertor target is 1 MW/m^2 due to the plasma radiation.

To summarize, the DIV-HP on the OVT is examined first because it has more liquid pressure loss, and the cassette body behind the OVT is thinner than the IVT. Meanwhile, a heat pipe used for a divertor target should generally operate between 1 and 10 MW/m^2 and have the ability to operate safely when the load increases up to 20 MW/m^2. As such, 20 MW/m^2 is chosen as the maximum heat flux of a DIV-HP with an evaporator below the condenser and a coolant of 5.3m3/h at 130 °C and 4MPa.

2.3.2 Divertor heat pipe materials and geometry

According to the merit figure mentioned above, illustrated in Figure 2.4, with the specified divertor coolant operating temperature of about 130 °C, the typical working liquids of the heat pipes for this operating range are CH_4O, NH_3, and water H_2O. However, NH_3 stays in the gas phase, and CH_4O is an organic compound with the issue of irradiation resistance [Anderson 2005], so it is not suitable for use in the fusion reactor. Finally, water is the best option.

The operating temperature range of water is from -30 °C to 350 °C, with the optimum working temperature being around 250 °C, where the Merit number M is approximately 10^5kW/cm^2

(10^3MW/m^2). Beyond the optimum working temperature, the curve decreases precipitously. To avoid the merit number becoming so low at high operation temperature, meaning the performance of the liquid grows worse, 250 °C is intended as the maximum operating temperature in the vapor space when maximum heat flux (20 MW/m^2) is provided.

In the baseline water cooling range, the two solids most commonly utilized in divertor are Eurofer 97 (E97) and CuCrZr. E97 is the material of choice for the cassette body since it is low-activation martensitic steel. However, it has a low heat conductivity compared to tungsten and CuCrZr and the risk of corrosion with water and liquid metals as opposed to stainless steel. Conversely, CuCrZr has superior high heat conductivity [Barabash et al. 2011], making it appropriate for low operating temperatures until 300 °C (locally 500 °C) with suitable mechanical strength [Bigot 2022]. Hence, the heat pipe envelope and capillary structure use CuCrZr. And the heat pipe temperature, especially the evaporator, should be controlled well below 450 °C.

The evaporator end should be small enough to control the received power but have at least the equivalent plasma-facing area as the baseline block (23 mm x 12 mm). Meanwhile, to integrate the evaporator on the target surface, the proposed HP has a cylindrical adiabatic section and condenser, but the evaporator is on one end of the pipe.

As with the other target designs, a 5 mm thick tile of tungsten (W-cap) covers the DIV-HP evaporator. It is a castellated hexagonal design from the HEMJ finger concept with a side length of around 10 mm (18 mm width over flat) [Norajitra et al. 2007], as a hexagon shape can relax the thermal stress. If the heat pipe evaporator is wholly joined with W-cap inner side, just like the HEMJ finger, a 15 mm outer diameter WL10 tungsten-alloy end cap, the outer diameter of the heat pipe $d_{en,o}$ is 15 mm as well. Then, the evaporator includes a 4 mm long hemisphere part and a 3 mm long cylindrical part, as depicted in Figure 2.8.

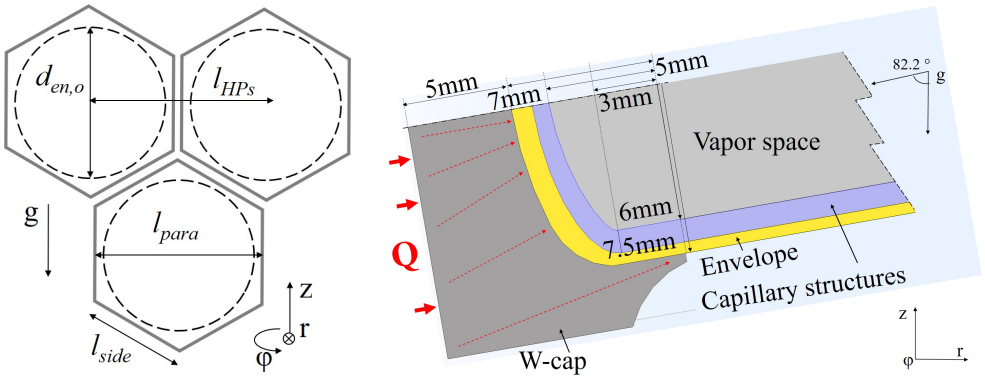

Figure 2.8: Heat pipe evaporator with HEMJ W-cap. (a)3 arranged W-caps with hexagonal surface (b) W-cap with evaporator.

The power deposited on the hexagon surface 259.8 mm^2 is close to 5.2 kW in case of a similar incident heat flux of 20 MW/m^2. It is similar to the power deposited at the baseline blocks. Numerous cylindrical heat pipes joined with W-caps can be inserted in a water-cooled target with a gap of 0.5 mm between each other, forming staggered parallel rows. It leaves space between each pipe and increases the external coolant's efficiency in the heat sink.

When the operating temperature of a heat pipe is 250°, the water vapor pressure is roughly 4 MPa at saturation. Given the CuCrZr's tensile strength and the aim to get a low effective thermal resistance, the minimum thickness of the CuCrZr envelope and capillary structure is roughly 1.5 mm, implying a diameter of the vapor space d_{vapor} of 12 mm. Because the vapor side is also the inner side of the capillary structure, the inner diameter of the capillary structure $d_{c,i}$= d_{vapor}=12 mm.

Table 2.3 summarizes the dimensions of the HEMJ W-cap and the related parameters of the heat pipe evaporator. Since there is already a significant amount of study on the optimization of HEMJ finger W caps under high heat flux loads [Norajitra et al. 2015], this study focuses only on the design of the heat pipe.

Table 2.3: Parameters of the W-cap and related heat pipe evaporator.

Parameters of the W-cap	**Value**
Side length l_{side}	10 mm
Distance between W-cap parallel sides l_{para}	17.5 mm
Distance between two heat pipes l_{HPs}	18 mm
The thinnest thickness of the cap plasma-facing side	>5 mm
W-cap surface: A_{W-cap}	259.8 mm^2
Maximum heat flux: Q	20 MW/m^2
Maximum power deposited on the cap surface: P	5.2 kW
Parameters of related heat pipe evaporator	**Value**
HP envelope outer diameter: $d_{en,o}$	15 mm
HP capillary structure inner diameter: $d_{c,i}$	12 mm
HP vapor space diameter: d_{vapor}	12 mm
HP evaporator length: l_{evap}	4 mm hemisphere +3 mm cylinder
Materials	
HP envelope material	CuCrZr
HP working fluid (assumed optimize temperature 250 ℃)	Water

2.3.3 Divertor heat pipe's heat sink design considering its condenser

As the vapor temperature is considered to be 250 °C and the evaporator temperature is assumed to be well below 450 °C, the temperature chain of divertor heat pipe can be estimated and controlled by the heat pipe's effective thermal resistance model. Since the same operating conditions for the baseline coolant system are used in the DIV-HP heat sink, the temperature of the heat sink coolant is known, the heat pipe design starts from the condenser, whose structure is influenced by the heat transfer coefficient of the particular heat sink design.

The parameters given are that when the applied heat flux is 20 MW/m^2, and the coolant temperature is 130 °C, the vapor working temperature is 250 °C. As a result, the heat transfer coefficient (HTC) of the heat sink α must be high enough to guarantee that the temperature difference between the coolant water and the heat pipe condenser $\Delta T_{coolant-HP}$ is minimal, so that the temperature gradient between the condenser and the vapor is relaxed.

The heat pipes with dimensioned hexagon W-caps form a staggered arrangement bundle of heated rods, which is cooled by a transverse flow in the divertor cooling system. According to sections G6-G7 of the VDI Heat Atlas [Gnielinski 2010], besides the diameter of the individual heat pipe, its arrangement, flow direction, and the length of the condenser in the heat sink also dictate the amount of heat that can be transferred. Depending on the relation between the heat pipe bundle orientation and the coolant flow direction, the heat pipes can be arranged according to the flow direction in two ways, as illustrated in Figure 2.9.

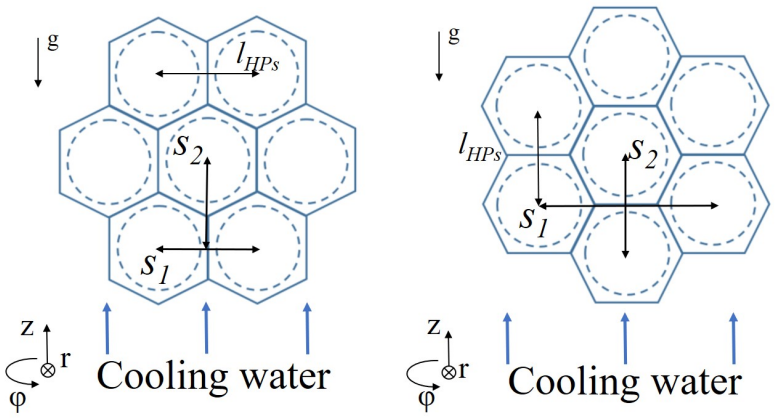

(a) (b)

Figure 2.9: Heat pipe arrangements with parameters: (a) Configuration 1, (b) Configuration 2.

The distance between the parallel sides of the W-cap is 17.5 mm, and each cap leaves a 0.5 mm gap to avoid heat expansion. Hence, the distance between the axis of two neighboring heat pipes is l_{HPs}=18 mm. In Configuration 1, as shown in Figure 2.9 (a), the parameter s_1 =l_{HPs} represents

the distances of two heat pipes perpendicular to the flow direction that are shorter than s_2: the distances of two heat pipes parallel to the flow direction. Configuration 2 shows an arrangement with parameter s_1 longer than s_2, and $s_2 = l_{HPs}$. Table 2.4 lists the parameters of two configurations based on the W-cap dimensions.

Table 2.4: Bundle parameters for the two heat sink arrangements.

Arrangement	s_1	s_2
Configuration 1	$= l_{HPs}$=18 mm	$=l_{HPs}\sqrt{3}/2 = 15.6$ mm
Configuration 2	$=l_{HPs}\sqrt{3}/2 = 31.2$ mm	$=l_{HPs}$=18 mm

Because the arrangement of the heat pipe rows is different from that of the baseline solutions, in order to maintain the same volumetric cooling flow rate for several HPs covering the same area as in the baseline, an equivalent volume flow rate distribution $\dot{V}_{coolant}$ in the toroidal direction has to be calculated. Assuming the width of the interest coolant channel is $w_{coolant}$, the $\dot{V}_{coolant}$ is:

$$\dot{V}_{coolant} = v_{base} \cdot \frac{\pi \cdot d_{base}^2}{4} \cdot \frac{w_{coolant}}{l_{base}} = v_{HP-coolant} \cdot w_{coolant} \cdot l_{cond}, \tag{2.11}$$

where $l_{base} = 23$ mm is the width of the tungsten monoblock, $v_{base} = 13$ m/s is the water velocity and $d_{base} = 12$ mm is the pipe's inner diameter in the baseline configuration, while $v_{HP-coolant}$ is the water velocity, and l_{cond} is the condenser length of the DIV-HP equals the height of the cooling channel in the heat pipe's heat sink configuration.

Then, the heat sink cooling velocity of DIV-HP corresponding to the condenser length reads:

$$v_{HP-coolant} = \frac{\dot{V}_{coolant}}{w_{coolant} \cdot l_{cond}} = \frac{v_{base} \cdot \pi \cdot d_{base}^2}{4 l_{base} \cdot l_{cond}}, \tag{2.12}$$

$v_{HP-coolant}$ influences the average Nusselt number in staggered bundles, which is also determined by operating temperature with the correction factor K and the particular parameters of the pipe arrangement:

$$Nu_{bundle,stag} = K \cdot f_{A,stag} \cdot Nu_{l,0}(\mathrm{Re}, \mathrm{Pr}, \psi), \tag{2.13}$$

where the void fraction is $\psi = 1 - \frac{\pi}{4a}$ for $b \geq 1$ and the arrangement factor is $f_{A,stag} = 1 + \frac{2}{3b}$. They depend on the transverse pitch ratio $a = s1/d_{en,o}$ and the longitudinal pitch ratio $b = s2/d_{en,o}$ in the tube bundles.

The average heat transfer coefficient (α_{ave}) is given by:

$$\alpha_{ave} = \frac{Nu_{bundle,stag} \cdot \lambda}{l}. \tag{2.14}$$

Then, the temperature difference between the coolant and condenser outer surface $\Delta T_{coolant-HP}$ can be calculated with α_{ave} as:

$$\Delta T_{coolant-HP} = \frac{Q}{A_{coolant-HP} \cdot \alpha_{ave}}. \tag{2.15}$$

$A_{coolant-HP} = \pi \cdot l_{cond} \cdot \frac{d_{en,o}}{2}$ is the heat transfer area between the coolant and heat pipe condenser.

Because the outer diameter of the heat pipe $d_{en,o}$ = 15 mm, s_1, s_2 relating to z = 18 mm in two configurations are known, following equations 2.11 to 2.15, α_{ave} and $\Delta T_{coolant-HP}$ depend only on l_{cond}.

The temperature difference between the coolant water and the outer envelope surface of the heat pipe condenser is shown in Figure 2.10 as a function of the condenser length l_{cond} for two configurations. It indicates that when the heat flux is 20 MW/m^2, the longer the condenser is, the smaller $\Delta T_{coolant-HP}$ and the temperature difference of configuration 2 is always higher than Configuration 1. It means that Configuration 1 has a higher heat transfer capability. When l_{cond}= 200 mm, $\Delta T_{coolant-HP}$ of Configuration 1 is 26 °C, while that of Configuration 2 is 42 °C. And the average heat transfer coefficient α_{ave} of Configuration 1 is 2.23x10^4 W/(m^{2}K), almost 40% higher than the α_{ave} obtained by Configuration 2 of 1.38x10^4 W/(m^{2}K). Hence, the outer temperature of the heat pipe condenser envelope $T_{en,o,cond}$ is around 156 °C with Configuration 1 when the coolant is 130 °C, away from the boiling temperature 250.6 °C of the coolant water at 4 MPa.

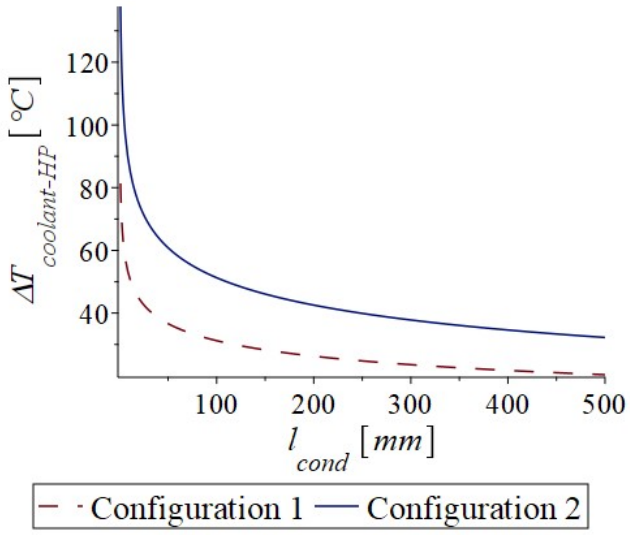

Figure 2.10: Calculated temperature difference between the HP wall and coolant as a function of condenser length for transferring 5.2 kW.

Further staggered heat sink studies focus on heat pipes arranged with Configuration 1 when the distance of two heat pipes perpendicular to the cross-flow direction corresponds to s_1=18 mm.

2.4 Options to Increase Heat Transfer Capability of a Divertor Heat Pipe

2.4.1 Condenser capillary structure based on effective thermal resistance

After knowing $T_{en,o,cond}$ through the average heat transfer coefficient of the heat sink, the corresponding temperatures at different positions assigned in Figure 2.11 can be estimated:

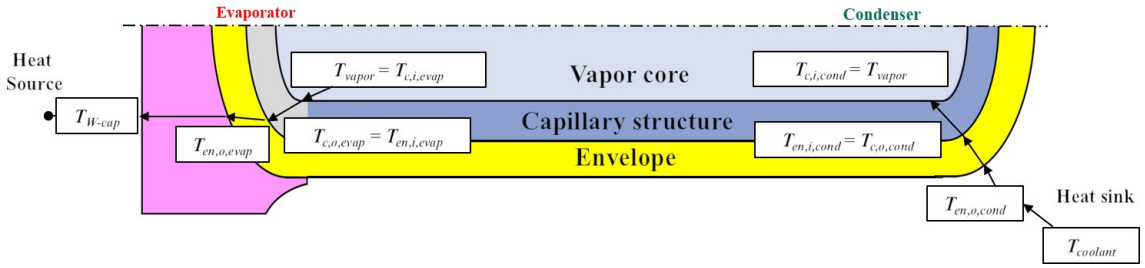

Figure 2.11: Temperature at different positions in a heat pipe.

- $T_{en,o,cond}$: the condenser temperature of the heat pipe envelope outer surface;
- $T_{en,i,cond}$: the condenser temperature at the interface between the envelope and the capillary structure;
- $T_{c,i,cond}$: the condenser temperature at the inner side of the capillary structure;
- T_{vapor}: vapor, as well as the operating temperature of the heat pipe. Ideally, it is equal to $T_{c,i,cond}$ in the saturation state if the temperature jump at the liquid-vapor interface is ignored;
- $T_{c,i,evap}$: the evaporator temperature at the inner side of the capillary structure. As the same, it is ideally equal to T_v.

All these temperatures can be predicted by the effective thermal resistance of the heat pipe, which is influenced by the dimensions of the heat pipe, and the effective heat conductivity of its capillary structure. For example, vapor temperature is:

$$T_v = T_{en,o,cond} + P \cdot R_{en,cond} + P \cdot R_{c,cond}. \tag{2.16}$$

As introduced in Section 2.1, there are three commonly used capillary structures, mesh, sintered porous structure, and open grooves. According to the decided 1.5mm thick CuCrZr in Section 2.3, the envelope thickness is $\delta_{en} = 0.5$ mm, and the capillary structure's thickness is $\delta_c = 1.0$ mm.

Condenser temperature analysis begins from these three capillary structures, with parameters listed in Table 2.5.

Table 2.5: Three commonly used capillary structures options with assumed parameters.

Design Options	**Grooves**	**Mesh**	**Sintered porous**
Number of grooves N_g	80		
Width of groove w_g [mm]	0.3		
Depth of groove ξ_g [mm]	1		
Mesh/Wire Diameter d_m [mm]		0.1	
Mesh width w_m [mm]		0.5	
Sinter particle radius r_{po} [mm]			0.05
Porosity ϵ			0.5

Figure 2.12 shows the dependence of the vapor temperatures T_v with three capillary structures in the condenser as a function of the length of the condenser l_{cond}.

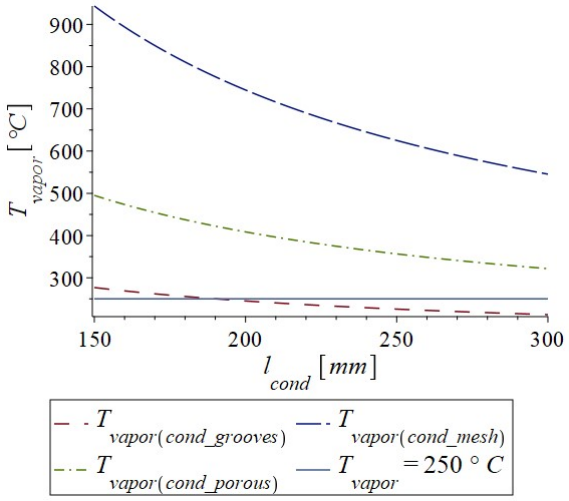

Figure 2.12: Calculated vapor (operation) temperature needed to transfer 5.2kW into the cooling circuit with different condenser capillary structures as a function of the condenser length, compared with the maximum vapor saturation temperature of 250 °C.

The horizontal line indicates the maximum vapor saturation temperature of 250 °C. It can be seen that as the length of the condenser increases, the vapor temperature decreases because of the increased heat transfer area. However, the vapor temperature of a heat pipe with a mesh and sintered porous structure is always higher than 250 °C, as they have a high effective heat resistance. Only the heat tube that uses grooves as capillary structures has a vapor temperature lower than 250 °C when the condenser length is greater than 180 mm.

Hence, based on the current external cooling conditions, the water-based DIV-HP concept chooses grooves as a capillary structure, with a minimum condenser length of 200 mm in the safety region. It is supposed to withstand heat flux of 20 MW/m^2 and maintain the HP operating temperature around 250 °C.

In addition, the insulated adiabatic part plays an important role in maintaining the stability of the heat pipe, especially when the heat pipe is exposed to high heat flux [Brahim and Jemni 2014]. Here, the adiabatic part has the same capillary groove structure as the condenser with a length of 23 mm, so the distance from the cassette to the target surface is 35 mm.

2.4.2 Evaporator capillary structure based on performance limits

The 200 mm long condenser with grooves is chosen because it is capable of transferring the 5.2 kW into the external cooling. The vapor can easily spread in the heat pipe, so the next step is to ensure that the condensed liquid water from the vapor in the condenser can return to the evaporator, feeding the evaporation process there. Hence, the capillary pressure difference has to be high enough to drive the condensed liquid back to the evaporator, forming a 2-phase circulation. Otherwise, the HP locally faces a capillary limit.

Except for the capillary limit, as mentioned in Section 2.2, there are typically five performance limits. Among them, the viscous limit for operating near the melting point and the sonic limit relevant for liquid metal heat pipe at high temperatures are ignored. In contrast, the other three limits, which include the capillary limit that determines closed circulation, the entrainment limit that takes into account the shear stress between liquid and vapor flow, and the boiling limit that activates potential nucleate boiling, are crucial in determining and dimensioning the DIV-HP capillary structures.

From the design of the condenser, it becomes clear that the shortest condenser corresponds to a heat pipe having grooves in a cylindrical pipe. However, the evaporator of the divertor heat pipe under the W-cap has a hemispherical geometry. This geometrical constraint makes it challenging to create a groove-based capillary structure in that area. Alternatively, the capillary structure of the evaporator can be made of only a mesh or sintered porous metal. In the following, two options are investigated using combined capillary structures, of which the groove is kept in the condenser with the parameters as in Table 2.5.

- **HP1 (Grooves+Mesh):** a heat pipe having grooves all over the cylindrical part of the pipe (adiabatic and condenser) and a mesh structure at the evaporator,
- **HP2 (Grooves+Sinter):** a heat pipe having grooves all over the cylindrical part of the pipe (adiabatic and condenser) and a sintered porous metal at the evaporator.

Table 2.6 lists the parameters of two evaporator capillary structures, as options for DIV-HP.

Table 2.6: Considered dimensions of two evaporator capillary structure options.

Design Options	**HP1 (Grooves + Mesh)**	**HP2 (Grooves +Sintered porous)**
Mesh/Wire Diameter d_m [mm]	0.1	
Mesh width w_m [mm]	0.5	
Sinter particle radius r_{po}[mm]		0.05
Porosity ϵ	0.74	0.5

To guarantee successful 2-phase circulation in a heat pipe, the maximum capillary pressure difference provided by the capillary structure must be greater or equivalent at least to the total pressure loss, referring to $\Delta p_{c,\max} \geq \Delta p_l + \Delta p_v$. Because the liquid recedes most in the evaporator, where the liquid has difficulty reaching, the maximum capillary pressure difference is decided by the capillary structure in the evaporator, with mesh or sintered porous metal.

Figure 2.13 (a) shows the maximum capillary pressure provided by the mesh or sintered porous metal as a function of the vapor temperature. In both cases, the capillary pressure decreases with temperature. The maximum driving capillary pressure $\Delta p_{c,max} = 2\sigma / R_{eff,min} cos\theta$ is more significant when a sintered porous metal is used in the evaporator compared to using a mesh with a wire diameter that is the same as the particle size of the sintered porous. It is because the minimum effective radius of the liquid-vapor curvature of the sintered porous metal $R_{eff,min} = 0.41 \cdot r_{po}$ <10^{-3} mm is much smaller than the mesh with $R_{eff,min} = (w_m + d_m)/2$ =0.3 mm.

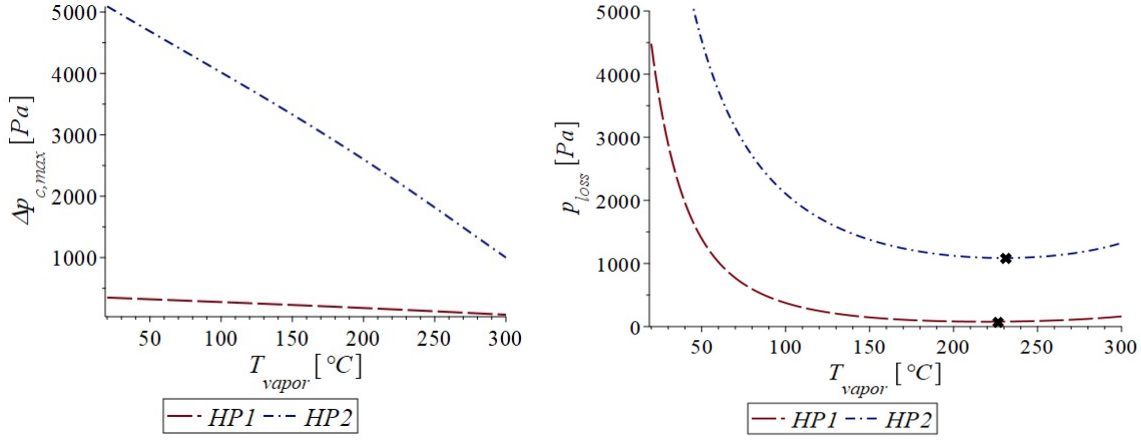

(a) (b)

Figure 2.13: Calculated variation of (a) the maximum driving capillary pressure difference and (b) the total pressure loss as a function of vapor temperature for HP with grooves and mesh (HP1) and HP with grooves and sintered structure (HP2), with assumption l_{cond}=200 mm and Q=20 MW/m^2.

Figure 2.13 (b) shows the total pressure loss due to the mesh or the sintered porous metal as a function of the vapor temperature. It indicates that the total pressure loss of the sintered porous metal is greater than that of the mesh, and it is not easy to say which structure is better. Unlike the maximum pressure difference, which gradually decreases with increasing temperature, the total pressure loss decreases rapidly and maintains a low value between 150 and 300 °C. The minimum total pressure loss of both structures is at around 220 °C. According to the merit figure, this is the ideal working temperature of the water.

Consequently, Figure 2.14 indicates the difference between the maximum driving capillary pressure difference and the total pressure loss $\Delta p_{c,max} - (\Delta p_l + \Delta p_v)$ of the two capillary structures. For operation temperatures from 50 °C to 300 °C, the difference in porous sinter metal is always positive, which means the maximum capillary pressure difference is higher than the total pressure loss and the two-phase flow can circulate successfully. Meanwhile, the difference of the sinter porous metal is always higher than mesh. Hence, sintered porous metal has more capability to transport liquid from the condenser to the evaporator, making the design less restrictive. When $\Delta p_{c,max} - (\Delta p_l + \Delta p_v) > 1000$ Pa, the curve of sintered porous metal shows that the better operation range is from 60 to 240 °C.

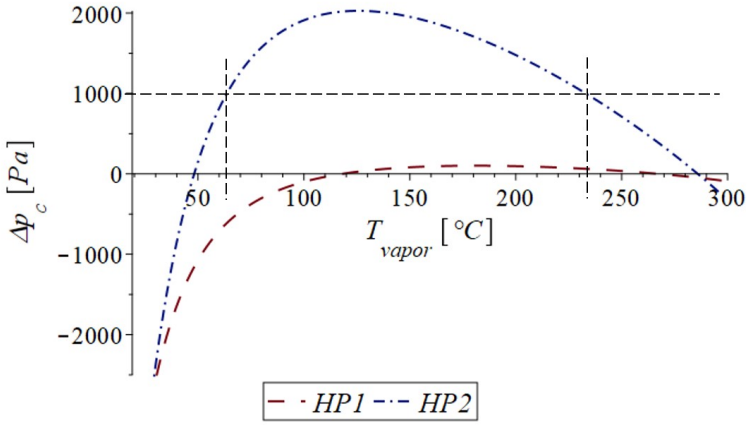

Figure 2.14: Calculated variation of the difference of the maximum driving capillary pressure difference and the total pressure loss as a function of vapor temperature for HP with grooves and mesh (HP1) and HP with grooves and sintered structure (HP2), with assumption l_{cond}=200 mm and Q=20 MW/m^2.

The performance limits and the operation temperature of DIV-HP with the combined capillary structures HP1 and HP2 as a function of the condenser length at a heat flux of 20 MW/m^2 are presented in Table 2.7. It shows that the only viable solution for the present case is HP2 with sintered porous metal in the evaporator and a groove in the 200 mm long condenser. The performance limits of HP1 with meshes at the evaporator are around half less than the proposed heat flux.

Table 2.7: Calculated operating temperature (vapor), operation limits for various condenser lengths (l_{cond}).

l_{cond} [m]	Vapor Temperature [°C]	Capillary limit HP1 [MW/m^2]	Capillary limit HP2 [MW/m^2]	Entrainment limit HP1/HP2 [MW/m^2]	Entrainment limit HP1/HP2 (mesh) [MW/m^2]	Boiling limit HP1 [MW/m^2]
0.15	276	6.1	21.4	21.9	61.5	0.82
0.2	245	8.5	28.8	21.9	61.5	1.22
0.22	233	9.6	30.4	21.5	60.0	1.40
0.25	225	10.0	31.9	20.7	58.5	1.53

Meanwhile, the values in Table 2.7 indicate that the entrainment limit is close to the maximum heat flux. The problem is solved by covering the grooves with a single-layer mesh with the same size as the one used for the HP1 option. It separates the vapor flow from the liquid flow inside the grooves, reducing the liquid-vapor shear stress, and the results of the entertainment limit is higher.

Furthermore, the boiling limit in Table 2.7 presents a rather low value, which means that the nucleate boiling is easily activated in the porous structure. According to the study by Afgan et al. [Afgan et al. 1985], enlarged surface boundaries of the meniscus in the porous core and vapor channels in the porous structure can increase critical heat fluxes. Even if the limit is low, the DIV-HP can still run with the nucleate boiling state in the porous core, which is useful for high heat flux operating conditions. The only major issue is that the liquid flow path is blocked if there are too many bubbles in the porous structure of the evaporator. Then, the condensed liquid feeding back is interrupted, resulting in a dry-out, and the heat pipe no longer works.

Finally, the water-based divertor heat pipe DIV-HP is shown in Figure 2.15.

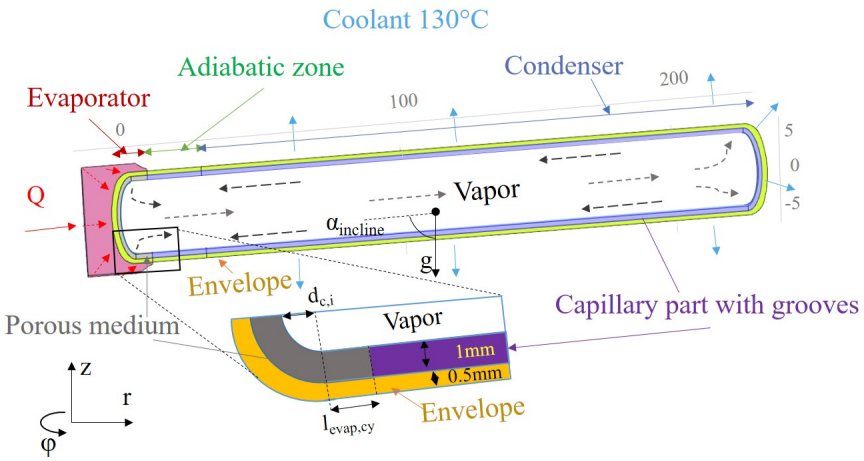

Figure 2.15: Dimensioning of the DIV-HP model combined the sinter porous and grooves as capillary structures according to analysis to meet DEMO requirements.

DIV-HP uses a combined capillary structure similar to HP2. The grooves cover a 200 mm condenser and 23 mm adiabatic section, and the sintered porous structure is chosen as the capillary structure for the evaporator with the hemispherical surface. Meanwhile, a single layer mesh of the same size as the one used for HP1 covers the grooves to increase the entrainment limit. Unlike the condenser with a standard cylindrical shape, the evaporator receives heat with its hemispherical surface and 3 mm long cylindrical part $l_{evap,cy}$.

Therefore, the heat resistance formulation has to be changed. The evaporator hemispherical surface is simplified with the same $d_{en,o}$, $d_{en,i}$, $d_{c,o}$ and $d_{c,i}$. According to the Fourier law: $P = -\lambda \cdot A \cdot \frac{dT}{dr}, Q = -\lambda \cdot \frac{dT}{dr}$ where P is the power, λ is the heat conductivity. $A = 2\pi \cdot r^2 + 2\pi \cdot l_{evap,cy}$, r is the simplified demi-sphere area with the length of the cylinder shape $l_{evap,cy}$ and radius of sphere r, then the heat resistance of the evaporator envelope is,

$$R_{en,evap} = \frac{\ln\left(\frac{d_{en,o}(d_{en,i}+2l_{evap,cy})}{(d_{en,o}+2l_{evap,cy})d_{en,i}}\right)}{2\pi \cdot \lambda_{en} \cdot l_{evap,cy}}, \tag{2.17}$$

with the thermal conductivity λ_{en} of the envelope material.

The heat resistance of the evaporator capillary structure reads to:

$$R_{c,evap} = \frac{\ln\left(\frac{d_{c,o}(d_{c,i}+2l_{evap,cy})}{(d_{c,o}+2l_{evap,cy})d_{c,i}}\right)}{2\pi \cdot \lambda_{eff} \cdot l_{evap,cy}}, \tag{2.18}$$

with the effective thermal conductivity λ_{eff} of the different capillary structures [Stephan 2010]. For outer evaporator temperature, the equation 2.19 is applied:

$$T_{en,o,evap} = P \cdot (R_{en,evap} + R_{c,evap}) . \tag{2.19}$$

According to the engineering analysis model, with CuCrZr as the envelope material and the capillary structure, the vapor temperature is around 245 °C when the applied heat flux is 20 MW/m^2, and the maximum evaporator temperature of DIV-HP with porous sinter metal $T_{en,o,evap}$ is around 350 °C, well below the limit of the evaporator temperature. Then, it is essential to test and validate the DIV-HP design experimentally, with a particular focus on the evaporator's performance, because of its low boiling limit and the possibility of operating in a nucleate boiling state.

3 Experimental Heat Pipe Focus on the Evaporator Evaluation (HPEE)

The divertor heat pipe design developed in Chapter 2 aims to work at DEMO-relevant high heat flux conditions, by considering working temperatures and capillary and entrainment limits. In order to validate the design for DEMO divertor high heat flux conditions, an experiment is initially set up to investigate certain specific issues, such as the boiling limit reached.

In this chapter, the heat pipe to evaluate its evaporator performance is designed according to the requirements to retain the design of the divertor heat pipe as much as possible. The main change is in the heat sink and heat pipe structures to make the industry manufacturing procedure easy and maintain high transfer capability. The two heat-pipe mock-ups with different evaporators are chosen. The engineering analysis model is established to predict the HPEE temperature chain. Finally, the setup and purpose of the experiment procedure are described. Data processing, especially to reduce the relative uncertainty of the calorimetric power evaluated, is also discussed.

3.1 Experimental Requirements of Heat Pipe for Evaporator Evaluation

Design approaches based on heat resistances, particularly performance limits analysis [Stephan 2010], are generally given for a cylindrical heat pipe sustained by uniform heat flux. The divertor heat pipe evaporator has a hemispherical surface of 4 mm and a cylindrical part of 3 mm, which contacts the inner surface of the tungsten armor. Hence, a high heat flux is concentrated more quickly in the hemisphere part than evenly distributed on a standard cylindrical heat pipe.

Other performance limits, such as the capillary limit, are well above the values calculated for the DIV-HP. However, even with diverse methodologies, the boiling limit depending on the small void space is challenging to define. To study the potential that nucleate boiling in the evaporator porous structure has a positive influence on HPEE heat transfer capability [Afgan et al. 1985], an experimenthas been updated, focusing on investigating the performance of the capillary structure of heat pipe evaporator. To distinguish itself from the DIV-HP, the current experimental heat pipe mock-up is referred to as the Heat Pipe for Evaluating the Evaporator (HPEE).

The HPEE first retains most of the characteristics of the DIV-HP and reproduces the same operating conditions. Thus, the following requirements are first formulated for this experiment:

- The HPEE is capable of transferring heat flux of 20 MW/m^2 as per DIV-HP requirements;
- The HPEE has an evaporator of a similar size as DIV-HP;
- The evaporator porous structure has a similar porosity and particle size as DIV-HP at first in the sense that the capillary driving force of the heat pipe is not affected. The potential optimized structure that improves the evaporator performance is seen as the second choice and be studied;
- The CuCrZr is used for the HPEE envelop, it is the same material selected for the DIV-HP;
- The operating (vapor) temperature with maximum heat flux 20 MW/m^2 is 250 °C same as the DIV-HP.

More advanced design solutions are explored on the basis of this. Some design modifications are needed to improve the evaluation accuracy, simplify manufacturing, and keep the costs for the experimental setup within reasonable margins.

The experiment was carried out under vacuum conditions with a minimum vacuum pressure of 1.5 Pa to limit thermal losses due to heat convection in the air and protect the heated surface from unwanted oxidation. Hence, the HPEE connected to a heat sink has been installed in an existing vacuum tank with a diameter of 500 mm and height of 1000 mm through the top flange with an inner diameter of 76.1 mm, like in Figure 3.1.

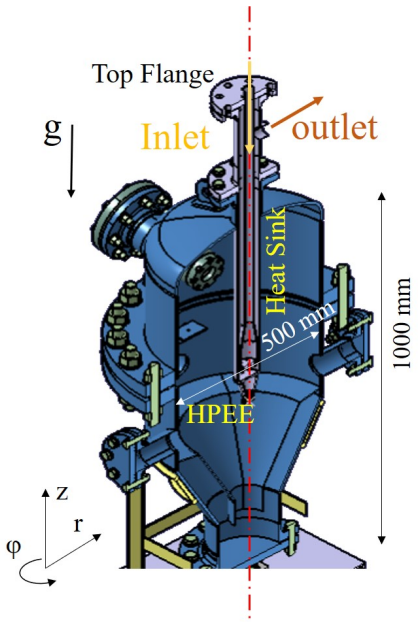

Figure 3.1: Sketch of HPEE design structures in the vacuum tank.

The inlet temperature of the HPEE heat sink is around 17 °C, maintained by an external cooling system at the KIT INR Institute. Its pressure of 0.4 MPa is regulated by the pump system.

In contrast to the hemisphere of the DIV-HP evaporator, the HPEE evaporator has been altered to be flat in order to reduce production costs and complexity. The same heated area is concentrated at the front end of the HPEE, as the DIV-HP evaporator. Because the capillary limit is not an issue in this research, the condenser is positioned directly above the evaporator at a small height, and gravity helps the liquid flow from the condenser to the evaporator with a low-pressure drop.

3.2 Design of the Experimental Heat Pipe for Evaporator Performance Evaluation

3.2.1 Heat sink and condenser design for high heat transfer capability

With the experimental setup, an estimation of the transported power is challenging by accounting for all heat losses and the surface heat load on the input power readings. As an alternative, the heat sink is used to evaluate the power and heat flux transferred by HPEE with the calorimetric method by measuring the temperature and pressure of its inlet and outlet. The calorimetric power is estimated as follows:

$$P = (h(T_{out}, p_{out}) - h(T_{in}, p_{in})) \cdot \dot{m}_{out}(T_{out}, p_{out}), \tag{3.1}$$

where h is the specific enthalpy [J/kg], and $\dot{m}_{out}(T_{out}, p_{out}) = \rho(T_{out}, p_{out}) \cdot \dot{V}_{out}$, ρ is the density [kg/m^3] of the cooling water. Both quantities are calculated based on the provisions of IAPWS Industrial Formulation 1997 for Region 1, as shown in Figure 3.2 [Kretzschmar and Wagner 2019].

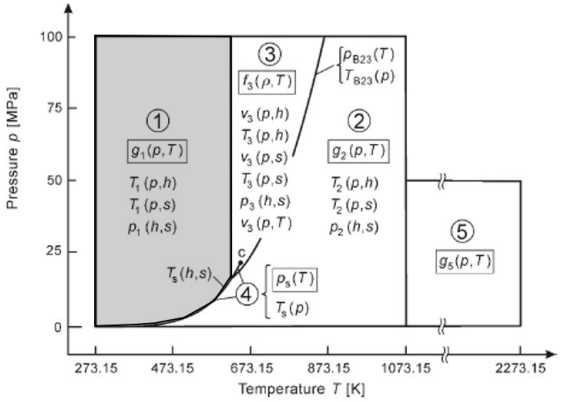

Figure 3.2: Properties region of the water and steam based on formulation IAPWS-IF97 [Kretzschmar and Wagner 2019].

To ensure the validity of the experiment results, the relative uncertainty ($U = \frac{u_{p,ave}}{P}$) of the evaluated power should be as low as possible.

The average calorimetric power is contingent on the average temperature, pressure, and flow rate in steady state, and the uncertainty of the calorimetric power is determined by the systematic uncertainty of the average measurements, with the Taylor Series Method [Coleman and Steele 2009] and GUM [JCGM106:2020 2020], as expressed in Equation 3.1.

$$u_{p,ave} = \sqrt{(h_{out}(T_{out}, p_{out}) - h_{in}(T_{in}, p_{in}))^2 \cdot u^2_{\dot{m}_{out}} + \dot{m}_{out}(T_{out}, p_{out})^2 \cdot (u^2_{h_{out}} + u^2_{h_{in}})}. \quad (3.2)$$

where uncertainty $u^2_{\dot{m}_{out}}, u^2_{h_{out}}$, and $u^2_{h_{in}}$ are related to systematic uncertainty of temperature, pressure, and flow rate $u^2_{T_{in}}, u^2_{Tout}, u^2_{p_{in}}, u^2_{p_{out}}$ and $u^2_{\dot{V}}$.

When transporting the same power, a high flow rate reduces the difference in coolant temperature between the inlet and outlet of the heat sink $\Delta T_{coolant,out-in}$. As a result, according to Equation 3.1, the difference in enthalpy as a function of temperature and pressure is small. Then, the evaluated power P is small, close to the uncertainty of the calorimetric power $u_{p,ave}$, resulting in an high relative uncertaiy of the estimated calorimetric power.

Figure 3.3 indicates that the relative uncertainty of the evaluated power U reduces as the temperature difference increases. For example, the relative uncertainty of the applied heat flux 0.5 MW/m^2 is around 68% for a coolant temperature difference of 0.5 °C but 10% for 3.1 °C. As a result, an HPEE heat sink should help maintain a continuous and sufficient coolant temperature difference between the inlet and outlet $\Delta T_{coolant,out-in}$ of at least 5 °C.

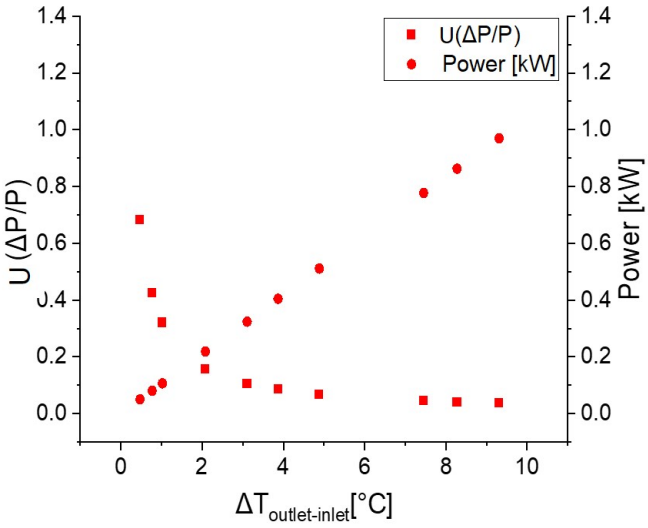

Figure 3.3: Evaluated experimental relative power uncertainty and calorimetric power as a function of the temperature difference between coolant inlet and outlet for the HPEE set-up.

Figure 3.4 gives an initial idea about the relation between the applied heat flux and the coolant flow rate for different $\Delta T_{coolant,out-ini}$ at 5 °C, 8 °C, and 10 °C. Finally, a value of $\Delta T_{coolant,out-in}$ 8 °C has been chosen so that the flow rate is controlled from 100 to 1050 l/h for heat flux of 1-20 MW/m^2.

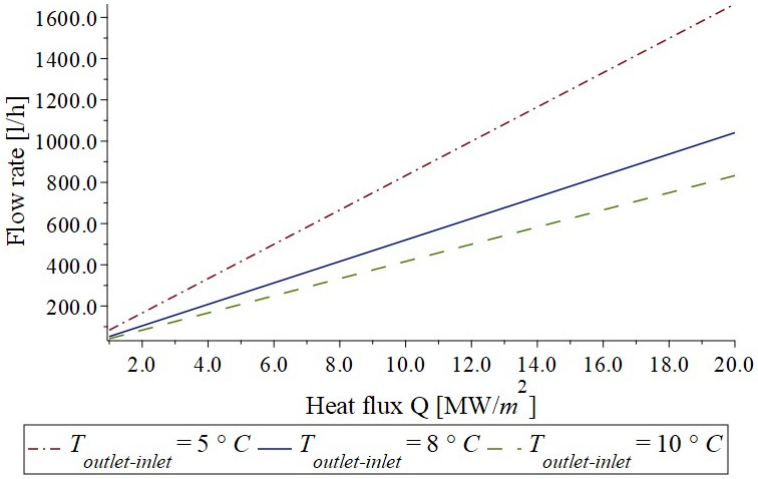

Figure 3.4: External coolant flow rate versus surface heat flux assuming a temperature rise of 5 °C, 8 °C. 10 °C.

The inlet coolant for the HPEE heat sink is controlled at around 17 °C by the external cooling system of the HELOKA experimental hall in KIT INR Institut and 4 MPa by the pump system. To keep the operating conditions inside the HPEE the same as those in the DIV-HP (mainly vapor temperature of 250 °C with heat flux 20 MW/m^2), the temperature chain along the HPEE and the effective heat resistance of various parts [Stephan 2010] are considered as in Chapter 2. Therefore, the condenser temperature is estimated first, and the condenser thickness is limited to a low value, preventing the exceeding of the vapor temperature.

The HPEE with heat sink is supposed to be installed in the vacuum tank. The size of the coolant tube is limited to DN65, having an external diameter of 76.1 mm so that it can go through the top flange of the tank. Furthermore, considering the required thickness of the pipe wall and other mechanical constraints, the cooled area, as the condenser surface, is flat for simplifying the manufacturing, limited to 3×10^3mm^2 with a flat disc of 60.3 mm in diameter. It is much smaller than the cooling area of a 200 mm long HP, around 35×10^3mm^2.

Therefore, the coolant flow rate is less than the baseline coolant system, and the coolant area is smaller. With such conditions, a cooling method not only keeps the temperature rise at the coolant inlet and outlet high enough, but it is also efficient in cooling the HPEE so that the outer surface temperature of the HPEE condenser can be similar or even lower than that of the DIV-HP.

For such reasons, an impinging jet is an excellent choice. It can provide high jet flow on the condenser surface, then flow back from an annular tube, ensuring the high-temperature difference at the coolant inlet and outlet. The vertical circulation of coolant in the impinging jet system also saved space so that it could go into the vacuum tank through the flange.

Considering different jet arrangements according to VDI heat Atlas [Wilhelm and Holger 2010] and [Martin 1977] in Appendix A, the final heat sink is implemented by an impinging jet featuring seven nozzles with a triangular arrangement, as shown in Figure 3.5, for better coverage of the condenser wall. Water flows through a 1-inch pipe, which increases its diameter to 60 mm before the condenser. The jets are generated from seven small pipes inserted in the flange. An extensive list of the parameters of the cooling system can be found in Table 3.1.

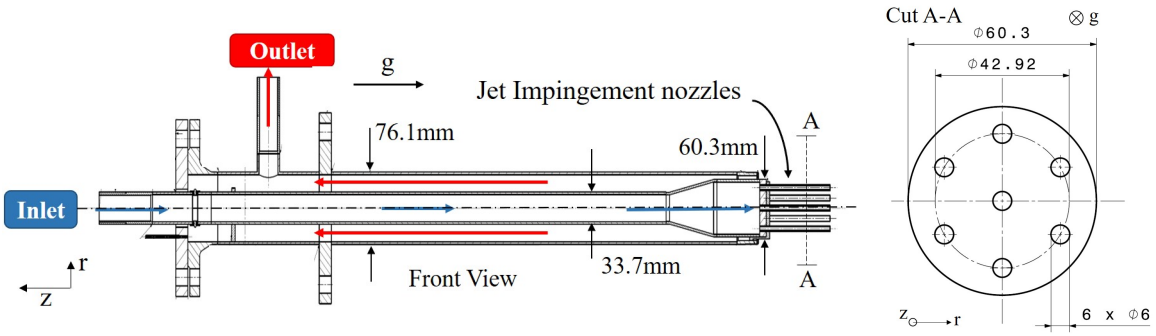

Figure 3.5: Impingement jet cooling system for HPEE (a) jet cooling system with condenser surface (b) triangular arrangement for cooling using seven jets.

Table 3.1: Parameter of heat sink system with impinging jet.

Parameters	**Symbol**	**Value**
The inlet temperature of the coolant	T_{in}	$17°C$
Pressure of the coolant	$p_{coolant}$	0.4 MPa
The outer diameter of the coolant pipe	$d_{coolant,o}$	76.1 mm
The inner diameter of the coolant pipe	$d_{cooalnt,i}$	60.3 mm
The thickness of the coolant box wall (steel)	$\delta_{coolant}$	4 mm
Number of jets	N_j	7
The inner diameter of the jet	D	3 mm
Distance between jet and bottom of HPEE	H	15 mm

The heat transfer coefficient of the different flow rates is shown in Table 3.2, which varies depending on the heat flux in order to maintain a $\Delta T_{coolant,out-ini}$ of 8 °C.

Table 3.2: The heat transfer coefficient of the different flow rates changing with the applied heat flux.

Heat flux [MW/m^2]	**Flow rate [l/h]**	**Heat transfer coefficient [W/(m^{2}K)]**
1	52.04	3731.68
5	260.19	10911.50
10	520.37	17320.93
15	780.56	22696.84
20	1040.75	27495.26

The impinging jet system connects the HPEE condenser with a screw head, as in Figure 3.6 (a). With the heat transfer coefficient, the outer surface temperature of the condenser can be estimated by the coolant temperature of 17 °C. By knowing the condenser cooled area with a diameter of 60.3 mm, the thickness of the condenser is decided by studying the effective heat resistance and the inner surface temperature of the condenser with increased heat flux. To keep the same operating condition as DIV-HP, the condenser thickness is around 10 mm, as designed in Appendix A.

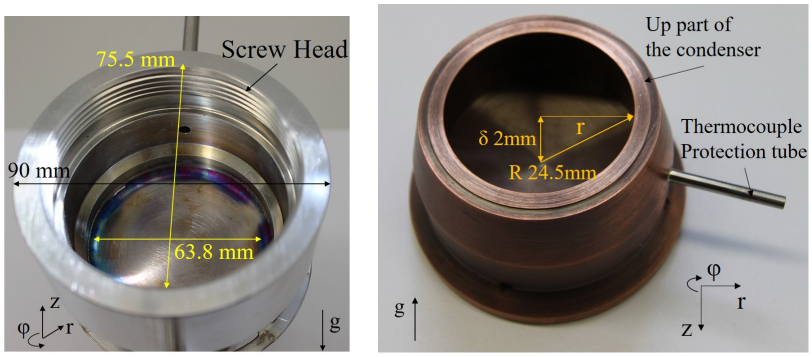

(a) (b)

Figure 3.6: The condenser (a) outer surface connecting the jet coolant heat sink with the screw head. (b) inside surface with a slope.

Because the heat pipe's condenser is positioned above the evaporator, the grooves along the complete flow direction, like DIV-HP, are not required to make production easy and economical. Hence, there are no grooves on the inside of the condenser wall. Considering that liquid droplets accumulate on the inside of the condenser surface, a slight slope is added, making the condenser wall 2 mm thicker at the margin, as in Figure 3.6(b). It helps the condensed liquid flow towards the lateral walls, preventing the droplets from directly falling into the evaporator.

3.2.2 Evaporator and adiabatic section with potential capillary structures

The evaporator of the HPEE that receives the heat directly is a flat disk for simplifying the manufacture. Taking into account the high-temperature and high-pressure operating conditions inside the HPEE at high power loads, the evaporator has to be thick enough to avoid deformation. At the same time, a too-thick evaporator increases the evaporator temperature due to an enlarged effective heat resistance. According to the stress calculations, the minimum thickness of the evaporator CuCrZr plate is 1.5 mm, the same as the DIV-HP CuCrZr thickness. As a safety precaution, the CuCrZr evaporator envelope for HPEE is specified to be 2 mm thick. As shown in Figure 3.7(a), a 2 mm tungsten plate covers the CuCrZr plate, like in the DIV-HP W-armor. It also protects the temperature sensors installed on the CuCrZr plate's outer surface.

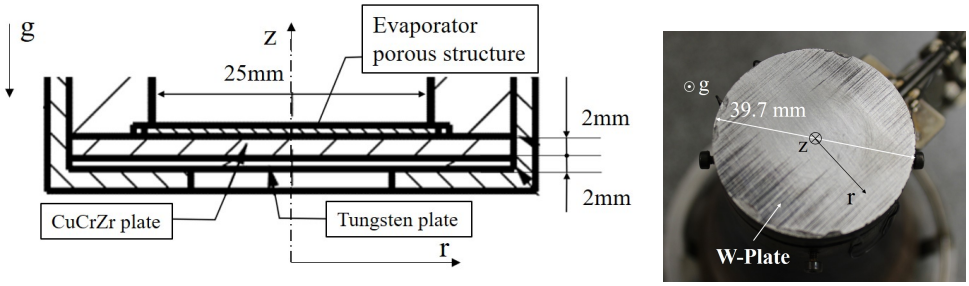

(a) (b)

Figure 3.7: HPEE evaporator (a) drawing with dimensions of HPEE evaporator-end with W-plate; (b) top view of the outer evaporator surface with W-plate (after testing).

According to initial requirements, the HPEE evaporator is considered to have a heated area close to the DIV-HP evaporator, which is the sum of the hemispherical and cylindrical area under the W-armor (400mm^2). For HPEE, the heated area of the evaporator is around 490mm^2 with a diameter of 25 mm. The diameter of the CuCrZr and tungsten plate of the evaporator, as well as the outer diameter of the cylindrical adiabatic wall above the CuCrZr plate, is 39.74 mm.

Figure 3.8 (a) shows that the adiabatic wall has a cylinder-shaped part that is 20 mm tall and 7.35 mm thick. Inside the cylindrical part, the capillary grooves are 24 mm long and 0.3 mm wide, as those of the DIV-HP. The HPEE grooves have a lesser depth of 0.5 mm, with a rounded end having a radius of 0.15 mm, different from the divertor heat pipe with a depth of 1 mm. It is to compensate for a higher channel number of 125 due to the larger circumference of the body.

The grooves intersect with the capillary structure of the evaporator which has a diameter of 26.4 mm. It allows the condensed liquid on the HPEE's adiabatic wall to flow through the capillary grooves and directly into the evaporator capillary structure as DIV-HP. The cylindrical vapor space above the evaporator has a diameter of around 25 mm and a height of 22 mm.

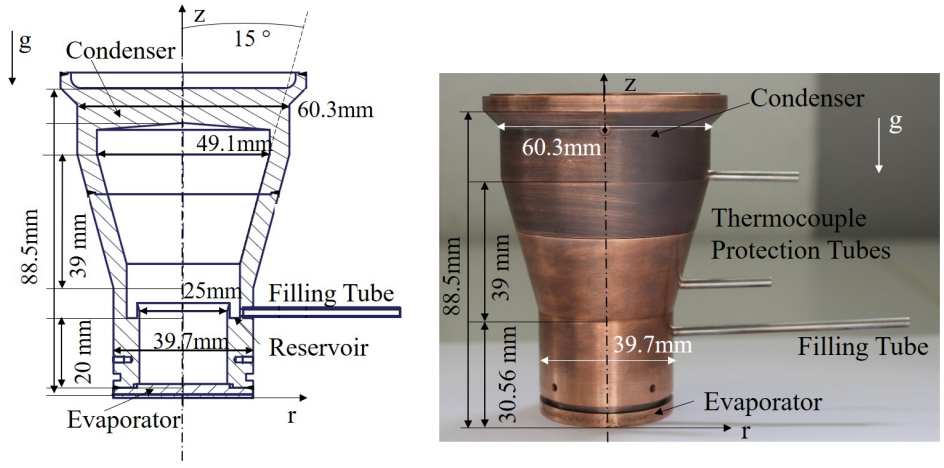

Figure 3.8: HPEE mock-up: (a) cross-section through the mock-up with dimensions, (b) photograph of the HPEE mock-up with a connecting head for the heat sink.

Above the cylindrical part, the HPEE is enlarged in a conical shape with a vertical inclination angle of 15°, as shown in Figure 3.8 (b). It is to realize the transition from the condenser with a 60 mm diameter down to a 39.7 mm diameter evaporator within a small distance of around 50 mm. The absence of grooves in the conical shape makes manufacturing simple and cost-effective, and the conical shape facilitates a gentle downward flow of liquid. The adiabatic wall thickness of this part becomes 4 mm. The parameters of the HPEE mock-up are summarized in Table 3.3.

Table 3.3: Parameters of HPEE body.

Parameters	**Symbol**	**Value**
The outer diameter of the evaporator	$d_{evap,o}$	39.7 mm
The inner diameter of the evaporator	$d_{evap,i}$	25 mm
Active Evaporator Area	A_{evap}	490 mm^2
The thickness of the evaporator envelope (CuCrZr)	$\delta_{evap,en}$	2 mm
The outer diameter of the condenser	$d_{cond,o}$	60.3 mm
The inner diameter of the condenser	$d_{cond,i}$	49.1 mm
The thickness of the condenser (CuCrZr)	δ_{cond}	10 mm
Inner length of the adiabatic zone	l_{adia}	75 mm
The thickness of adiabatic (CuCrZr)	δ_{adia}	4 mm
Vertical inclination angle	β	19.5°
The thickness of the tungsten protects plate (W)	$\delta_{w,cap}$	2 mm

Design studies for DIV-HP assume that the sintered porous material uses copper with a particle radius of 0.05 mm and porosity of 0.5. To be comparable with the DIV-HP, the sintered porous metal on the HPEE evaporator should also use Cu and the same particle size.

However, due to material and manufacturing limitations, sintered porous copper C120 suffers from adhesion problems with the CuCrZr plate. It lost its integrity even when the plate was coated with Ni and failed to integrate properly into the final mock-up. Therefore, bronze- CuSn10 (10% tin, 90% copper) as the sintered porous material B200 with a porosity of 0.47 is chosen as an alternative, showing excellent stability and precise open porosity.

The structure and properties of C120 and B200 are different:

- C120: sintered porous copper with porosity 0.42 and grain radius 118 μm, high heat conductivity of 401 W/(mK);
- B200: sintered porous bronze with porosity 0.47, grain radius 400µm and permeability 1.54×10^{-10}mm^2, heat conductivity, 50 W/(mK).

B200 has a lower pressure loss but a lower heat conductivity. Using B200, two main aspects are impacting the experimental results:

- the thickness of the B200 on the CuCrZr plate is increased to 2 mm due to its larger grain size, rather than 1 mm sintered porous copper C120 as in DIV-HP;
- the maximum heat flux that HPEE with B200 can receive is lower than C120 and could not reach 20 MW/m^2. The evaporator temperature increases rather quickly due to its low heat conductivity and thicker plate than C120, increasing the risk of approaching its operational limits or meeting the dry-out.

It is necessary to alter the porous structure to determine if it can enhance the effectiveness of the heat pipe. One possible reason why dry-out occurs in a porous structure is that the accumulation of vapor bubbles blocks liquid flow from entering a particular evaporator area. Weibel [Weibel et al. 2010] studied the influence of particle size on heat transfer capability of the porous structure, of which the maximum heat flux applied is 5.9 MW/m^2. His advanced studies [Weibel and Garimella 2012] with the radial and square grids that covers the porous structure, as well as the heat pipe spreader with multi-artery from Min [Min et al. 2009] show an improved performance of the porous structure with channels. The Cose experiment [Coso et al. 2012] with biporous fins with vertical microgrooves even reached 7.3 MW/m^2.

Making the channels on the present porous structure B200 is easier. Therefore, two HPEE mock-ups with different evaporators are designed to investigate the impact of such channels on the performance of the heat pipe evaporator. HPEE-1 with one plain evaporator uses a uniform

sintered porous structure B200 (see Figure 3.9 (a)), HPEE-2 with an enhanced evaporator and the same porous structure features a pattern of channels made through the discharge of electric wire erosion from its surface (Figure 3.9 (b)).

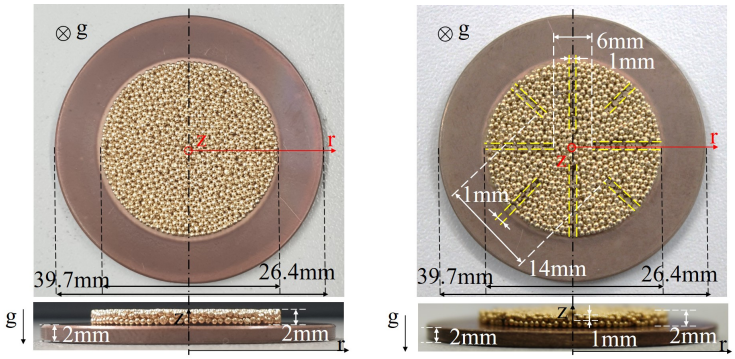

(a) (b)

Figure 3.9: Photographs of porous structure on CuCrZr plate (a) plain shape, (b) with channels.

Two sintered porous structures are affixed to a CuCrZr plate. They are identical except for the fact that HPEE-2 has channels. The parameters of the evaporator are outlined in Table 3.2.3.

Table 3.4: Parameters of wick structures: grooves, sintered porous material.

Parameters	**Symbol**	**Value**
Sinter porous for HPEE-1 and HPEE-2		
The thickness of the porous evaporator plate (Bronze)	$\delta_{evap,pp}$	2 mm
The particle size of the porous plate	r_{po}	400 μm
porosity	ϵ	0.47
Channels on sinter porous for HPEE-2		
Width of porous channels	$w_{pp,ch}$	1 mm
Depth of porous channels	$\theta_{pp,ch}$	1 mm
Number of porous channels and length	$N_{pp,ch} \times l_{pp,ch}$	4×10mm$+4\times6$mm

The design with channels locally reduces the porous structure's thickness and creates channel flow on it. Since the cross-section is comparable to the size of the porous structure grains, the liquid inside the channels is expected to be shaped as a meniscus. Such structures increase heat transfer performances by reducing the resistance for vapor to escape and friction loss of liquid flow, especially in high heat flux conditions, producing convection boiling mode with bubble and annular boiling [Stephan and Busse 1992][Deng et al. 2017].

Another issue is that when the experiment runs with various loads from 1 MW/m^2 to 20 MW/m^2, the water properties and the liquid inventory needed for evaporation are different [Guichet and Jouhara 2020] due to different operating temperatures and pressures.

It is not an issue for the DIV-HP because it is a closed system, and the maximum water is inside. However, in the experiment for HPEEs, to understand the operation of the evaporator, especially in a porous structure, the liquid condition is expected just to wet the porous structure rather than fully submerge it, resulting in a pool boiling.

If filling is performed for the maximum loading of 20 MW/m^2 directly, the excess liquid gathers on top of the sintered porous metal creats a pool of water during tests in a low power range. This results in a pool boiling-dominated operation over the evaporator characteristic of a thermosyphon rather than the intended goal - boiling inside a sintered porous structure.

Hence, a small reservoir has been created with a width of 3 mm and a depth of 3 mm (see Appendix B) at the beginning of the capillary grooves, as shown in Figure 3.10. At low-power operation, the excess liquid will gather inside this reservoir from the condenser, while at maximum power, a continuous liquid flow is ensured. The grooves help to guide the liquid from the reservoir to the evaporator smoothly on the straight part. To reduce the entrainment limit, a mesh layer covers the grooves to reduce the sheer stress and avoid liquid flow from the reservoir.

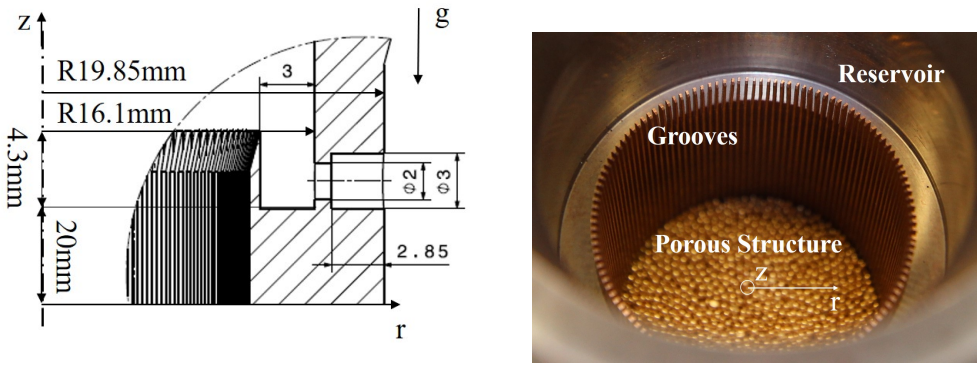

(a) (b)

Figure 3.10: Inner view of HPEE mock-up (a) drawing of the reservoir; (b) manufactured grooves and porous insert.

To investigate the evaporator performance is depending on the boiling phase change that occurs in the porous structure or a pool that boils over the porous structure, the liquid inventory inside is strictly controlled. Unlike the commonly used heat pipe and DIV-HP, which are sealed after the maximum amount of working liquid is injected, the HPEE will have its water inventory added in three stages. This will result in the heat pipe having a total water inventory that corresponds to three different experimental ranges of heat flux.

As a result, the HPEE is not permanently closed, but rather uses a well-sealed valve to control HPEE on/off. In the first round, a water inventory of 1.5 ml is filled in HPEE, which is adequate for an experiment with a heat flux of up to 1 MW/m^2. The experiment then begins after making sure the valve is completely closed. In the second round, 0.2 ml more water is added to HPEE, bringing the total water inventory to 1.7 ml for an experiment heat flux range from 1 to 5 MW/m^2. In the last cycle, the total water inventory in HPEE is increased to 2.0 ml for an experiment heat flux range of 5-20 MW/m^2. The experimental heat flux range and the corresponding water inventory are listed in Table 3.5. Details on calculating the liquid quantity needed for a certain load and the filing procedure can be found in Appendix B.

Table 3.5: heat flux range with the corresponding total water inventories in the HPEE.

heat flux range	**Liquid inventory** (V_l)
0-1 MW/m^2	1.5 ml
1-5 MW/m^2	1.7 ml
5-20 MW/m^2	2.0 ml

The mock-up was separated into two parts in manufacturing: the upper part with the condenser and the bottom part with the brazed sintered porous B200 evaporator and grooves. The grooves are manufactured through spark erosion. After the ultrasonic cleaning procedure with Isopropanol, the two HPEE parts (condenser and evaporator) equipped with nine thermocouples have been joined together by brazing. The condenser screw head and 2 mm tungsten plate at the evaporator are joined on HPEE. Then the evaporator is covered with a stainless-steel cover for protection and to fix the position of the heater, as depicted in Figure 3.11.

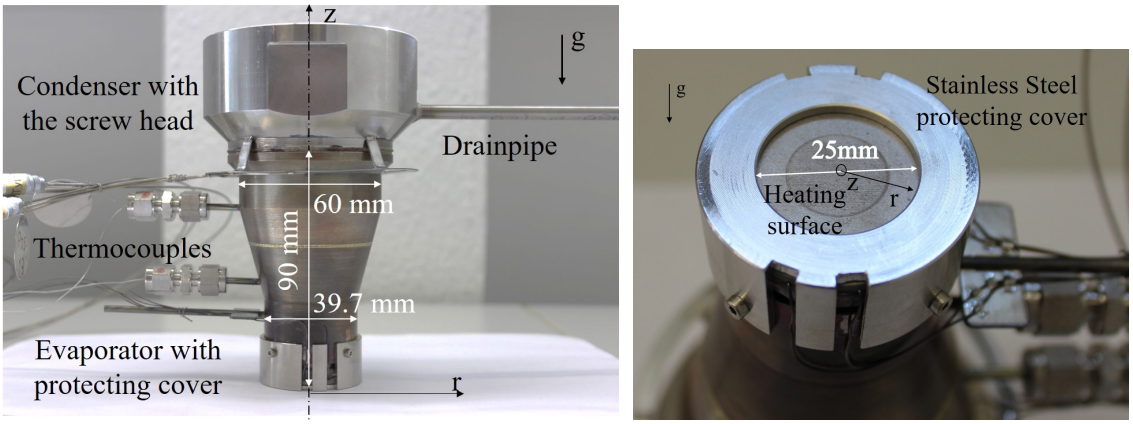

(a) (b)

Figure 3.11: Finished mock-up (a) complete mock-up body after brazing with thermocouples;(b) evaporator with protecting cover.

3.2.3 Measurement instruments for performance evaluation

The size of the mock-up, particularly the reduced vapor zone's dimensions, allows a limited number of measurements to monitor the HPEE operation. As seen in Figure 3.12, three thermocouples (HP05, HP06, and HP07) are inserted 5 mm below the outer surface of the condenser to avoid the influence of jet turbulence. Two thermocouples (HP03 and HP04) monitor the axial change in vapor temperature. Four thermocouples (HP08, HP09, HP10, and HP11), which are brazed on the surface of the 2 mm tungsten plate and contact the CuCrZr plate of the evaporator, measure the outer temperature of the evaporator. All thermocouples are K-type with nominal uncertainty ±1.5 °C or ±0.4%, their position and dimensions are listed in Table 3.6.

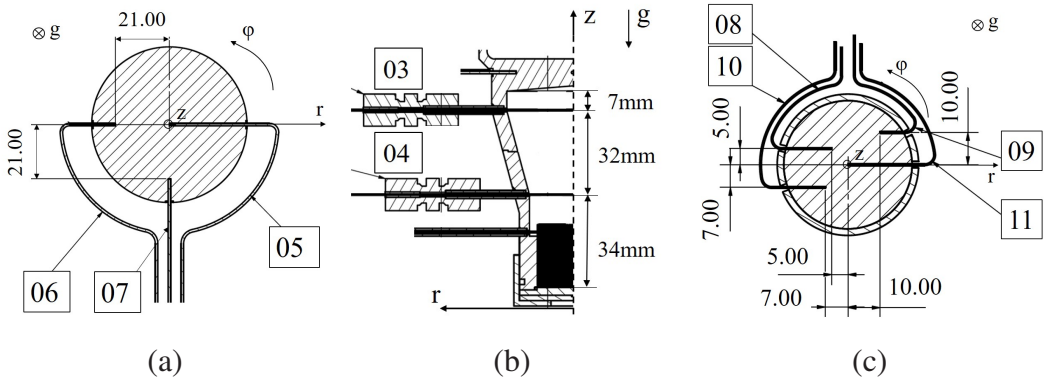

Figure 3.12: Temperature measurement arrangement of the HPEE mock-up: (a) condenser wall temperature measurements (HP05:HP07); (b) vapor temperature measurements (HP03:HP04); (c) loaded surface temperature measurements (HP08:HP11).

Table 3.6: Description of the dimension and position of the heat pipe thermocouples.

Thermocouples	Position	Diameter
HP05	Condenser center, 5 mm below the cooling surface in z dirction	1 mm
HP06	21 mm away from condenser center along r direction, 5 mm below the cooling surface in z direction	1 mm
HP07	21 mm away from condenser center along r direction, 5 mm below the cooling surface in z direction	1 mm
HP03	In vapor space, 7 mm below condenser inner surface in z axis	0.5 mm
HP04	In vapor space, 39 mm below condenser inner surface in z axis	0.5 mm
HP08	5 mm away from evaporator center in r direction	0.5 mm
HP09	10 mm away from evaporator center in r direction	0.5 mm
HP10	7 mm away from evaporator center in r direction	0.5 mm
HP11	Evaporator center	0.5 mm

3.3 Analysis Model for Temperature Chain of Experimental Heat Pipe

Following the same procedures as the one used in Chapter 2 for divertor heat pipe DIV-HP, the temperature and performance limits as prerequisites for the experiment are also essential for HPEE. Hence, an analysis heat pipe model is built using the same DIV-HP design approaches. First, the model predicts the temperature chain based on the effective heat resistance of the heat pipe by dividing it into eight parts, as shown in Figure 3.13. The calculation of the heat resistance of each part of the heat pipe is listed in Appendix C.

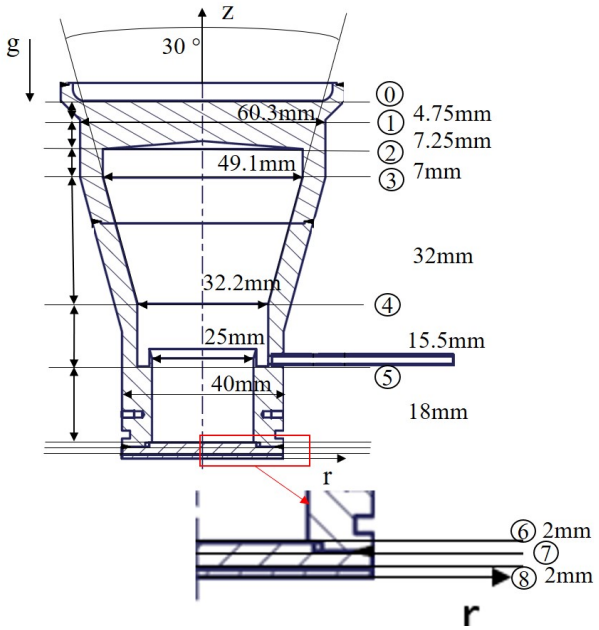

Figure 3.13: Dimensions of the HPEE in eight effective thermal resistance parts.

With this model, the temperature chains of the heat pipe can be estimated with conduction-only or with evaporation-condenser behavior. As only the inlet coolant temperature $T_{cool,in}$ is known, the evaluation of the temperature chain starts from the condenser considering the heat transfer coefficient of the heat sink when the flow rate controlling the coolant temperature rises at around 8 °C. Hence, the condenser temperature where thermocouples exist is predicted :

$$T_{cond,measure} = T_{coolant,in} + P \cdot R_{HTC_{heatsink}} + P \cdot R_{01}, \tag{3.3}$$

The temperature of the condenser's inner surface is estimated by assuming the thickness from parts 1-2 is 6 mm:

$$T_{cond,i} = T_{cond,measure} + P \cdot R_{12}, \tag{3.4}$$

The vapor temperature T_{vapor} is assumed to be the same as the temperature at the interface between the vapor and liquid film at the condenser's inner surface because T_{vapor} in the HPEE is quasi-uniform at the saturation state. Hence, the T_{vapor} is based on the estimated temperature of the condenser's inner surface $T_{cond,i}$ plus the temperature gradient due to the liquid film. Due to the liquid film thickness changes when applied heat flux and the HPEE's temperature increase. Here, the liquid film thickness is expressed simply as a constant of 0.07 mm. It is an average thickness determined by the inner side temperature of the condenser when the applied heat flux ranges from 1 to 5 MW/m^2, according to Appendix B. As the same, the heat conductivity of the water is simplified as 0.6 W/(mK).

$$T_{vapor} = T_{cond,i} + P \cdot R_{liquid-film}, \tag{3.5}$$

It is different from the approaches for designing the DIV-HP because DIV-HP has capillary structures in its condenser, which contains the liquid inside, rather than covering the condenser inner side surface.

The evaporator temperature T_{evap} is estimated in the final step by assuming vapor temperature is uniform until the vapor-porous interface. Then, the temperature gradient is calculated through the effective heat resistance of the evaporator porous (26.8 K/W when considering water in the void) at part 6-7 and CuCrZr plate (360 K/W at a constant temperature of 20 °C) at part 7-8.

$$T_{evap} = T_{vapor} + P \cdot (R_{67} + R_{78}). \tag{3.6}$$

According to the heat resistance analysis model, the evaporator temperature of HPEE-1 already reaches 600 °C with a maximum heat flux of 5 MW/m^2, because of the low heat conductivity of bronze, where the vapor temperature is 207.9 °C. This means that the experiments could not go further up to 20 MW/m^2. Table 3.7 lists the performance limits estimated using the same equation from equations 2.5 to 2.8 in Section 2.2 with a vapor temperature of 207.9 °C at 5 MW/m^2. It shows that the performance limits are high enough for the proposed heat flux of 20 MW/m^2 (9.8kW on the HPEE evaporator), and only the boiling limit needs to be considered when the critical heat flux is reached.

Table 3.7: Vapor temperature and corresponding performance limit.

Vapor temperature	**Performance limits**	**Maximum heat flux [MW/m^2]**
207.9 °C	Capillary limit	21.8
	Entrainment limit	69.8
	Boiling limit	0.087

3.4 Experimental Setup and Procedure

The HPEE with its heat source is installed in the vacuum tank, as shown in Figure 3.14 (a). It is evacuated by a vacuum pump with type PFEIFFER DUO 35 M. The minimum vacuum level that can be reached is 1.5 Pa. The impingement jet heat sink designed in Chapter 3 goes through the top flange of the vacuum tank, while the outside pump system drives the external coolant.

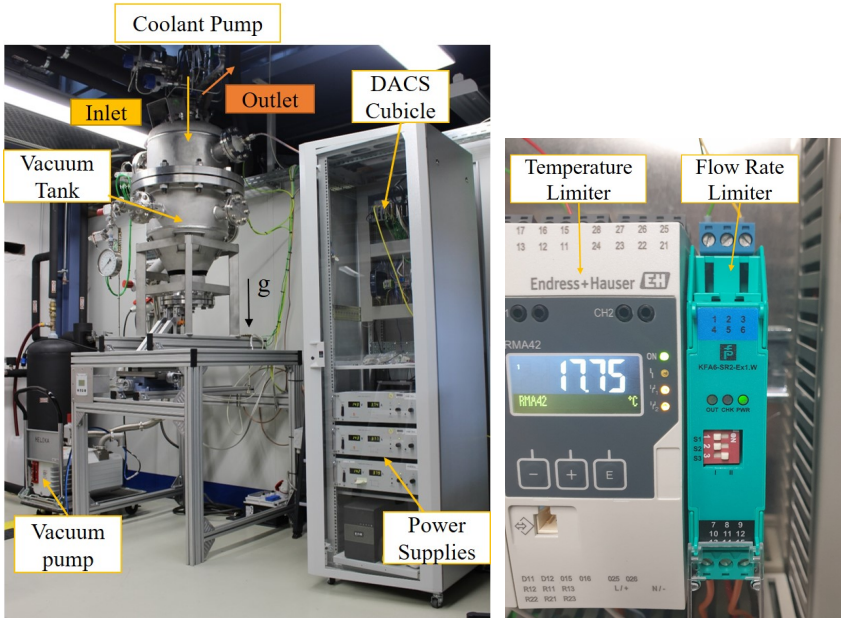

(a) (b)

Figure 3.14: Experimental setup (a) entire experiment setup with National Instrument cubicle(b) temperature limiter (gray) and flow limiter (green).

All data are recorded by the Data Acquisition System (DACS) based on National Instruments components and are monitored with LabView 2019. Origin2022 processes the collected data. The National Instruments components are installed in the Cubicle, which also contains the power supplies and Safety Interlock System. The Safety Interlock System, as shown in Figure 3.14 (b), stops the experiment immediately under specific conditions by shuting down the power supplies. The threshold values of the safety limitations are listed in Table 3.8.

Table 3.8: Three limiters and their threshold values.

Limiters	**Threshold values**
Temperature of the mock-up	>450 ℃
Temperature of the copper heater	>750 ℃
Flow meter	<50 l/m

3.4.1 Heat source and sink with function of calorimetric power evaluation

An electric copper heater has been developed as the heat source for the HPEE experiment. It uses a shaped copper block with six heaters. The block has a diameter of 80 mm and a height of 100 mm on the larger side (where the heaters are inserted), and it reduces its diameter to only 25 mm towards the heated end that comes in contact with the HPEE evaporator. Each single rod heater (from company Maxiwatt) has a diameter of 12.5 mm and is 80 mm long. They can provide a maximum power of 800W each (4800W in total) and operate up to 750 °C. Four thermocouples (HE1, HE2, HE3, HE4) monitor the temperature of the copper block in the axial direction, as illustrated in Figure 3.15(a). The power is provided by three power supplies from DELTA ELEKTRONIKA SM300-10D. Each power supply feeds two heaters and is connected in parallel.

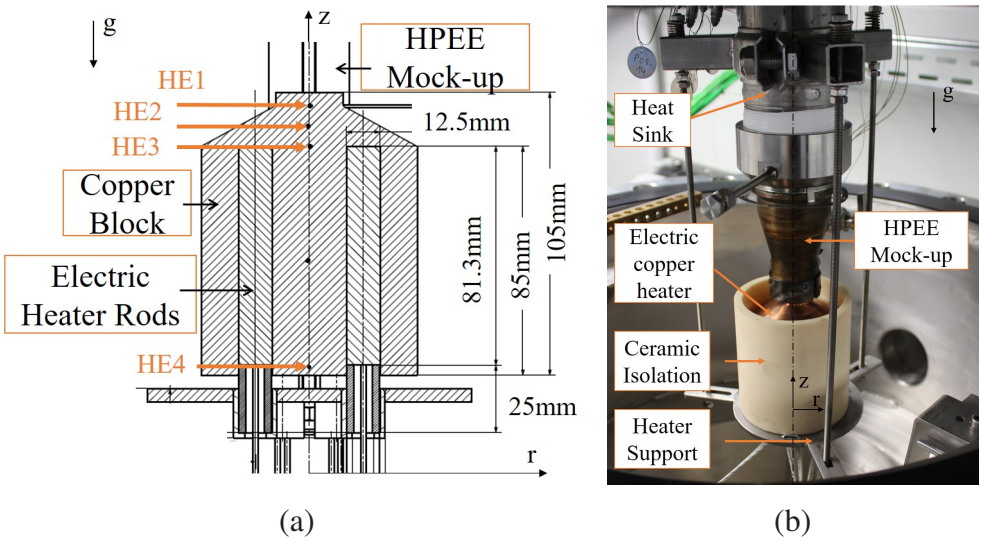

(a) (b)

Figure 3.15: Electric heating unit (a)dimension design and (b)installation with ceramic isolation in the vacuum chamber.

The heating unit is installed directly under the HPEE in the vacuum tank. Due to manufacturing issues, the evaporator protected by the tungsten plate deformed a little during brazing, so the evaporator can not contact the flat copper heater surface well. A lubricant paste with copper particles (Loctite LB 8065) covers the contact surface between the heater and the evaporator surface to increase heat transfer efficiency. In addition, the support structure is isolated with ceramic parts from the electrical heater and the copper body to reduce heat loss (Figure 3.15 (b)).

The conceptual idea of the heat sink is introduced in Section 3.2. The inlet water temperature of the heat sink fluctuates periodically between 15-18 °C due to the external cooling circuit being regulated by a chilled water machine with a hysteresis switch that keeps the coolant temperature in

the range of 15 °C to 18 °C. Due to this large temperature bandwidth, a thermal buffer is connected between the external cooling circuit and the heat sink cooling circuit. The 300 liter water in this buffer tank reduces the temperature variation of the external cooling circuit when it flows through a spiral winding, as in Figure 3.16(a). The oscillation amplitude of the heat sink inlet temperature is reduced by a factor of five, presented in Appendix D.

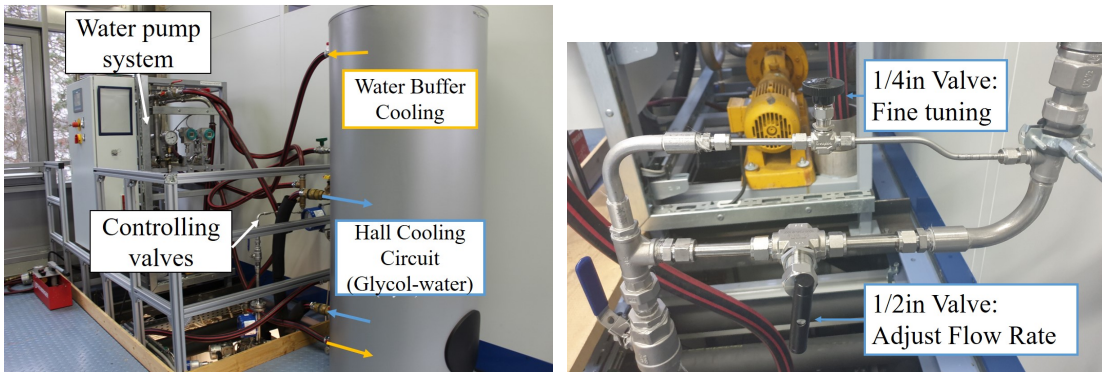

(a) (b)

Figure 3.16: Heat sink (a) water cooling loop featuring a pump system and buffer tank as a heat exchanger between the heat sink loop and the external cooling circuit (glycol-water); (b)flow regulation valve assembly installed on the return line on the outlet loop.

The pump system of the heat sink has a pressure head at a nominal flow ($5m^3/h$) of 0.1 MPa. To regulating the flow rates needed for the experiment (100l/h to 1050l/h), two control valves have been installed on the return line:

- SS-1RS4 REGULIERVALVE 1/4 SWAGEL
- SS-18RS8 REGULIERVALVE 1/2 SWAGEL

These two valves have different sizes and flow characteristics, the larger one (1/2in) being used to adjust the flow rate level close to the desired value, and the smaller one is used for fine-tuning, which is illustrated in Figure 3.16 (b).

The measurement instruments are placed close to the inlet and outlet of the heat sink to evaluate the calorimetric power transferred into the heat sink coolant by HPEE. The resistance thermometers (RTD) and pressure sensors OPTIBAR-PM-5060-C KROHNE in the vicinity of the inletoutlet of the coolant heat sink used for the calorimetric power evaluation are shown in Figure 3.17. For estimating the mass flow $\dot{m}$, the volumetric flow rate $\dot{V}$ is measured by two water flow meters (KROHNE 250 M40) installed at the outlet of the heat sink. Their testing range are 50-500l/h and 150-1500l/h for obtaining high accuracy, which are enough to be used for HPEE with the bronze porous evaporator. A complete list of the sensors with their types and accuracies is given in Table 3.9.

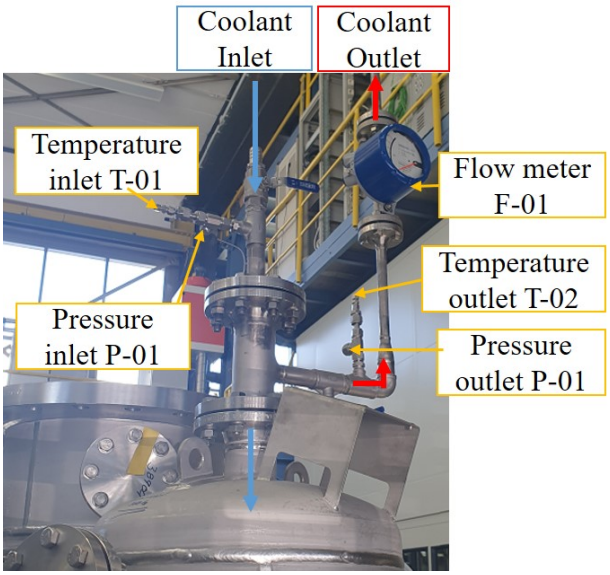

Figure 3.17: Heat sink through top flange of vacuum tank and measurement instruments (HS-T-01:02, HS-P-01:02, HS-F-01).

Table 3.9: Parameters of HPEE experiment measuring instruments for heat sink.

Component	Locationl	Model	Range	Accuracy
Temperature T-01	Inlet coolant	RTD	-200-600 °C	± (0,15 + 0,002 0 |t|) (Class A) [DIN43760]
Temperature T-02	Outlet coolant	RTD	-200-600 °C	
Pressure P-01	Inlet coolant	PM-5060-C	0-2.5 MPa	≤ ±0.5 % of span [IEC 61298-2]
Pressure P-02	Outlet coolant	PM-5060-C	0-2.5 MPa	
The volume flow rate F-01	Outlet coolant	H250 M40	50-500 l/h and 150-1500 l/h	1.6% of measured value VDI/VDE 3513-2

3.4.2 Aims of experiment and procedure

The experiment initially starts from the low power of 100W, where the heat flux is around 0.2 MW/m^2 on HPEE for safety reasons.

Meanwhile, two mock-ups, HPEE-1 and HPEE-2, are investigated with three designed liquid inventories: 1.5 ml, 1.7 ml and 2.0 ml, which are increased in three steps corresponding to three heat flux ranges: 0-1,1-5 and 5-20 MW/m^2.

As explained in Section 3.2, the heat sink coolant flow rate is adjusted according to the heat flux so that the coolant temperature rises to stay around 8 °C, reducing the degree of uncertainty in the calorimetric evaluation of the transferred power. However, although the flow meter registers a minimum flow rate of about 50l/h, the precise value is roughly 90l/h. Additionally, when the heat flux is less than 2 MW/m^2, the flow rate needed to raise the coolant temperature by 8 °C is less than 90l/h. Therefore, controlling the coolant temperature rise at 8 °C when heat flux is below 2 MW/m^2 is impossible.

As an alternative, the heat sink flow rates are controlled by three different methods, and the impact of the heat sink coolant conditions on the HPEE is examined. At first, the existing configuration keeps the flow rate 'i' constant at 90 l/h, while the heat flux ranges between 0.2 and 2 MW/m^2 or until limit conditions are reached by showing unstable behavior. Secondly, starting from a high heat flux of 2 MW/m^2, the flow rate 'ii' is regulated with the change in the heat flux to maintain a coolant temperature rise of roughly 8 °C as the initial design. When the coolant temperature rises by around 8 °C, the HPEE condenser temperature is 83 °C when the heat flux is 2 MW/m^2, and the flow rate is about 90 l/h. Finally, to maintain a constant condenser temperature at 83 °C after 2 MW/m^2, the flow rate 'iii' is regulated with the variation in heat flux.

The three heat sink flow conditions are as follows:

- (i): constant flow rate (90l/h) maintained during different heating loads,
- (ii): flow rate adjusted with the heat flux, keeping the coolant temperature rise constant at 8 °C,
- (iii): flow rate adjusted with the heat flux, keeping the condenser temperature constant at 83 °C.

The experiment procedure is as follows: first, the heat flux examined in HPEE-1 begins at 0.2 MW/m^2 with a liquid inventory of 1.5 ml and flow rate 'i'. The heat flux is then gradually increased with a typical jump of 0.2 MW/m^2 each time. After the heat source and HPEE temperatures increase a little, $\frac{dT}{dt}$ <0.5 °C/min, and reach a stable state, the experiment maintains the same heat flux and runs for an additional 60 to 90 minutes to gather sufficient data for a calorimetric power evaluation. When HPEE exhibits a sign of unstable operation or reaches operational limitations, the heat flux rise is stopped by monitoring the temperature change of the heat source and HPEE. Subsequently, the test is repeated using the same HPEE-1 and 1.5 ml liquid at a higher flow rate of 'ii,' and the applied heat flux is begun at 2 MW/m^2. When the unstable temperature behavior occurs again, the flow rate increases to 'iii,' and the test is repeated from 2 MW/m^2 as well.

After testing the three flow rate conditions on HPEE-1 with 1.5 ml, the liquid inventory is increased to 1.7 ml and 2.0 ml. Repetitive experimental steps are taken as used for HPEE-1 containing 1.5 ml liquid. Up to 20 MW/m^2. When the liquid inventory rises, there is a chance that liquid in excess of 2.0 ml could build up on the porous structure and cause the pool to boil. Therefore, in HPEE-1 a liquid inventory of 4.0 ml is examined, twice larger than 2.0 ml, to study how a greater liquid inventory, which can lead to pool boiling, affects HPEE heat transfer behavior.

3.5 Calorimetric Power Evaluation, Optimized by Relative Uncertainty Analysis

The experimental uncertainty analysis is performed according to Taylor Series Method [Coleman and Steele 2009] and GUM [JCGM106:2020 2020], where the uncertainty $u_x = \sqrt{b_x^2 + s_x^2}$ is combined by b_x and s_x. The systematic uncertainties b_x are based on the sensor accuracy listed in Table 3.9 and the measurement equipment resolution, like the NI Instruments Module. The random standard uncertainties s_x are based on the measured data's standard deviation in one test.

The uncertainty of measured data, mainly average value, is

$$u_{md} = \frac{1}{n}\sqrt{u_{md1}^2 + u_{md2}^2 + ... + u_{mdn}^2}. \tag{3.7}$$

where n is the test repeat time, at least three, with each heat flux, $u_{mdn} = \sqrt{b_{mdn}^2 + s_{mdn}^2}$.

The uncertainties propagate in temperature, pressure, and flow rate and then in calculating the calorimetric power. Figure 3.18 illustrates the temporal evolution of the temperatures recorded at the inlet and outlet of the heat sink without heat flux in 60 min.

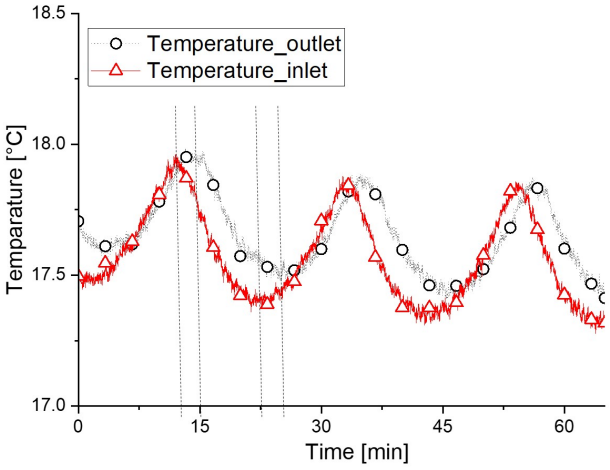

Figure 3.18: Measured temperature evolution of the inlet and outlet coolant with power 0W.

However, it shows that although the buffer tank was added to relax the temperature oscillation of the cooling machine, the temperatures, without applied power, still oscillated with an amplitude of around 0.5 °C, increasing the measured data's standard deviation of the average value. As this temperature oscillation can not be ignored and reduced, $u_{p,average}$ calculated with equation 3.2 will be high due to the high standard deviation of the temperature measurements.

To control the uncertainty of the calorimetric power at a lower level, the high uncertainty of the average $u_{T_{in}}$, $u_{T_{out}}$, has to be avoided. Hence, the uncertainty analysis as equation 3.2 is seen as Method 1, another uncertainty analysis method by determining the steady power by averaging the transient power at a steady state after directly calculating the calorimetric power using transient data at each record point is seen as Method 2, which ignores the average value of the measurements.

$$u_{p,transient,steady} = \sqrt{b_p^2 + s_p^2}. \tag{3.8}$$

The uncertainty of Method 2 $u_{p,transient,steady}$ just needs to consider the systematic uncertainties b_p, which is the same as method 1, and the random standard uncertainties s_p, showing a lower value than $u_{T_{in}}$, $u_{T_{out}}$.

Figure 3.18 also shows that the outlet temperature always delays the inlet temperature with an evident time lag dt, according to the peak of the temperature oscillation. Then, the time lag dt_{loop} and dt_{corr} estimated by two methods with different flow rates when the heat flux is 0 MW/m^2 is listed in Table 3.10.

Table 3.10: Two types of time lag with different flow rates.

Volume low rates $\dot{V}$[l/h]	**Time lag dt_{loop} [s]**	**Time lag dt_{corr} [s]**
100	102.86	120
200	51.43	60
300	34.29	36
400	25.72	30
500	20.57	18

The time lag dt_{loop} is estimated by assuming the time duration when one particle flows from the inlet to the heat sink outlet (in Appendix D). The time lags dt_{corr} is calculated with the experiment results and processed by applying MATLAB's 'finddelay' function. The 'finddelay' function makes use of the 'xcorr' function to calculate the cross-correlation between the measured data of the heat sink inlet and outlet that show possible lags. Then it calculates the normalized cross-correlation between the heat sink inlet and outlet data, whose negative value of the lag for

the biggest absolute value gives the estimated delay. As the data demonstrate a periodic case, there are multiple lags leading to the biggest absolute value of the cross-correlation, and then the smallest (in absolute value) negative value of such lags is seen as the estimated delay.

With different flow rates, the values of the two types of time lag estimation are close. It proves that this delay occurs because the coolant needs to pass through the entire loop before reaching the outlet. Due to the significant distance between the inlet and outlet of the HPEE heat sink loop, it takes time for the flow to travel from the inlet to the outlet, resulting in a time lag of the loop response and then a delay of the outlet temperature measurements. Hence, it is a systematic error and the delay can not be ignored.

However, as there is a systematic error due to the time lag dt of the heat sink loop response as in Figure 3.18, the transient power calculated using the transient measurements at the same record point is inaccurate. For example, because the outlet temperature is delayed from the inlet measurements, if the transient calorimetric power is calculated with Method 2 at time point A t_A, and the outlet measurements using data recorded at time t_A, the inlet measurement should use data recorded at time $t_A - dt$.

Therefore, to get the more accurate value of the transient calorimetric power, the evaluation should correct with time lag dt as seen as Method 3 by using the following formula:

$$P = \left(h\left(T_{out}(t), p_{out}(t)\right) - h\left(T_{in}(t-dt), p_{in}(t-dt)\right)\right) \cdot \rho\left(T_{out}(t), p_{out}(t)\right) \cdot \dot{V}(t). \tag{3.9}$$

where the time lag dt calculation has to be repeated at least once a day and before the flow rate changes to verify the accuracy. With the known time lag dt, the outlet temperature at time t $T_{out}(t)$ corresponds to the inlet temperature earlier $T_{in}(t-dt)$. At the same, $p_{out}(t)$ corresponds to $p_{in}(t-dt)$.

As a result, there are three ways to evaluate the calorimetric power:

- Method 1: calculating the average measurements of temperature, pressure, and flow rate at steady state first, then get the average calorimetric power with these average values;
- Method 2: calculating the calorimetric power with transient inlet and out measurements at the same record point, then get the average power by averaging the transient power at a steady state;
- Method 3: calculating the calorimetric power directly with transient measurements, but considering the time lag of the record point between the inlet and outlet, then get the steady power by averaging the transient power at a steady state.

An example of data processed in this way is compared with the original data without heat flux in 60 min, as shown in Figure 3.19.

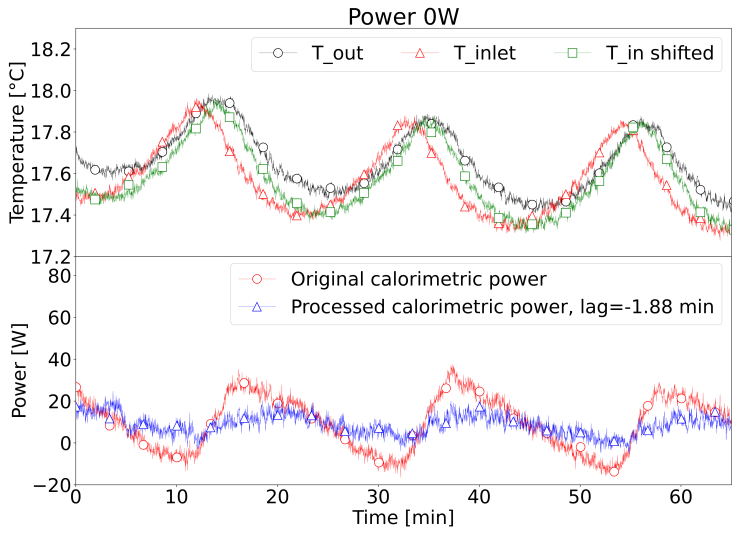

Figure 3.19: Comparison of the processed temperature and calorimetric power evolution at 0 W.

The top figure in Figure 3.19 shows the original inlet temperature (red triangle line) and the outlet coolant temperature (black circle line). By subtracting the time lag dt, the inlet temperature shifted to the same time as the outlet, shown as the green square line. The bottom figure presents the temporal evaluation of calorimetric power without taking into account the time delay (Method 2 in the red-circle-line) and after processing with the time lag dt (Method 3 in the blue-triangle-line). The calorimetric power calculated with Method 2 exhibits an obvious oscillation of around 0W during 60min with an amplitude of around 50W. While the processed power evaluated with Method 3 has a lower oscillate amplitude of around 10W without a clear peak value.

Table 3.11 lists the average calorimetric power with three methods when the flow rate is 90l/h.

Table 3.11: Calorimetric power evaluation [W] by three methods, numbers in parentheses are the computed relative uncertainty.

Power supplier [W]	**0**	**194**	**330**	**541**	**787**
Power from Method 1	8.79 (3.34)	179.69 (0.19)	307.11 (0.11)	503.23 (0.068)	738.65 (0.047)
Power from Method 2	8.23 (2.69)	178.67 (0.12)	296.63 (0.075)	489.79 (0.046)	724.22 (0.039)
Power from Method 3 (dt = 116s)	7.85 (2.36)	181.18 (0.10)	300.89 (0.062)	497.81 (0.037)	733.55 (0.031)

Except for the first column without a power (0W), the average power calculated over the same interval is almost the same through these three methods. The only difference is the relative uncertainty presented in parentheses. When Method 1 is used, the relative uncertainty is significantly higher because the average measurements have a higher standard deviation. And the relative uncertainty when using Method 3 is the lowest of the three. Hence, Method 3 is used for the calculation of the final results.

However, even though the power supplies do not provide power in some cases, the calorimetric power evaluation always shows an existing power as in the first column in Table 3.11 without power supplies, of which Method 3 presents the lowest standard deviation value. More tests without heat flux are presented in Figure 3.20 with increasing flow rates. It indicates that, even without a heat flux, a power calculated by Method 3 always exists and grows as the flow rate increases. After the polynomial regression fit, the relation between this existing power and the volumetric flow rate is $P_{exist} = (\dot{V}) = (8.85 \pm 2.83) - (0.002 \pm 0.009)\dot{V} + (7.14 \times 10^{-5} \pm 5.55 \times 10^{-6})\dot{V}^2$. It can be concluded that theP_{exist} is associated with friction losses in the coolant loop.

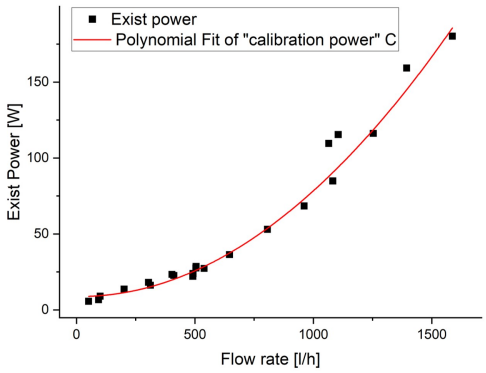

Figure 3.20: Exist calorimetric power without heat flux as a function of the coolant flow rate.

Because this power is always present due to friction loss and increases as the flow rate increases, it has to be removed from the power evaluated with Method 3 at each heat load when estimating the real power transported by the mock-up:

$$P_{trans} = P_{evaluated} - P_{exist}(\dot{V}). \tag{3.10}$$

By comparing the estimated transport calorimetric power with the one provided by power supplies, the heat transfer efficiency $e = P_{trans}/P_{Powersupply}$ is around 83-90%. It means the heat losses of the heater to the ambient is 10-17%, presenting a good heating condition.

The following experiment results, mainly the heat flux, are discussed based on the processed steady calorimetric power P_{trans}, evaluated using Method 3 by considering the time shift of the measurements and then subtracting the friction loss in the loop.

4 Heat Pipe Performance Analysis as a Function of Design & Operational Parameters

The heat transfer from the evaporator to the condenser of the working heat pipe occurs via two pathways [Weibel and Garimella 2013]: (1) conduction through the capillary and wall and (2) a two-phase heat exchange process that transports latent heat with the vapor flows. A successful working heat pipe transfers most of the heat through a circulated 2-phase flow in steady-state operation mainly because its exchange process has a higher effective conductance than the wall and the capillary structure.

At low heat inputs, heat transfer is first accomplished by conduction and evaporation from the liquid meniscus at the top of the porous structure, which is full of water. Once nucleation occurs at a critical heat flux, boiling occurs in the porous structure [Carey 2020] as in Figure 4.1's capillary-fed boiling regime. Phase change in the porous evaporator structure transports latent heat to the condenser through vapor flow, eliminating the thermal conduction resistance of the heat pipe wall and porous structure. As a result, the effective thermal resistance of HPEE is substantially reduced compared to that through the capillary structure and the wall. Then, the surface superheats drop abruptly and the evaporator temperature drops immediately as well.

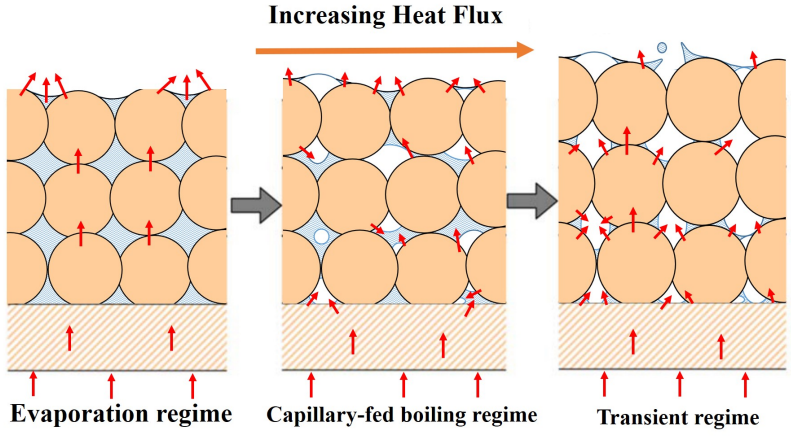

Figure 4.1: Schematic illustrations of the different two-phase flow regimes [55] for increasing heat flux at the bottom of a porous surface.

However, when the heat flux continuously increases, the liquid meniscus reduces significantly to the porous structure, as in the transient boiling regime shown in Figure 4.1. Vapor fills the cavities of the porous structure and some vapor occupies the porous structure until the bottom. Because of the surface tension, the capillary forces are still sufficient to supply the pores with liquid water for evaporation.

In this chapter, the primary method for assessing the functioning of the heat pipe is to monitor the measurements from the thermocouples on the three HPEE sections: evaporator, vapor, and condenser. After the measurement data processing, the evolution of the HPEE-1 temperature with a liquid inventory of 1.5 ml and a constant flow rate of 90 l/h is first analyzed. It is regarded as a reference for the full set of tests, and the HPEE's two-phase heat exchange behavior in accordance with the temperature evolution at the three portions of HPEE-1 is studied. Then, the possibility of improving the heat pipe performance is studied from three aspects: liquid inventories, evaporator structure, and heat sink coolant condition. Each aspect is compared by the average temperature difference between the evaporator and condenser of the HPEE, boiling curves or heat transfer characteristics of the evaporator in steady state as a function of the heat flux. Finally, the experimental results are compared with the prediction of the analysis model built in Chapter 3.

4.1 Start-up Heat Pipe Behavior of Reference Set-up

To examine whether the HPEE starts to behave like a working heat pipe, in which the heat is transferred by the working liquid's evaporation and condensation, even nucleate boiling, rather than through the conduction of the HPEE wall and the capillary structure, the start-up and transient behavior of HPEE-1 are studied. It first contains 1.5 ml of liquid within, cooled by a constant flow rate of 90 l/h, and the transient temperature evolution in the three sections of HPEE-1-the evaporator, vapor and condenser-is examined when different heat fluxes are applied.

Figure 4.2 shows the evolution of the transient temperature of the HPEE-1 with low heat fluxing of 0.2 MW/m^2 and 0.6 MW/m^2. Because of the thermal inertia of the copper heater, the power applied on the copper block of the heat source will be absorbed by itself and then transported to the HPEE by the contact surface of the evaporator. Therefore, the copper block and HPEE are heated stepwise. When power is applied to the heat source, the temperatures on the electric copper heater and all sections of the HP rise smoothly until remaining stationary. This means that the heat source and the HPEE are in thermal equilibrium and the supposed power is transported.

Figure 4.2 (a) shows that when 0.2 MW/m^2 heat flux is applied to the heat source, the temperatures of the heat source and all sections of HPEE-1 increase significantly in the first 30 min. The four temperature measurements HP08-11 in the evaporator show different values because

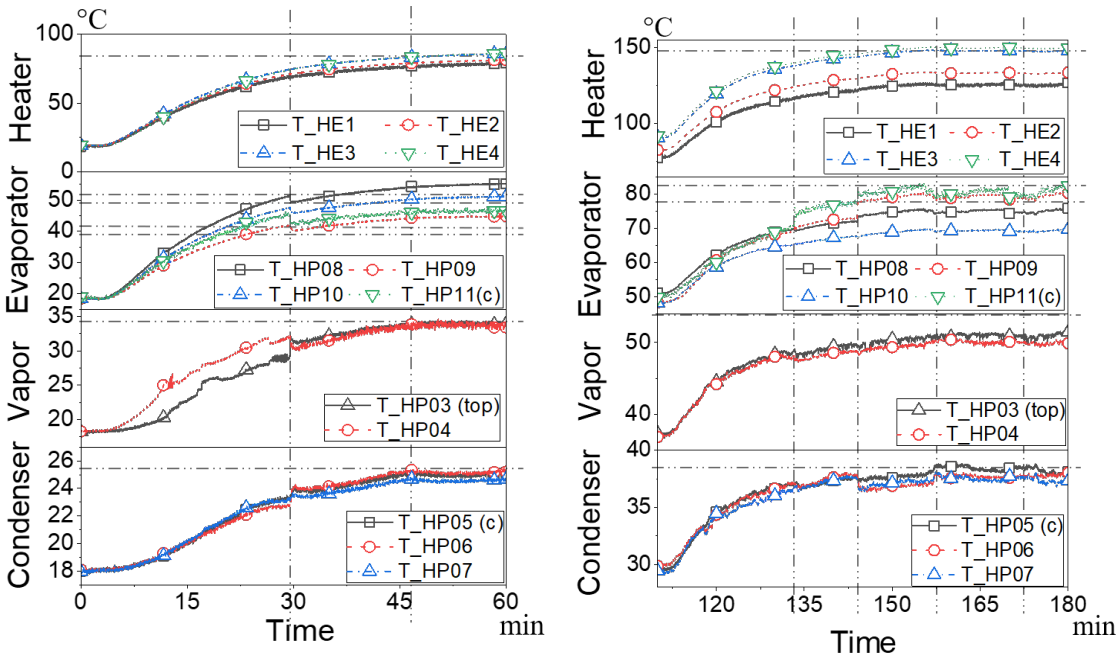

Figure 4.2: Measured temperature evolution of HPEE-1 with the liquid inventory of 1.5 ml and calorimetric power: (a)100W (heat flux:0.2 MW/m^2); (b) 300W (heat flux: 0.6 MW/m^2).

the tungsten plate that covers the evaporator is not perfectly flat during manufacturing, although copper paste is used to fill the gap. The maximum temperature shown at HP08 indicates that the position closest to the HP08 thermocouple contacts the heater surface better than others, with low heat resistance. Meanwhile, the vapor temperatures of HP03 and HP04 differ between 5 °C. The non-uniform vapor temperature inside indicates that the vapor inside is not saturated yet. The three condenser temperatures HP05-07 are practically identical during the ramp-up, controlled mainly by the heat sink. Hence, before 30 min, the HPEE's heat transfer is still evaporating from the liquid meniscus because the heat flux increases slowly and is not yet high enough to activate the nucleation.

After around 30 minutes, the temperatures are almost stable ($\frac{dT_{evap}}{dt} < 0.2$ °C/min in 30min), meaning that the heat transport in the heat source and HPEE-1 is in thermal equilibrium and is in steady state. A drop in the evaporator temperature is detected when the vapor temperature at HP03 starts to equal HP04, indicating that the nucleate boiling is activated. The vapor reaches saturation with an almost uniform temperature of around 33 °C. At that time, the saturation pressure inside is 5 kPa, according to Clausius-Clapeyron equation [Faghri 1994]. The temperature readings in the condenser increase and separate after 30 min, but showing an oscillation with the amplitude of ± 0.5 °C with a steady state period of 20 min later, same as the oscillation of the temperature of the heat sink coolant.

At 0.2 MW/m^2, the nucleate boiling is just activated after 30 min, so the bubble produced in the porous structure of the evaporator has a small volume and moves slowly or even does not move. Hence, the liquid meniscus between the vapor space and the liquid in the porous structure changes little, and the evaporation temperature is almost constant. Because more and more liquid is transferred to the vapor during boiling, and the pressure inside the HP increases. Consequently, this shifts the saturation temperature to higher values and is uniform in the entire vapor space, increasing the inner surface temperature. Thus, the condenser temperature also increases. However, since the heat flux is still low, the temperature of the heat sink inlet coolant significantly influences the temperature of the condenser surface.

As shown in Figure 4.2 (b), since HPEE-1 is heated from a lower heat flux to 0.6 MW/m^2 from 110 min, the vapor temperature at HP03 is equal to HP04 all the time without initialization, rising like copper heater and temperatures of other sections. However, during temperature rises, the temperature HP11 in the center of the evaporator increases rather quickly and soon exceeds others. The vapor and condenser temperatures oscillate when ramp up. At 135min, HP11 suddenly jumps by 5 °C, while the vapor and condenser temperatures drop slightly, the vapor temperature of HP04 is higher than that of HP03. At around 143 min, both HP11 and HP09 jump, showing substantial spreading. At 155 min, the evaporator temperature first drops and gradually increases. After 167 min, the evaporator temperatures show other drops and increases between the value 80 °C and 83 °C. The vapor temperatures are almost constant after 135 min, but the condenser temperatures always decline when the evaporator temperature jumps, showing an inverse behavior.

The difference in the temperature behavior of the evaporator in Figure 4.2 indicates a change in the operating regime of the heat pipe evaporator, especially in the center close to HP11. When the heat flux increases, vapor bubbles are continuously produced and grow larger in the porous structure of the evaporator. Some of them are joined together in the center of the evaporator, covering the center of the porous structure and blocking the liquid flow. Hence, the area of the evaporator containing liquid for phase change is reduced, the effective heat conductance is reduced, and the evaporator temperature increases. Some bubbles come out to the vapor space with high velocity, and the static pressure is reduced, lowering saturation and condenser temperature. When the condensed liquid flushes through the porous structure, pushing the vapor bubbles out, the evaporator temperature returns to a low value.

Figure 4.3 presents the evolution of the transient temperature of HPEE-1 at higher heat flux: 1.0 MW/m^2 and 2.1 MW/m^2. When the applied heat flux started with 1.0 MW/m^2, as shown in Figure 4.3 (a), the nucleate boiling is activated by observing that the temperature of HP03 equals HP04 as soon as the heat flux is delivered via the copper heating block to the evaporator, even without thermal equilibrium. At 15 min, four temperature readings in the evaporator HP08-11 rise quickly even before temperatures become stable and the vapor and condenser temperatures show

a little decrease. It is not the same as the temperature of the evaporator presented in Figure 4.2 (b) that only the measurement in HP11 oscillates between 80 °C and 83 °C at a steady state. This means that bubbles cover the porous structure of the evaporator before the HPEE reaches thermal equilibrium. At 60 min, the copper heater and HPEE-1 measurements are stable. From 90 min, the evaporator temperatures oscillate within a range of 5 °C, while the condenser temperatures oscillate within a range of 2 °C. Even the temperature of the copper heater shows a slight reduction because it is sensitive to the change in evaporator temperature.

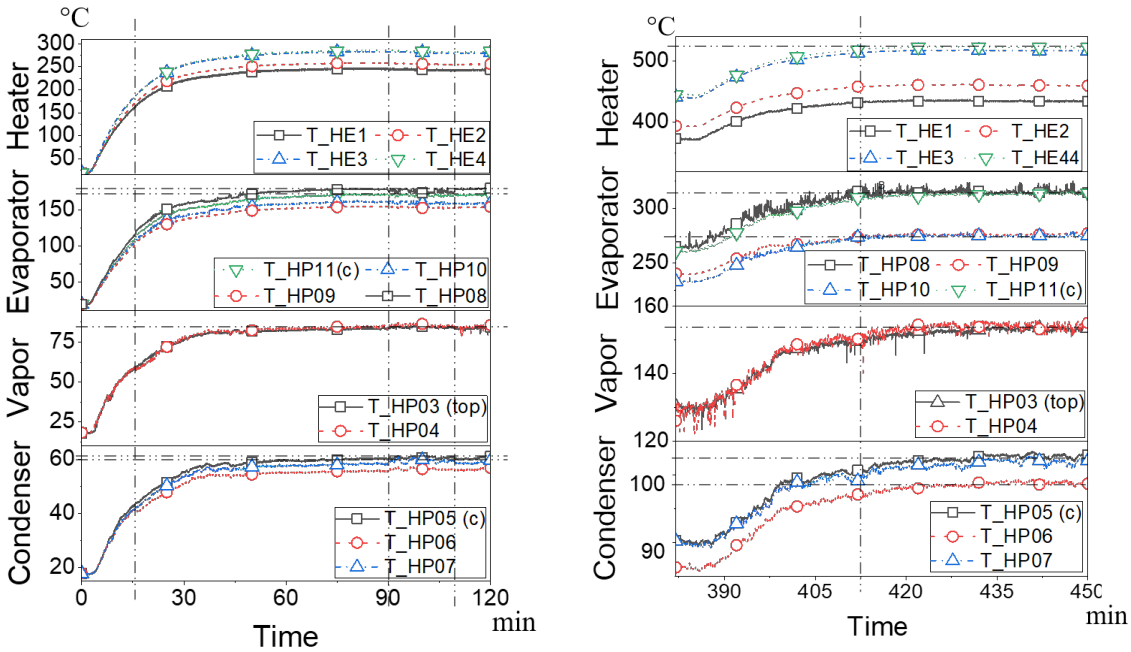

Figure 4.3: Measured temperature evolution of HPEE-1 with the liquid inventory of 1.5 ml and calorimetric power: (a)500 (heat flux:1.0 MW/m^2); (b) 1080W (heat flux: 2.1 MW/m^2).

The 1.5 ml liquid inventory is designed for the maximum heat flux of 1.0 MW/m^2. When directly applying 1.0 MW/m^2 of heat flux to the heat source, the heat flux is transferred as quickly as possible from the copper heater to the HPEE through the contact surface of the evaporator. The rate of increase in evaporator temperature is so high that the liquid in the evaporator boils immediately. However, it takes some time for the vapor produced to fill the HPEE vapor space and condenser. The capillary pressure difference between the condenser and the evaporator also needs time to stabilize and transport the condensed liquid flow back to the evaporator steadily. Therefore, the evaporator temperatures rise at 15 min.

As HPEE is continuously cooled by the external heat sink, when the pressure difference is stabilized, the condensed liquid can flow back to the evaporator, pushing the vapor bubbles out continuously. Then, the evaporator temperature becomes stable only with slight oscillation.

When the heat flux increases to 2.1 MW/m^2, the temperatures at the copper heater and HPEE-1 are stable at 420 min, as shown in Figure 4.3 (b). The evaporator temperature of HP08 is close to that of HP11 and is different from the temperature of HP09 and HP10. Meanwhile, the recorded data, especially the vapor temperature, exhibit an evident deviation, increasing the relative uncertainty of the measurement

With such a high heat flux, the liquid inventory designed for a maximum heat flux of 1 MW/m^2 is insufficient, so little condensed liquid flows back to the evaporator. As a result, the HEPP closes to the transient regime. However, the evaporation continues at the liquid-vapor interface of the liquid meniscus in the porous pore, keeping HPEE-1 behave like a heat pipe, but with increased heat resistance. The size of the vapor bubble and the rate of vapor generation increase continuously. It disturbs the stability of the vapor flow, making the pressure in the HPEE have high oscillations. Hence, the related temperature readings show a high deviation as well.

The 1.5 ml liquid inventory tested in HPEE-1 is designed for a maximum heat flux of around 1M MW/m^2, and the heat flux tested is already above this value. Repeated tests verify that the transient temperature of HPEE-1 has a smooth behavior at low heat flux and an oscillating behavior at high heat flux. The evaporator temperature increases rather quickly at 1-1.45 MW/m^2, showing a rise-and-fall behavior in a constant imposed heat flux. This oscillating behavior is kept in a specific range and disappears at a higher heat flux of around 1.6 MW/m^2. After that, the behavior of the heat pipe depends on the evaporation in the receded liquid meniscus in the porous structure. Although the thermal resistance is higher, it is still not close to the totally dry-out state, even not in the film boiling regime [Weibel and Garimella 2013]

As the temperature of the evaporator in a transient state shows an oscillation behavior at high heat flux, the average measurements of HPEE-1 with liquid 1.5 ml, while the flow rate is kept constant at 90 l/h are presented in Figure 4.4. Figure 4.4 (a) shows the average evaporator temperature T_{evap} of four temperatures at HP08, HP09, HP10 and HP11 in steady state as a function of the heat flux Q. At 0.2 MW/m^2, the average evaporator temperature is around 50 °C. When the heat flux increases to 0.4 MW/m^2, a small jump from 50° to 80 °C is observed. It indicates a boiling behavior change and more vapor bubbles are produced. Although the evaporator temperatures oscillate with an amplitude of 5 °C at a steady state during 1-1.45 MW/m^2, the average evaporator temperature T_{evap} increases linearly with increasing heat flux. Up to 1.6 MW/m^2 to 2.5 MW/m^2, T_{evap} increases rather quickly from 300 °C to 370 °C, far shifting from the linear increase trend, as the heat resistance increased with the receded liquid meniscus. The experiments are stopped at 2.5 MW/m^2 as the electric copper heater is close to its limit working temperature of 750 °C, even though dryout has not been detected.

The average vapor temperature T_{HP03} and T_{HP04} at steady state as a function of the heat flux Q in Figure 4.4 (b) shows that T_{HP04} equals T_{HP03} in the entire experimental range, proving

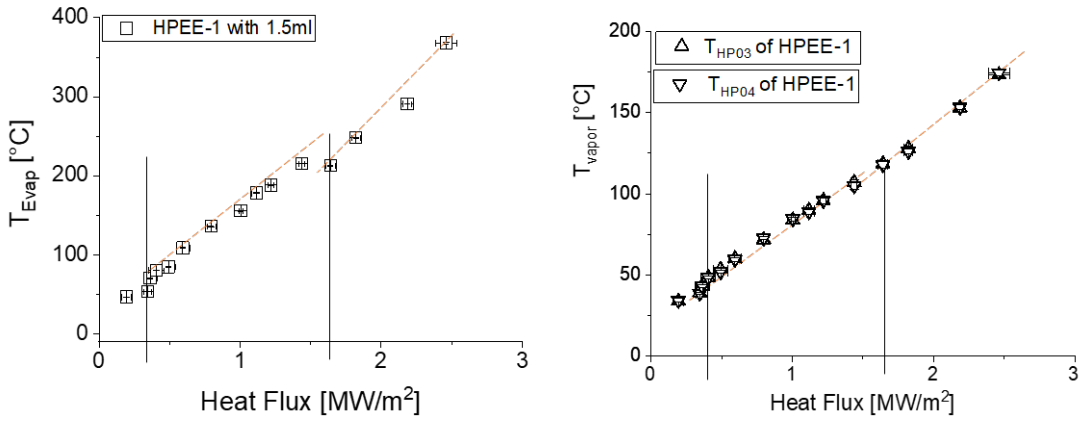

(a) (b)

Figure 4.4: Average temperature of HPEE-1 with liquid inventory 1.5 ml as a function of the heat flux with 'flow 90 l/h' (a) evaporator temperature $T_{evap,ave}$ (b) vapor temperature $T_{vapor,ave}$.

that the temperature in the center of HPEE is nearly uniform when water is saturated. They increase linearly with heat flux, showing no specific behavior at 0.4 MW/m^2 and slope change at 1.6 MW/m^2, where the evaporator temperature increases. This means that as heat flux increases, the vapor temperature, which is mainly influenced by saturation pressure, increases much more linearly than that of the evaporator. In turn, the increasing of the heat flux has more effect on the evaporator because boiling behavior in the porous structure of the evaporator (like superheat).

Although the 1.5 ml liquid inventory is designed for a maximum heat flux of 1 MW/m^2, Figure 4.4 shows that HPEE-1 with 1.5 ml can work up to 2.5 MW/m^2 without dry out. Hence, the experiment until 2.5 MW/m^2 is considered feasible, showing a better behavior than expected.

4.2 Heat Pipe Performance as a Function of Liquid Inventories

The evaporator boiling behavior influenced by the specific heat flux is understood by studying the transient temperature measurements evolution of the HPEE-1, featuring a plain evaporator porous structures, with 1.5 ml liquid inside. Then, the performance of HPEE-1 with different liquid inventories is analyzed by studying the steady-state average data in three aspects. First, the average temperature difference between the evaporator and condenser in steady state with increasing heat flux is compared with the analysis model in which HPEE-1 only transports heat through the wall conductivity, as discussed in Chapter 3. Then, to understand the performance of the HPEE-1 evaporator, where nucleate boiling occurs, the behavior of the boiling curve and the characteristic of heat transfer focused on the evaporator during a steady state with increasing heat flux are analyzed as well. Except for the liquid inventories introduced in Chapter 3 (1.5 ml,

1.7 ml, 2.0 ml), the extra test for HPEE-1 containing 4 ml of water is applied with finer resolution heat flux data points starting from the lower heat flux of 0.02 MW/m^2.

The temperature difference between the evaporator and condenser $\Delta T_{evap-cond}$ from the average value of the measured data is compared with the estimated value only through the conduction of the HPEE envelope and capillary structure, which is estimated based on the heat resistance analytic model in Appendix C according to the Fourier law.

Figure 4.5 indicates that from 0.2 MW/m^2, the temperature difference between the evaporator and condenser $\Delta T_{evap-cond}$ remains much lower than the difference estimated by the conduction-only model. This means that HPEE-1 heat transportation is dominated by a greater heat transfer capability of the heat pipe two-phase change effect. From 0.2 MW/m^2 to 0.4 MW/m^2, the temperature difference of HPEE-1 with four liquid inventories is almost the same. Above 0.4 MW/m^2, the $\Delta T_{evap-cond}$ as a function of the heat flux is linear with smaller slopes as the liquid inventory increases, meaning that the heat transfer capacities are enlarged.

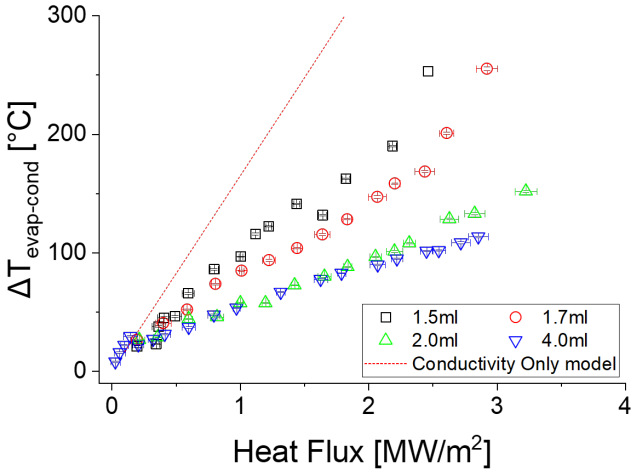

Figure 4.5: Measured temperature difference of HPEE-1 between evaporator and condenser as a function of applied heat flux with different liquid inventories under flow rate '90 l/h', comparing with the 'conductivity only model'.

With 1.5 ml liquid inside, the temperature difference between the evaporator and condenser $\Delta T_{evap-cond}$ of HPEE-1 jumped at 0.4 MW/m^2 and 2.5 MW/m^2, with temperature difference from 46-65 °C and 191-252 °C in Figure 4.5. Differently from the case with filled water of 1.5 ml, when liquid inventory in the HPEE-1 increases to 1.7 ml, estimated for a maximum heat flux of 5 MW/m^2, $\Delta T_{evap-cond}$ of HPEE-1 does not jump at 0.4 MW/m^2. It increases linearly when applied heat flux rise. The $\Delta T_{evap-cond}$ when with 1.7 ml liquid is 38 °C and 128 °C at 0.4 MW/m^2 and 1.8 MW/m^2, much lower than value for the case of 1.5 ml (45 °C and 163 °C). Up to 2.6 MW/m^2, $\Delta T_{evap-cond}$ of HPEE-1 shows a jump. The test is continued at 3 MW/m^2, where $\Delta T_{evap-cond}$ reaches 253 °C, of which the evaporator temperature reaches 380 °C.

Then, the $\Delta T_{evap-cond}$ of the HPEE-1 with liquid inventories of 2.0 increases linearly as a function of heat flux, even without showing a jump. At low heat flux from 0.02 MW/m^2 to 0.2 MW/m^2, the $\Delta T_{evap-cond}$ of HPEE-1 with 4.0 ml liquid is close to the value of the conduction only model. Then, at 0.2 MW/m^2, the $\Delta T_{evap-cond}$ of 4 ml reduce at first, and then it increase linearly with the almost same slope as the one with liquid of 2 ml up to 2 MW/m^2. After 2.2 MW/m^2, two curves separate, the $\Delta T_{evap-cond}$ of 4 ml is lower than the one with a liquid of 2 ml. The final $\Delta T_{evap-cond}$ with 2.0 ml liquid is 151.8 °C at 3.2 MW/m^2, while $\Delta T_{evap-cond}$ with 4.0 ml liquid is around 100 °C at 2.8 MW/m^2.

Experiments with 4.0 ml are stopped at a lower heat flux than 2.0 ml due to the loss of the high-conductivity paste between the mock-up and heater surface during repeated test. Then, the electric copper heater reached the working temperature limitation rather quickly, but the mock-up still shows the potential to accept more heat flux higher than the end of the experiments, as the curve still increases linearly without a sudden rise.

The temperature difference between the evaporator and condenser of HPEE-1 has a significant rise when containing 1.5 ml liquid at 0.4 MW/m^2 and 2.5 MW/m^2 and 1.7 ml at 3.2 MW/m^2, while other liquid inventories don't show the same behavior. It could be related to the increase in the temperature of the evaporator, as shown in Figure 4.4 (a), indicating that there is a change in the boiling regime, resulting in a reduction in the effective thermal conductivity of HPEE. And the $\Delta T_{evap-cond}$ of 4 ml close to the value of the conduction only model from 0.02M/m2 to 0.2 MW/m^2 indicates that the heat transfer seems to be dominated by conduction in that range.

The boiling curves related to the heat flux and the wall superheat are studied to characterize the heat transfer performance of the tested evaporator surfaces where boiling occurs [Carey 2020].

The superheat ΔT_{super} is the temperature difference between the top of the porous surface of the evaporator structure close to the vapor and the temperature of the vapor. However, it is difficult to determine the exact superheat ΔT_{super} because the temperature at the porous surface can not be measured. Hence, the sub-superheat $\Delta T_{wall-HP04}$ is employed, where T_{wall} represents the temperature at the interface of the CuCrZr plate evaporator and the porous structure. It equals the mean values of the four thermocouples in the evaporator minus the temperature gradient with a uniform heat flux distribution through the CuCrZr plate $\Delta T_{wall-HP04} = \text{mean}(T_{HP08:HP11}) - P \cdot R_{CuCrZr}$. And T_{HP04} is the vapor temperature measured by HP04, 20 mm away from the porous structure. Because the axial temperature variation is so low, this measurement is considered to provide a suitable value for characterizing the vapor temperature.

Figure 4.6 shows that when the heat flux is 0.2 MW/m^2, the $\Delta T_{wall-HP04}$ of HPEE-1 with 1.5 ml is 10 °C. When heat flux is increased to 0.4 MW/m^2, the curve is shifted to the right, where $\Delta T_{wall-HP04}$ changes from 12 to 25 °C directly, which is identified as the change in boiling

regime. Then it increases linearly with heat flux up to 2.2 MW/m^2, where the $\Delta T_{wall-HP04}$ is around 130 °C. After 2.2 MW/m^2, the curve slope becomes mild, as $\Delta T_{wall-HP04}$ increases rather quickly, but heat flux changed little, indicating a trend of the boiling regime shifting again.

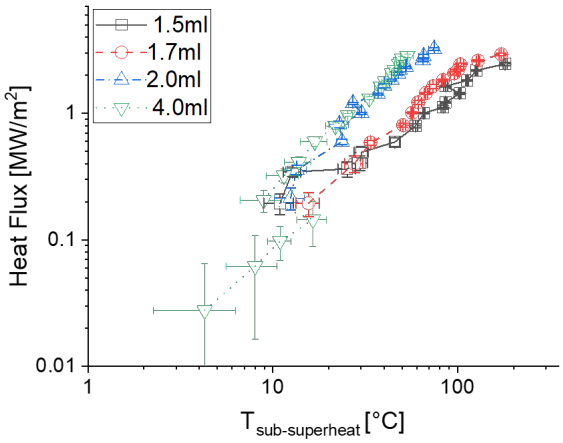

Figure 4.6: Measured boiling curves that heat flux as a function of the sub-superheat $\Delta T_{wall-HP04}$ of HPPE-1 for different liquid inventories at a heat sink flow rate of 'flow 90 l/h'.

For a liquid inventory of 1.7 ml, the sub-superheat $\Delta T_{wall-HP04}$ of HPEE-1 increases linearly from 0.2 MW/m^2 up to 2.4 MW/m^2, then the slope becomes gentle, showing a trend of the change in the boiling regime. The HPEE-1 curve with 2 ml moves to the left, which means that when transporting the same heat flux, $\Delta T_{wall-HP04}$ is smaller than one of 1.5 and 1.7 ml. The curve increases linearly, showing no clear indication of slope change up to 3 MW/m^2, which means no boiling regime change.

The sub-superheat $\Delta T_{wall-HP04}$ of 4 ml with fine resolution heat flux data points from 0.02 MW/m^2 to 0.2 MW/m^2 is higher than others but with high uncertainty. Then it moves to the left from 16 °C to 9 °C and increases linearly, overlapping the boiling curves of HPEE-1 with 2.0 ml of liquid inside.

As the temperature difference of the condenser and HPEE-1 evaporator of 4.0 ml at 0.02 - 0.2 MW/m^2 close to the conduction only model, which means that the nucleate boiling regime is not activated. Heat transfer remains in the mode of evaporation on the free surface of a saturated liquid layer and only through conduction, so the heat transport capability is low. The decrease of 4.0 ml at 0.2 MW/m^2 corresponds to the change in the mode to capillary-fed boiling in sintered porous [Weibel and Garimella 2013].

From 0.2 to 0.4 MW/m^2, the boiling curves of 1.5 ml, 2.0 ml, and 4.0 ml overlap with almost the same sub-superheat. This means that HPEE-1 with 1.5 ml of liquid inside is already close to the capillary-fed boiling regime when the heat flux is 0.2 MW/m^2. Then, as the bubbles increase,

the boiling curve of 1.5 ml shifts to the right at 0.4 MW/m^2. At 2.2 MW/m^2, the regime changes to transient because 1.5 ml of liquid was insufficient to be condensed and flow back to the evaporator.

The HPEE-1 boiling curves with 2.0 ml increase linearly with heat flux up to 2.5 MW/m^2, meaning that it is always in the stable capillary-fed boiling regime with small bubbles because the condensed water is enough to flow back to the evaporator.

It can be concluded that when the transported heat flux is the same, as shown by Figure 4.6, the sub-superheat $\Delta T_{wall-HP04}$ reduces as liquid inventory rises. Higher liquid inventories help the HPEE stay in a boiling regime that has a higher heat transport capability and the evaporator temperature is lower. But high liquid inventory like 4.0 ml requires a higher heat flux to active nucleate boiling. It is not recommended to be used for low heat flux conditions.

From the above comparisons, HPEE-1 with 2.0 ml has the best heat transfer capacity in four liquid inventories, which stays in the capillary-fed boiling regime from 0.2 to 3.2 MW/m^2. The 4.0 ml liquid inventory is too much for HPEE-1, which requires a higher heat flux to activate the nucleate boiling. Previously, HPEE-1 with 4.0 ml only transmits heat through the conductivity of the envelope and evaporation on the porous structure.

4.3 Impact of the Evaporator Design on Heat Pipe Performance

To study the possibility of improving the performance of the evaporator, the porous structures in the evaporator that feature extra open channels [Stephan and Busse 1992][Deng et al. 2017], called HPEE-2, are tested. The performance of HPEE-2 is compared with HPEE-1 by assessing the same three aspects as the HPEE-1 of the liquid inventories study in Section 5.2. Of these, the 1.5 ml liquid inventory is tested with finer data points with lower heat flux from 0.04 MW/m^2, as it meets the critical conditions more easily. Additionally, a test using HPEE-2 containing 2.0 ml of liquid, the best liquid inventory of HPEE-1, is also evaluated.

In Figure 4.7 (a), the temperature difference between the evaporator and condenser $\Delta T_{evap-cond}$ of the HPEE-2 with 1.5 ml is always lower than that of HPEE-1. It first increases linearly with the lower slope from 0.04 -0.4 MW/m^2, then it shows a clear jump in the heat flux of 0.5 MW/m^2 from 24 °C to 54 °C, while HPEE-1 jump at 0.4 MW/m^2. Unlike HPEE-1 which increases linearly up to 2.5 MW/m^2 and jump again, the curve of HPEE-2 increase linearly until 1 MW/m^2, then $\Delta T_{evap-cond}$ fluctuates around 100 °C in a specific heat flux range. Finally, it jumps directly from 95 °C to 140 °C at 1.8 MW/m^2.

In comparison, $\Delta T_{evap-cond}$ of HPEE-2 containing 2.0 ml of water in Figure 4.7 (b) increases linearly as a function of the heat flux with a slope lower than HPEE-1. It doesn't show a jump and

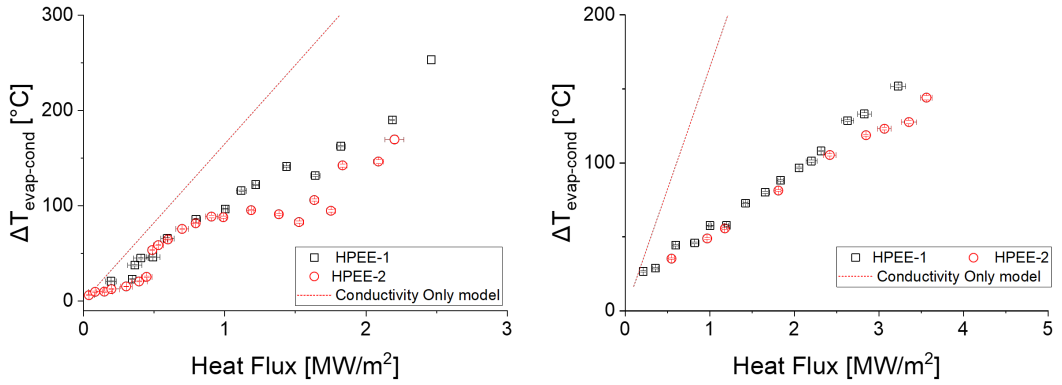

(a) (b)

Figure 4.7: Measured temperature difference between evaporator and condenser as a function of applied heat flux for HPEE-1 and HPEE-2 with liquid inventories (a) 1.5 ml (b) 2.0 ml, comparing with the 'conductivity only model'.

.

$\Delta T_{evap-cond}$ finally equals to 127 °C at 3.6 MW/m^2. While HPEE-1 with 2.0 ml stopps at lower heat flux around 3.2 MW/m^2 with higher difference value 150 °C.

The experiments of both mock-ups are stopped due to the evaporator temperature is close to 350 °C, and the electric copper heater is close to its limiting working temperature of 750 °C. But mock-ups show the potential to accept more heat flux higher than the end of experiments, as the curve of 2.0 ml is still linear without a sudden temperature rise and below the conduction only model.

The temperature difference of HPEE-2 with two liquid inventories is always lower than HPEE-1, as well as the conduction-only model, without observing any dry out. This is due to the fact that for HPEE-2, the liquid-vapor meniscus recedes into the channels of the porous structure and the effective heat transfer thickness where the channels are half that of HPEE-1. Thus, the effective heat resistance is reduced between the vapor and the porous structure. Water evaporation and vapor convection in HPEE-2 are initiated easier than in HPEE-1 as well.

$\Delta T_{evap-cond}$ of HPEE-2 fluctuates around 100 °C from 1.0-1.5 MW/m^2 is further studied with the boiling curves. With a finer resolution of heat flux data points from 0.04 MW/m^2, the curve shift behavior related to the boiling curve regimes can be seen much clearer in the low heat flux range with HPEE-2 when it contains 1.5 ml.

As shown in Figure 4.8 (a), the boiling curve of HPEE-2 increased linearly with lower sub-superheat $\Delta T_{wall-HP04}$ than HPEE-1 up to 0.4 MW/m^2, but with high uncertainty. Then, $\Delta T_{wall-HP04}$ shifted to the right at 0.5 MW/m^2 from 10 to 35 °C. From 0.5-0.8 MW/m^2, the sub-superheat of HPEE-2 is almost the same as HPEE-1. Around 1 MW/m^2, the $\Delta T_{wall-HP04}$

shifts back to the left from 70 °C to 50 °C, while HPEE-1 doesn't shift with a higher sub-superheat of 103 °C. After 2 MW/m^2, $\Delta T_{wall-HP04}$ increases quickly again but heat flux changed little, indicating a decrease in heat transfer capacity.

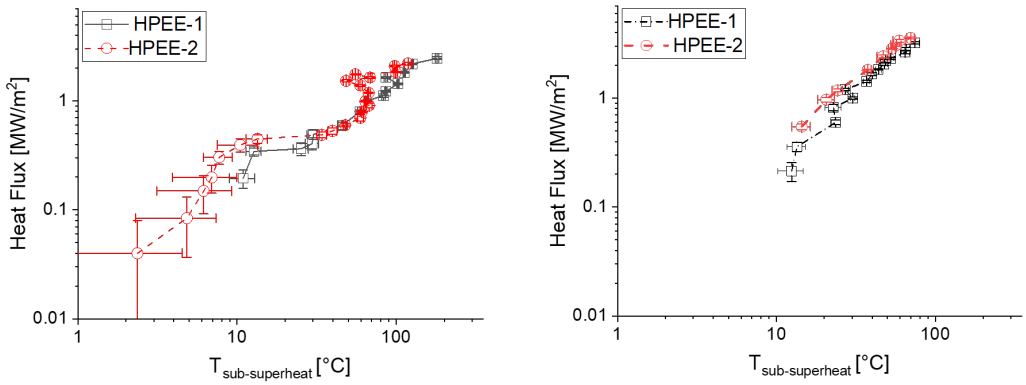

Figure 4.8: Measured boiling curves that heat flux as a function of the sub-superheat $\Delta T_{wall-HP04}$ for HPEE-1 and HPEE-2 with liquid inventories (a) 1.5 ml (b) 2.0 ml.

This behavior can be explained by the fact that during low and medium heat flux, the heat transfer mechanism of the porous channels is dominated by the capillary-fed boiling mode such as HPEE-1 with a plain porous structure. The channels provide a lower resistance path for the vapor bubbles to escape [Mughal and Plumb 1996] compared to the plain evaporator in HPEE-1, thus allowing the bubbles to escape. The capillary force in the channels drives more liquid flows to the evaporator. But at a high heat flux of 1 MW/m^2, the vapor bubbles produced are more and move rather quickly, the heat transfer mechanism of the porous microchannel switches to a convection vapor boiling mode, in which the bubble and annular flow patterns are observed in the porous channels [Qu et al. 2012][Zhang et al. 2020], as shown in Figure 4.9.

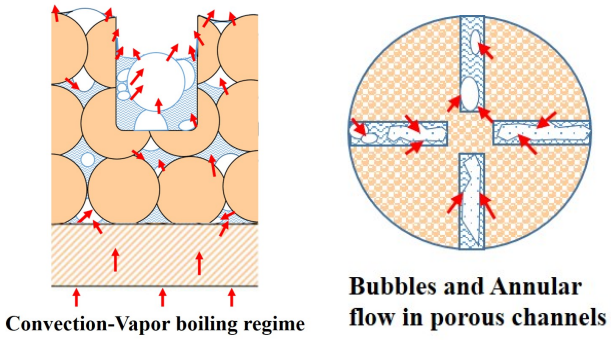

Figure 4.9: Schematic illustrations of the convection vapor boiling regimes (a) look into the bubbles in channels and menicus, (b) top view of the bubble flow in porous channels.

In this mode, the meniscus between the vapor and liquid is increased, which plays an important role for heat and mass transfer. High vapor flow in channels also increase the heat transfer capacity and delay the onset of a transient-boiling regime. When applied heat flux is continually increased, the convection vapor boiling mode changes to the transient boiling regime as well, because of the lack of liquid.

The boiling curve of HPEE-2 with 2.0 ml has almost the same linear trends as HPEE-1, showing no horizontal jump until 3.6 MW/m^2. When transporting the same heat flux, $\Delta T_{wall-HP04}$ of HPEE-2 is always lower than that of HPEE-1. At 3.2 MW/m^2, the sub-superheat of HPEE-1 is 78 °C, and that of HPEE-2 is 70 °C.

It indicates that when liquid is enough, the HPEE-2 evaporator performs better because the bubbles in the porous structure of the evaporator with channels come out easier than the normal porous plate, leaving more space for the flow of condensed liquid. Meanwhile, HPEE-2 has lower effective evaporator heat resistance than HPEE-1, and the temperature gradient from the vapor T_{HP04} to the T_{wall} is reduced as well.

The temperature difference between the evaporator and the condenser shows the heat transfer capability of the HPEE, while the heat transfer characteristics of the evaporator $HTCH_{evap}$, which focuses on the heat transfer capability of the two different evaporator structures, are presented in Figure 4.10. It is a function of the heat flux Q [W/m^2] dividing the temperature difference $\Delta T_{wall-HP04}$ [K] between the temperature at the interface of the evaporator CuCrZr plate and the porous structure and vapor temperature at HP04: $\frac{Q}{\Delta T_{wall\text{-}HP04}}$. The $HTCH_{evap}$ increases as liquid inventory increases.

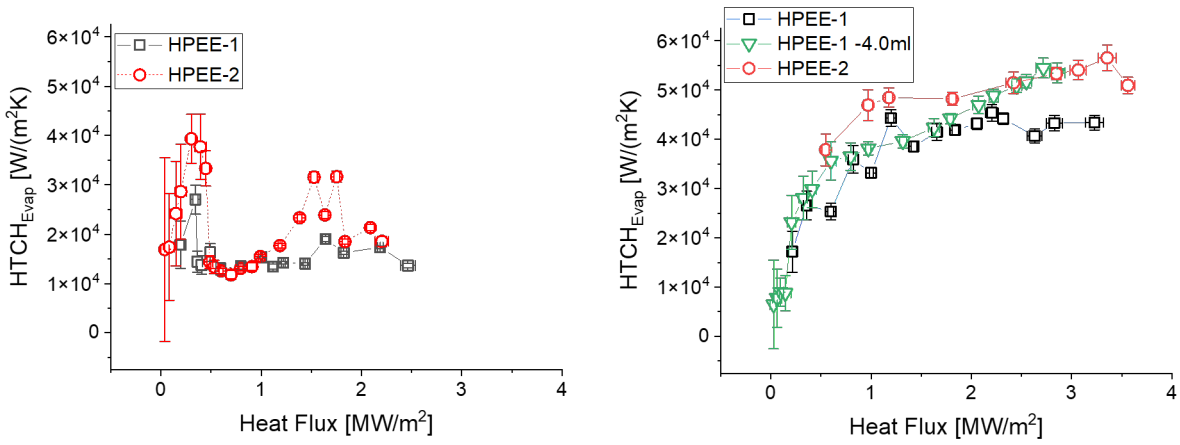

Figure 4.10: Measured heat transfer characteristic of the evaporator $HTCH_{evap}$ as a function of applied heat flux for HPEE-1 and HPEE-2 with liquid inventories (a) 1.5 ml (b) 2.0 ml.

The heat transfer characteristic $HTCH_{evap}$ of HPEE-2 is higher than HPEE-1 when HPEE-1 and HPEE-2 are filled with the same liquid inventory. A peak value of 4×10^4 W/(m^{2}K) of HPEE-2 with 1.5 ml of liquid is presented at 0.4 MW/m^2 in Figure 4.10 (a), higher than HPEE-1 by 1.2×10^4 W/(m^{2}K), then it drops to 1.4×10^4 W/(m^{2}K). But at 1.5 MW/m^2, the $HTCH_{evap}$ rise again to 3.5×10^4 W/(m^{2}K) because the channel supports changes the boiling regime. At 2 MW/m^2, although $HTCH_{evap}$ returns back to 2.0×10^4 W/(m^{2}K), it is still higher than HPEE-1.

As shown in Figure 4.10 (b), starting from 0.4 MW/m^2, the $HTCH_{evap}$ of HPEE-2 containing 2.0 ml liquid fluctuates between 4×10^4 W/(m^{2}K) and 5×10^4 W/(m^{2}K) up to 2.9 MW/m^2. It is always higher than HPEE-1 with 2.0 ml liquid by 1×10^4 W/(m^{2}K) in the entire test range, even higher than the one of HPEE-1 with 4.0 ml.

Because of the higher $HTCH_{evap}$ and lower sub-superheat of HPEE-2 than HPEE-1, the evaporator temperature is much lower than the experiments' maximum temperature limits. Then, instead of ending at 2.8 MW/m^2 like HPEE-1, the HPEE-2 with 2.0 ml liquid stays in the capillary-fed boiling regime until 3.5 MW/m^2 with potential to sustain higher heat flux.

From the above comparisons, HPEE-2 with channels on a porous evaporator performs better than HPEE-1. When liquid inventory is not enough like 1.5 ml, the channels on porous evaporator structure provides a low flow resistance path for the vapor to escape from the porous to vapor space in the HPEE, helping evaportaor stay in the capillary-fed boiling regime at low heat flux. When the applied heat flux is high, the channel in the porous structure creates an extra convection boiling mode in which bubbles flush onto the channels and take some heat to the vapor space, improving the heat transfer capability of HPEE-2 at high heat flux and keeping the HPEE-2 evaporator at a relatively low temperature.

4.4 Dependence of Heat Sink Conditions on Heat Pipe Performance

The investigation of the temperature measurements of two mock-ups with different liquid inventories is discussed under a constant heat sink flow rate of 90 l/h, as introduced as level 'i' in Chapter 4. It is used for cooling the mock-ups in low heat flux test ranges to guarantee that the temperature rise of the coolant is high enough and reduce the relative uncertainty of the calorimetric power evaluation.

However, at high heat flux, the heat transfer capability was limited due to the boiling regime changing in HPEEs. Meanwhile, an increased condenser temperature and, consequently, a higher vapor temperature also influence the HPEE. As a result, the temperature of the evaporator increases very quickly. Therefore, the effects of the heat transfer capability of the heat sink on two HPEEs are

investigated by varying the flow conditions. In addition to the existing test results with a constant flow rate of 90 l/h as level 'i', the other two flow rates as level 'ii' to control the temperature difference between the input and outlet at 8 °C and level 'iii' to keep the condenser temperature constant around 83 °C are investigated.

Since the higher flow rate test is interested in the high heat flux range, the experiments start from 2.0 MW/m^2, where the temperature difference at the inlet and outlet is 10 °C with a constant flow rate of 90 l/h. The performance of HPEE-2 containing 1.7 ml and 2.0 ml liquid is presented.

The temperature difference between the evaporator and condenser $\Delta T_{evap-cond}$ as a function of the heat flux with different flow rate control methods is presented in Figure 4.11.

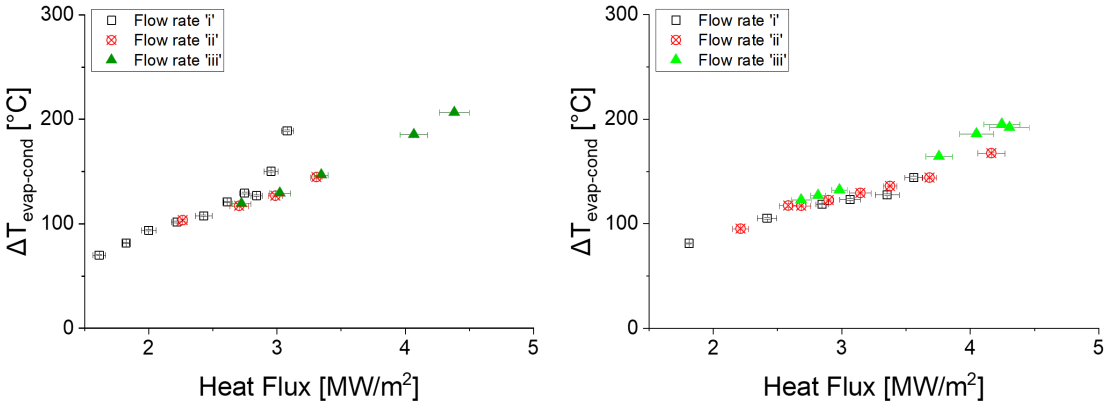

Figure 4.11: Measured temperature difference of HPEE-2 between evaporator and condenser as a function of applied heat flux with different flow rates and liquid inventories (a) 1.7 ml (b) 2.0 ml.

It illustrates that the change in flow rate has little influence on the $\Delta T_{evap-cond}$. For HPEE-2 with 1.7 ml, $\Delta T_{evap\text{-}cond}$ has a significant rise at 3 MW/m^2 when the flow rate is 90 l/h. While $\Delta T_{evap\text{-}cond}$ of HPEE-2 increase linearly with unchanged slope when cooled with higher flow rates 'ii' and 'iii'. The flow rate 'iii' results in an extension of the operating range up to 4.38 MW/m^2.

It is because when with a flow rate of 90 l/h, the heat transfer capability is not high enough to cool the condenser, the liquid cannot flow back to the evaporator in time, resulting in the capillary-fed boiling changing to transient boiling, and the evaporator temperature increases. When HPEE-2 is cooled by a high enough flow rate, such as 'ii' or 'iii', the condenser and vapor temperature are cooled down, and the required mass flow is lower for the same load, succeeding the two-phase loop circulates. Then, the evaporator temperature is lower, and the porous structure of the evaporator is in the capillary-fed boiling regime. As the evaporator temperature is reduced significantly with flow rate 'iii', far from the working temperature limit, the experiment goes further with higher heat flux.

HPEE-2 with 2 ml of liquid does not experience an non linear increase in its $\Delta T_{evap\text{-}cond}$ like with 1.7 ml liquid at 3 MW/m^2 when cooled with a flow rate of 90 l/h. Even with higher flow rates, the $\Delta T_{evap\text{-}cond}$ of HPEE-2 with 2 ml remains similar. This is because the porous structure is always in the capillary-fed boiling regime, and the evaporator temperature is in a low range.

HPEE-2 experiments with 2 ml liquid cooled by flow rate 'i' stop at 3.5MW/m^2, and cooled by 'ii' stop at 4.0MW/m^2 because the evaporator temperature increases rapidly, and the working temperature of the copper heater reaches its limitation. Although $\Delta T_{evap\text{-}cond}$ with flow rate for a fixed condenser temperature 'iii' is higher than working with a fixed temperature rise of the coolant 'ii', the heat pipe can transport higher heat fluxes up to 4.3MW/m^2. The mock-up does not show a worse state of its heat transport capabilities, as it still increases as a function of the heat flux linearly, without slope changing. Hence, it is not straightforward to say which case would perform better.

Therefore, the influence of flow rate on the heat transfer characteristic HTCH$_{evap}$ as a function of the heat flux is studied. Figure 4.12 (a) shows that before 3 MW/m^2, the heat transfer characteristic HTCH$_{evap}$ is almost same around 4.5×10^4 W/(m^{2}K) when cooled by three flow rate levels. After 3 MW/m^2, HTCH$_{evap}$ drops from 4.5 to 3×10^4 W/(m^{2}K) when cooled by flow 'i' 90 l/h, while other stay around 4.5×10^4 W/(m^{2}K) until 4 MW/m^2. It means that higher flow rates 'ii' or 'iii' only have an positive influence after 3 MW/m^2.

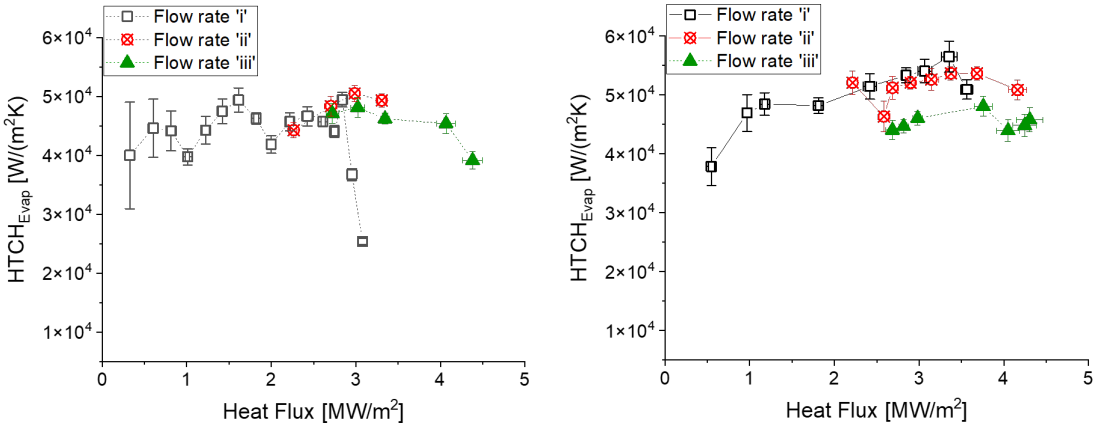

Figure 4.12: Measured heat transfer characteristic of the HPEE-2 evaporator HTCH$_{evap}$ as a function of the applied heat flux with different flow rate modes and liquid inventories (a) 1.7 ml and (b) 2.0 ml.

HTCH$_{evap}$ of HPEE-2 with 2.0 ml with flow rate 'i' and 'ii' is amost same, around 5×10^4 W/(m^{2}K) from 2 to 3.5 MW/m^2, as shown in Figure 4.12 (b). When coolant flow rate increased to 'iii',

keeping condenser temperature low, the curves even show a decreased heat transfer characteristic $HTCH_{evap}$ around 5×10^4 W/(m^{2}K).

Table 4.1 lists the temperature measurements of HPEE-2 with 2.0 ml with specific imposed heat flux when cooled by heat sink flow rates controlled by three methods. It can be found that the evaporator temperature T_{evap} reduces when flow rate is higher. But the reducing gradient of the evaporator temperature is not significant compared to the one of vapor and condenser temperatures. At 2.8MW/m^2, when the flow rate is increased from 'i' to 'ii,' the evaporator temperature is decreased by around 8 °C, and the vapor and condenser temperatures are reduced by 11 and 16 °C, respectively, which are reduced almost 37% and 100% more than T_{evap}.

Table 4.1: Measured temperatures at HPEE-2's evaporator, vapor, and condenser when cooled with different flow rates control method at specific imposed heat flux.

HPEE-2	**2.8 MW/m^2**			**3.4 MW/m^2**		
	T_{evap} **[°C]**	T_{vapor} **[°C]**	T_{cond} **[°C]**	T_{evap} **[°C]**	T_{vapor} **[°C]**	T_{cond} **[°C]**
i	243	175	128	273	196	146
ii	235	164	112	257	176	121
iii	215	135	83	230	145	84
$T_{reduced}$ i-ii	8	11	16	16	20	25
$T_{reduced}$ i-iii	28	40	45	43	51	62

This is because when the flow rate increases, the influence of the heat transfer coefficient of the heat sink is mainly applied to the condenser temperature, which drops first with high gradient. Then, through the effective thermal conduction, the saturation pressure and temperature of vapor in HPEE decrease. The evaporator temperature is therefore reduced because the boiling in the porous structure keeps the superheat between the vapor and the evaporator as low as possible. However, as the high heat flux is applied on the evaporator, the evaporator temperature is much sensitive with heat source, as the high heat flux is applied on the evaporator, rather than the heat transfer coefficient of the heat sink.

As a result, when the flow rate is increased by changing the controlling method from 'i' to 'ii' or 'iii,' vapor and condenser temperatures drop faster than evaporator temperatures. Hence, when applying the same heat flux, $\Delta T_{\text{wall-HP04}}$ is increased when flow rate is higher. According to the equation of heat transfer characteristic of evaporator: $\frac{Q}{\Delta T_{\text{wall-HP04}}}$, that's why heat transfer characteristic of evaporator even reduces when flow rates increase.

The same reason can explain why the temperature difference between evaporator and condenser $\Delta T_{evap-cond}$ is higher when flow rates increase. But the evaporator temperature itself decreases

when flow rates increases, making HPEE-2 can transport higher heat flux before reaching the working temperature limit.

Due to the limitation of the heat flux test range, it is challenging to define which flow rate can help HPEE performance better, as the difference between them is little. To avoid the HPEE meeting the critical temperature limit quick, the flow rate keeping condenser temperature constant and low 'iii' is better, as it can keep evaporator temperature as low as possible. But when considering the heat transfer capability and economic efficiency, the flow rate keeping coolant temperature rise constant 'ii' is enough.

The discussion above indicates that when HPEE-2 with 2.0 ml of liquid inventory, cooled by flow rate 'ii', which is adjusted to keeping $\Delta T_{coolant,out\text{-}in}$ around 8 °C is better than others, when considering economic efficiency, as used in the fusion reactor. The higher flow rate reduce the evaporator temperature far from the critical temperature limits, but it reduces the heat transfer capability of the HPEE-2.

4.5 Verification of Analytic Heat-Pipe-Model by Experimental Results

Average value of the experimental temperatures at HPEE-1's three sections with liquid inventories 1.5 ml and 2.0 ml is compared with the value from the engineering analytic heat-pipe-model, using the same approaches for designing the divertor heat pipe, as introduced in Chapter 3.

Because the evaluation of the temperature chain starts from the inlet coolant temperature $T_{cool,in}$, and the heat transfer coefficient of the heat sink is considered in the analytical model, there are two analytical models named Model 'i' and Model 'ii', which relate to different flow rate conditions in the experiments: with constant flow 90 l/h 'i' and with adjusted flow rate 'ii', keeping coolant temperature rise constant at 8 °C.

At first, the condenser temperature where thermocouples exist is predicted with the inner diameter of the heat sink jet D = 3 mm as in the design. By comparing the experimental measurements of HPEE-1 containing 1.5 ml and 2.0 ml of liquid with the results of the analytical model, Figure 4.13 (a) and (b) indicate that the measured condenser temperature at flow rates 'i' and 'ii' exhibit a higher value than the analytical models Model- 'i' and Model- 'ii'.

It is the result of the manufacturing process. At first, the inner diameter of the nozzles D=3+0.5 mm after measuring. Then, a drilling process after the nozzle tube is cut to its proposed length makes a chamfer at the end of the jet nozzle with a bigger inner diameter, to which the heat sink coefficient is sensitive. Meanwhile, the inlet and outlet tube cannot remain coaxially in the

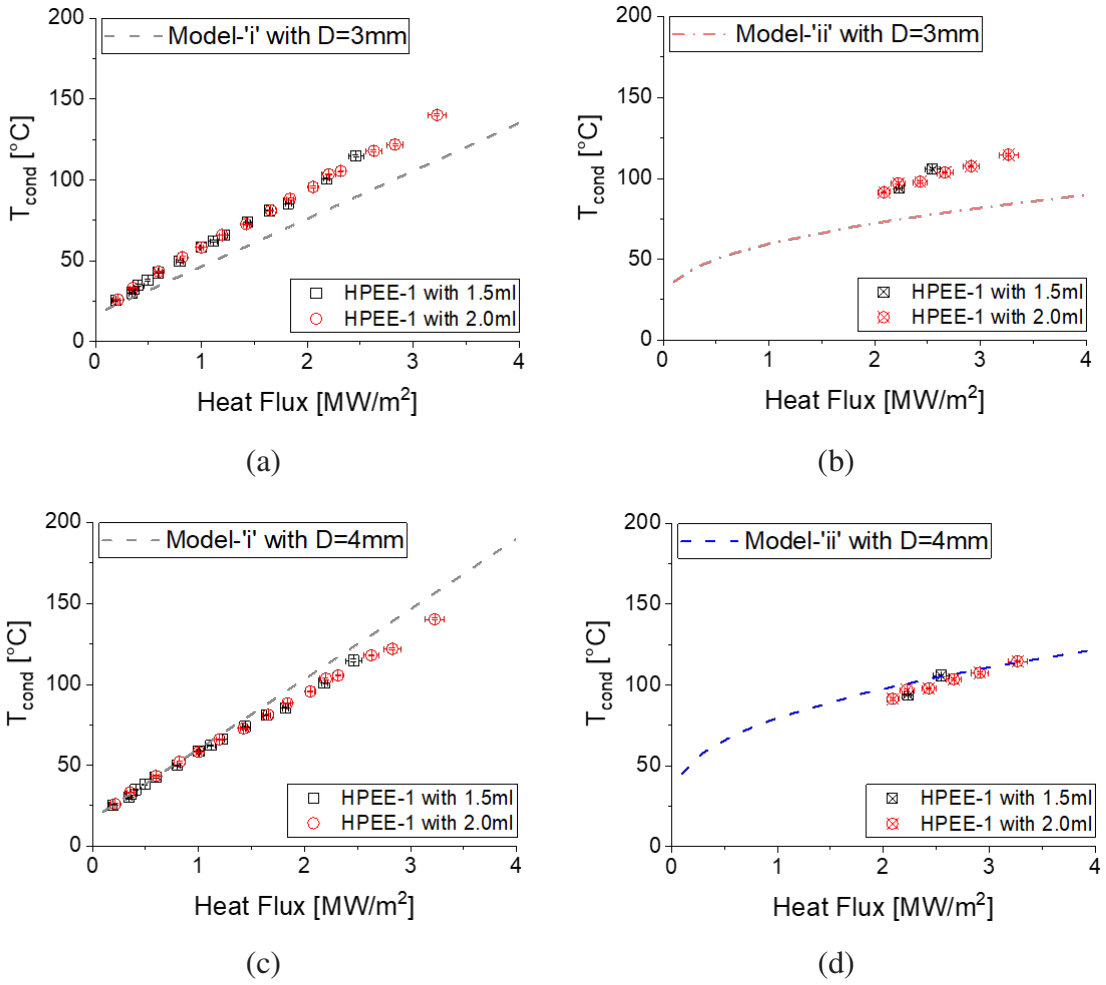

Figure 4.13: Measured condenser temperature as a function of applied heat flux for HPEE-1 with liquid inventories 1.5 ml and 2.0 ml and different heat sink flow rates, comparing with the analytic model (a) Model-'i' with nozzle inner diameter D=3 mm (b) Model-'ii' with nozzle inner diameter D=3 mm (c) Model-'i' with nozzle inner diameter D=4 mm, (d) Model-'ii' with nozzle inner diameter D=4 mm.

installation procedure, and the Teflon band is used as the sealing material between the jet and the HPEE head. Hence, the jet coolant distance from the nozzle to the condenser surface, which influences the heat transfer coefficient of the heat sink, is difficult to guarantee.

Figure 4.13 (c) and (d) present that the measured condenser temperature at flow rates 'i' and 'ii' is much closer to the value predicted by two models with jet nozzle D=4 mm, which is used as a reference model later.

The measured vapor temperature T_{vapor} is compared with the value based on the predicted condenser temperature of two models by assuming that the vapor temperature is the same as the temperature on the inter surface between the vapor and liquid film that covers the inner surface of

the condenser. Figure 4.14 indicates that the measured vapor temperature at HP03 T_{HP03} equals T_{HP04} in the entire test range. Vapor temperatures in two models are close to the predicted vapor temperature when considering the liquid film with an average thickness of 0.055 mm and an average heat conductivity 0.65 W/(mK) on the condenser inner surface from 1MW/m^2 to 5MW/m^2.

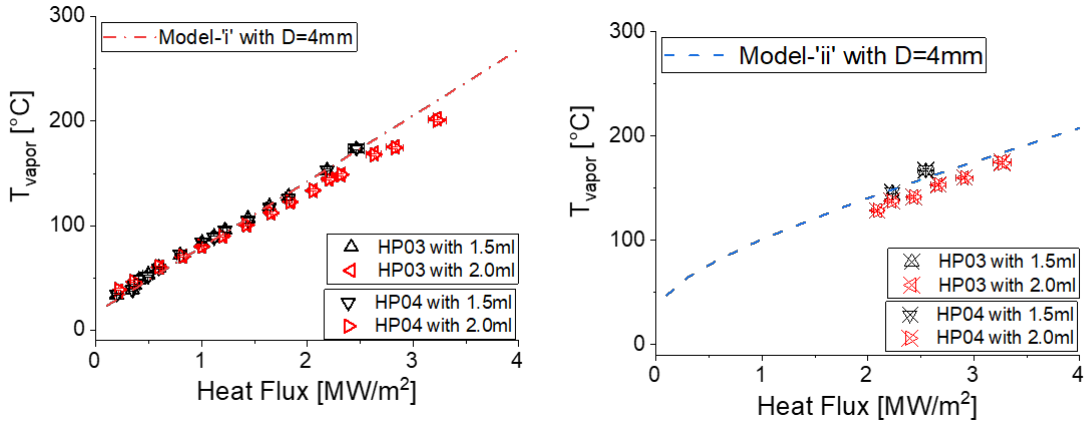

(a) (b)

Figure 4.14: Measured vapor temperature as a function of applied evaporator heat flux for HPEE-1 with liquid inventories 1.5 ml and 2.0 ml and different heat sink flow rates, comparing with the analytic model with nozzle inner diameter D=4 mm (a) Model-'i', (b) Model-'ii'.

Therefore, it shows that the temperature in the center of HPEE is nearly uniform when water is saturated. The liquid inventory has almost no influence on the vapor temperature with heat flux. A liquid film that covers the inner surface of the condenser plays an important role in the effective thermal resistance. Because the model uses the average thickness of the liquid film and the heat conductivity, when the heat flux increases, the difference between the experimental value and the model is greater, which is 10% at 5MW/m^2. Due to the geometry constraint of the mock-up, the saturation pressure, relating to the saturation temperature, is not detectable for a precise analysis.

The evaporator temperature is estimated considering the vapor temperatures equal to the temperature at the vapor-liquid interface in two models, as presented in Figure 4.15. It shows that in Model'i' and Model'ii', only when the liquid inventory is 1.5 ml, the measured evaporator temperature of HPEE-1 is close to the model value in coincidence. When liquid inventories increase to 2.0 ml, the measured evaporator temperature of HPEE-1 increases linearly with heat flux but with a smaller slope than the increasing slope of the model. At 3 MW/m^2, the predicted evaporator temperature of HPEE-1 in Model 'i' is 450 °C, but the experimental measurement with 2.0 ml liquid is only 300 °C, with a different percentage of 50%. And the predicted evaporator temperature of HPEE-1 in Model 'ii' is 440 °C at 3 MW/m^2, but the experimental measurement is 260 °C, with a different percentage of 41%.

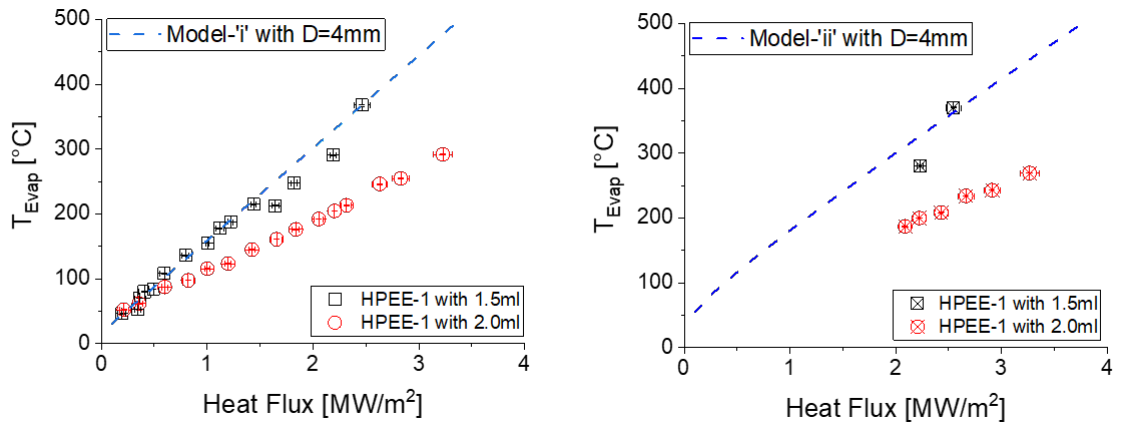

(a) (b)

Figure 4.15: Measured evaporator temperature as a function of applied evaporator heat flux for HPEE-1 with liquid inventories 1.5 ml and 2.0 ml and different heat sink flow rates, comparing with the analytic model with nozzle inner diameter D=4 mm (a) Model-'i', (b) Model-'ii'.

Then, the Model 'i' and Model 'ii' of HPEE-2 evaporator temperature are established, as shown in Figure 4.16. They are also estimated by considering vapor temperatures equal to the temperature at the vapor-liquid interface. The heat resistance of the porous structure with channels is altered by assuming the effect heat transfer thickness is 1.5 mm instead of 2 mm thick as a porous plate. This is because the liquid-vapor meniscus retreats into the channels of the porous structure.

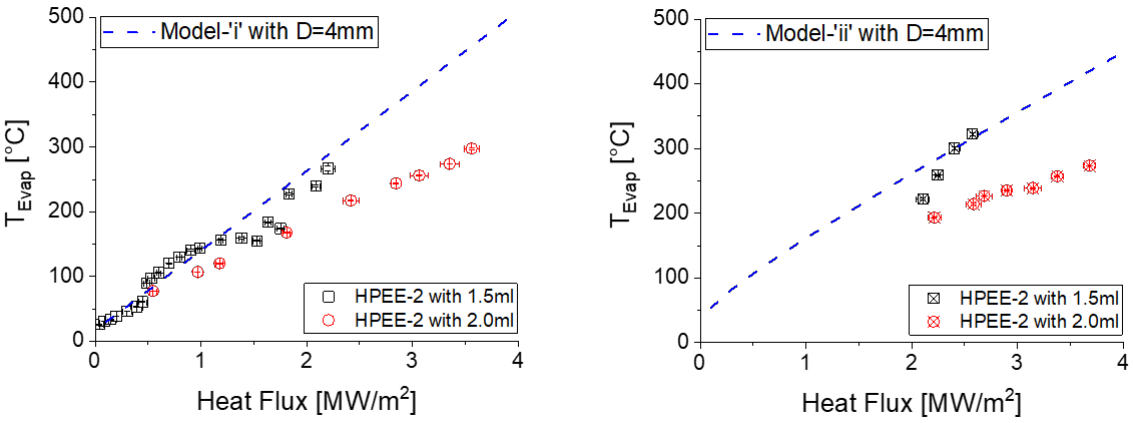

(a) (b)

Figure 4.16: Measured evaporator temperature as a function of applied evaporator heat flux for HPEE-2 with liquid inventories 1.5 ml and 2.0 ml and different heat sink flow rates, comparing with the analytic model with nozzle inner diameter D=4 mm (a) Model-'i', (b) Model-'ii'.

At 3 MW/m^2, the predicted evaporator temperature of HPEE-2 in Model 'i' is 400 °C, and the predicted evaporator temperature of HPEE-2 in Model 'ii' is 375 °C. The evaporator temperature

of HPEE-2 in Model 'i' and Model 'ii' is lower than that of HPEE-1 because HPEE-2 with channels in porous structures has a lower effective heat resistance.

When the liquid inventory is 1.5 ml, the measured evaporator temperature of HPEE-2 is close to the value of both models like the HPEE-1. When liquid inventories increase to 2.0 ml, the measured HPEE-2 evaporator temperature increases linearly with heat flux with a slope smaller than the increasing slope of the model. At 3 MW/m^2, the experimental evaporator temperature of HPEE-2 with 2.0 ml is only 265 °C when cooled with flow rate 'i', it is 34% lower than the value of Model 'i'. And the experimental evaporator temperature of HPEE-2 is 250 °C when cooled with flow rate 'ii', 33% lower than the predicted value in Model 'ii'.

When containing 2.0 ml of liquid, the experimental evaporator temperature rise with heat flux is less than what is predicted by engineering analysis Models 'i' and 'ii' for HPEE-1 and HPEE-2. However, when with 1.5 ml of liquid, such phenomena are not observed. When the heat flux is high, the mock-up with 1.5 ml of water has already reached the transient regime, and the effective heat resistance of the working heat pipe is close to the one estimated in the engineering analysis model. When containing 2.0 ml of water, the capillary-fed boiling in the porous evaporator optimizes the effective heat resistance, keeping the evaporator much lower than the predicted value.

The HPEE-2 temperatures with a bronze porous structure B200 evaporator, featuring eight channels, are shown in Table 4.2. These temperatures were estimated using Model-'i' and Model-'ii' with a heat sink jet of diameter 4 mm up to 5 MW/m^2. The evaporator temperature T_{evap} reaches 510 °C with bronze porous at maximum heat flux of 4 MW/m^2 according to Model-'i', while T_{evap} reaches 449 °C at a heat flux of 4 MW/m^2, and 541 °C at a heat flux of 5 MW/m^2 in Model-'ii'.

Table 4.2: Estimated vapor and evaporator temperature with capillary structures B200 until 5 MW/m^2 based on Model-'i' and Model-'ii'.

Heat flux	**Model-'i'**			**Model-'ii'**		
[MW/m^2]	$T_{en,i,cond}$ **[°C]**	T_{vapor} **[°C]**	T_{evap} **[°C]**	$T_{en,i,cond}$ **[°C]**	T_{vapor} **[°C]**	T_{evap} **[°C]**
1	62.4	79.7	140.1	82.1	101.3	161.8
2	107.8	142.5	263.3	102.2	140.7	261.4
3	153.4	205.5	386.6	117.7	175.4	356.5
4	199.3	268.8	510.3	131.0	207.9	449.4
5	245.7	332.5	634.4	142.9	239.0	540.9

The HPEE-2 experiment revealed that when the liquid inventory was 2.0 ml at 4.3 MW/m^2, the evaporator temperature was lower than expected, reaching 275 °C. This implies that the HPEE-2

performed better than what was predicted by both models. The capillary-fed boiling behavior in the porous structure of the HPEE encourages the movement of vapor bubbles, which in turn enhances its heat transfer capability and reduces the effective heat resistance. Meanwhile, HPEE-2 has not experienced a sudden rise in temperature when the heat flux is increased, suggesting that it has the potential to handle higher heat fluxes than 4.3 MW/m^2. The estimation for HPEE with copper porous structure C120 in Appendix C predicts that the evaporator temperature of HPEE-2 based on the Model-'ii' is only 282 °C at 5 MW/m^2, which means that the heat conductivity is the main reason that restricts the experiment for HPEE with bronze porous structure.

Furthermore, at 5 MW/m^2, the vapor temperature of HPEE-2 with Model 'ii' is already reached 282 °C, close to the design of the maximum operational vapor temperature for the divertor heat pipe. Because the heat resistance of the film thickness on the inner condenser surface plays an important role in the temperature chain.

This is not an issue for the divertor heat pipe DIV-HP. The HPEE does not have the capillary structure on the condenser, while the open groove capillary structure covers the DIV-HP's condenser, fully containing the condensed liquid inside. Hence, the vapor temperature of HPEE is equal to the vapor-liquid interface temperature, while the vapor temperature of DIV-HP is equal to the interface temperature of the vapor-capillary structure, calculated by the effective heat resistance of the condenser capillary structure $R_{c,evap}$ as discussed in Chapter 2.

As the experimental vapor temperature around 200 °C is closed to the operational temperature designed for divertor heat pipe, The validation of the engineering analysis model of HPEE can also be concluded for the DIV-HP with a copper porous structure. With the same design approach and engineering analysis model, the maximum evaporator temperature of DIV-HP is 350 °C when applied power is 20 MW/m^2, lower than the working temperature limit. The comparison of the results between the experiment and the analytic model of the HPEE showed that when the liquid inventory is sufficient, the actual operational evaporator temperature is lower than the value predicted in the model with same heat flux. This is due to the optimization of the effective heat resistance caused by capillary-fed boiling.

Consequently, the operational evaporator temperature of DIV-HP can be lower than the estimated 350 °C when the applied power is 20 MW/m^2, which is a positive indication that the divertor heat pipe can function properly under the conditions of a DEMO divertor.

5 Synopsis and Outlook

5.1 Synopsis

This dissertation examines the potential of using a water-based heat pipe as a heat sink in the DEMO fusion reactor divertor target, which is capable of withstanding heat fluxes of up to 20 MW/m^2. To this end, effective heat resistance and performance limits analysis approaches are employed to dimension a water-based heat pipe for the divertor DIV-HP with a combined capillary structure. However, because of the complex structure and uncertain heat transfer capability when the boiling limit is reached, experiments are conducted with a specific mock-up HPEE, which focus on the performance of the heat pipe evaporator, where the boiling limit is easily reached.

This research contributes significantly to the knowledge of the factors, such as structures, liquid inventories, and the flow rates of the heat sinks, that affect the use of water-based heat pipes in the DEMO divertor target. Two specific mock-ups with different evaporator porous structures have been tested in experimental campaigns. The first mock-up (HPEE-1) features a plain porous structure and the second mock-up (HPEE-2) has additional channels. The behavior of the two mock-ups is analyzed by monitoring the temperature measurements with increasing heat flux.

The HPEE-2 (including channels on the evaporator's surface) with 2.0 ml water and the flow rate 'ii' (for controlling the temperature difference between the intake and exit of the coolant at 8 °C) has better performance until 4.3 MW/m^2 and still in the stable nucleate boiling regime. The experimental condenser and vapor temperature fit well with the analytic model. However, the evaporator temperatures of the experiment results are lower than the value predicted by the analytic model, especially when the liquid inventory is 2.0 ml, indicating the possibility that the HPEE performs better than the prediction from the analytic model. The capillary-fed regime in the heat pipe evaporator optimizes the effective heat resistance calculated in engineering model. Validation of the engineering analysis model gives positive insight that the divertor heat tube can be used in the DEMO divertor target, transferring a maximum heat flux of 20 MW/m^2.

The results of the HPEE experiments are already better than the prediction of water-based heat pipes for handling 2 MW/m^2 heat flux in high heat flux fusion applications Rosenfeld and

Lindemuth [1993], which only reaches 0.525 MW/m^2 in experiments. The results are also close to the value tested by Weibel Weibel and Garimella [2012], and shows the potential to go further.

It shows an improvement in the heat transfer coefficient of the heat pipe by around 10 % compared to HPEE-1, as it has a lower effective heat resistance and the boiling behavior is improved when in channels. The 2.0 ml liquid inventory, corresponding to 2.6 % of vapor space, is optimal to improve the performance of the heat pipe. Little water makes the porous evaporator in the transient boiling regime, while too much liquid accumulates over the capillary structure, causing pool boiling, reducing the heat transfer capability when applying low heat flux. The influence of the heat sink flow rate on the heat transfer capability of the heat pipe is small. A higher flow rate reduces the condenser temperature, and then the evaporator temperature, making it far from the critical working temperature when the heat flux increases.

Some deductions for the DIV-HP divertor heat pipe can be concluded according to the validation of the HPEE analytic model. According to the calculation in Chapter 2, when the heat flux reaches 20 MW/m^2, the vapor temperature is around 245 °C, assuming that the condenser is covered with a fully liquid filled capillary structure. The evaporator temperature of the DIV-HP is around 350 °C, far from the working temperature limit. The results of the HPEE experiment show that the operational performance of HPEE is better than the value predicted in the anlytic model. Hence, there is a high potential that DIV-HP works well when the applied heat flux is 20 MW/m^2. Furthermore, if the optimized porous structure of the evaporator that contains channels is used for DIV-HP, the evaporator temperature will be much lower and perform better.

The HPEE experiment showed that the heat pipe can still function at higher heat flux even if the liquid is not sufficient. This is true for both the capillary-fed boiling regime and the transient boiling regime. Even if the liquid is not enough, DIV-HP can still work with a heat flux around 20 MW/m^2. In this case, the evaporator temperature will increase, but it will not reach the dry out. If there is an excessive amount of liquid covering the condenser, the heat resistance of the liquid layer will lead to an increase in the vapor temperature. Furthermore, if there is too much liquid covering the evaporator, the boiling process will only be initiated at a higher heat flux. Hence, the liquid needed in the capillary structure and the vapor space for the divertor heat pipe must be strictly controlled. At heat flux 1 MW/m^2, the liquid inventory is approximately 4.5 ml, and at heat flux 20 MW/m^2, the liquid inventory needed is around 4.9 ml, with little difference. For safety reasons, 0.5-1 ml more liquid can be added to the divertor heat pipe.

The higher flow rate of the external heat sink can reduce the evaporator temperature of the divertor heat pipe so that the heat pipe can transport higher heat flux without meeting critical working temperatures. According to the current calculation, the heat transfer coefficient of the external cooling system for the baseline divertor target is sufficient to be used to cool the divertor heat tube.

5.2 Outlook

As one of the first to explore the potential of water-based heat pipe technology for use in DEMO divertor applications, it offers a promising outlook for the use of water-hat pipes in high heat flux conditions. The heat pipe that can handle such a high heat flux of 4 MW/m^2 can be used in many specific conditions already, such as the blanket or first wall in the fusion reactor application and the solar energy system. The divertor heat pipe has a specific shape compared to the standard heat pipe. Its evaporator at the end of the cylindrical pipe and its composited capillary structures make it flexible for use in other specific space-limited conditions.

Due to the low heat conductivity of the bronze evaporator and the limitation of the working temperature of the heat source, the experiment is limited to heat fluxes of up to 4.3 MW/m^2. In comparison, the mock-up itself is capable of transporting higher heat fluxes. The exact behavior of the heat pipe at a higher heat flux around 20 MW/m^2 remains unknown, and more factors can be explored to improve the performance of the heat pipe in the target of the DEMO divertor. Meanwhile, the engineering analysis model focused on the evaporator can be optimized.

To have heat pipe experiments that can work with higher heat flux, a high-conductivity material, such as copper, sliver, and gold, can be used in a porous structure, and it should stay well on the evaporator CuCrZr plate. To reduces the influence of the heat resistance of the liquid film, the condenser capillary structure needs to be optimized, and the heat transfer coefficient of the heat sink can be enhanced. The heat source can be changed to a laser or electric beam, so that there is no heat source temperature limit. The start-up behavior of the heat pipes heated by high heat flux directly can be investigated, like plasma particles hit the divertor target.

It is possible to investigate the specifics of the channel, such as its size, quantity, and arrangement on the porous structure, which could have an effect on the heat pipe's performance. It is possible to explore other evaporator capillary structures that could improve the heat pipe's performance, such as biporous and foam structures, as well as reentrant and inverted meniscus designs.

The analytic model used now is still simple, as only the effective heat resistance through heat pipe conduction is considered. The analytic model should incorporate the heat transfer coefficient of the boiling behavior in the evaporator, which needs to be further validated with additional experimental data.

By exploring the possibility of enhancing heat pipe performance under high heat flux, it is possible to improve the performance of heat pipes utilized in the DEMO diverter target. The finalized engineering analytical model can enhance the precision of the prediction of the heat pipe behavior and give an insight to the heat flux as high as possible that the experiment cannot reach.

Bibliography

H. Cabal, Y. Lechón, U. Ciorba, F. Gracceva, T. Eder, T. Hamacher, A. Lehtila, M. Biberacher, P. E. Grohnheit, D. Ward, W. Han, C. Eherer, and A. Pina. Analysing the role of fusion power in the future global energy system. 33:01006, 2012. ISSN 21016275. doi: 10.1051/epjconf/20123301006. URL https://cris.vtt.fi/en/publications/analysing-the-role-of-fusion-power-in-the-future-global-energy-sy.

C. Bustreo, U. Giuliani, D. Maggio, and G. Zollino. How fusion power can contribute to a fully decarbonized European power mix after 2050. *Fusion Engineering and Design*, 146 (April):2189–2193, 2019. ISSN 09203796. doi: 10.1016/j.fusengdes.2019.03.150. URL https://doi.org/10.1016/j.fusengdes.2019.03.150.

K. Gi, F. Sano, K. Akimoto, R. Hiwatari, and K. Tobita. Potential contribution of fusion power generation to low-carbon development under the Paris Agreement and associated uncertainties. *Energy Strategy Reviews*, 27:100432, jan 2020. ISSN 2211467X. doi: 10.1016/j.esr.2019.100432.

B. Bigot. Preparation for assembly and commissioning of ITER. *Nuclear Fusion*, 62(4), apr 2022. ISSN 17414326. doi: 10.1088/1741-4326/AC168F.

S. Matsuda and K. Tobita. Evolution of the ITER program and prospect for the next-step fusion DEMO reactors: Status of the fusion energy RD as ultimate source of energy. *Journal of Nuclear Science and Technology*, 50(4):321–345, apr 2013. ISSN 00223131. doi: 10.1080/00223131.2013.773166. URL https://www.tandfonline.com/action/journalInformation?journalCode=tnst20.

G. Federici, C. Bachmann, W. Biel, L. Boccaccini, F. Cismondi, S. Ciattaglia, M. Coleman, C. Day, E. Diegele, T. Franke, M. Grattarola, H. Hurzlmeier, A. Ibarra, A. Loving, F. Maviglia, B. Meszaros, C. Morlock, M. Rieth, M. Shannon, N. Taylor, M. Q. Tran, J. H. You, R. Wenninger, and L. Zani. Overview of the design approach and prioritization of RD activities towards an

EU DEMO. *Fusion Engineering and Design*, 109-111:1464–1474, 2016. ISSN 09203796. doi: 10.1016/J.FUSENGDES.2015.11.050.

F. Romanelli. Fusion Electricity A roadmap to the realisation of fusion energy 28 European countries signed an agreement to work on an energy source for the future :. *Fusion Electricity - EFDA*, pages 1–75, 2012.

U. Bonavolontà, C. Bachmann, D. Coccorese, G. D. Gironimo, V. Imbriani, D. Marzullo, G. Mazzone, C. Vorpahl, and J.H. You. EU-DEMO divertor: Cassette design and PFCs integration at pre-conceptual stage. *Fusion Engineering and Design*, 159:111784, 2020. doi: 10.1016/j.fusengdes.2020.111784.

G. Mazzone, J.H. You, C. Bachmann, U. Bonavolontà, V. Cerri, D. Coccorese, D. Dongiovanni, P. Flammini, D.and Frosi, L. Forest, Giuseppe Di. G., Gennaro Di. M., V. Imbriani, A. Maffucci, D. Marzullo, Pietro Alessandro Di. M., M. T. Porfiri, E. Vallone, R. Villari, E. Visca, and C. Vorpahl. Eurofusion-DEMO Divertor - Cassette Design and Integration. *Fusion Engineering and Design*, 157:111656, aug 2020. ISSN 09203796. doi: 10.1016/j.fusengdes.2020.111656. URL `http://www.sciencedirect.com/science/article/pii/S0920379620302040https://linkinghub.elsevier.com/retrieve/pii/S0920379620302040`.

Eurofusion. Divertor cassette CAD model 2019. Technical report, 2019. URL `https://idm.euro-fusion.org/?uid=2NCUJX&version=v2.2%0A`.

J. H. You, G. Mazzone, E. Visca, H. Greuner, M. Fursdon, Y. Addab, C. Bachmann, T. Barrett, U. Bonavolontà, B. Böswirth, F. M. Castrovinci, C. Carelli, D. Coccorese, R. Coppola, F. Crescenzi, G. Di Gironimo, P. A. Di Maio, G. Di Mambro, F. Domptail, D. Dongiovanni, G. Dose, D. Flammini, L. Forest, P. Frosi, F. Gallay, B. E. Ghidersa, C. Harrington, K. Hunger, V. Imbriani, M. Li, A. Lukenskas, A. Maffucci, N. Mantel, D. Marzullo, T. Minniti, A. V. Müller, S. Noce, M. T. Porfiri, A. Quartararo, M. Richou, S. Roccella, D. Terentyev, A. Tincani, E. Vallone, S. Ventre, R. Villari, F. Villone, C. Vorpahl, and K. Zhang. Divertor of the European DEMO: Engineering and technologies for power exhaust. *Fusion Engineering and Design*, 175, 2022. ISSN 09203796. doi: 10.1016/j.fusengdes.2022.113010.

J. H. You, E. Visca, Ch Bachmann, T. Barrett, F. Crescenzi, M. Fursdon, H. Greuner, D. Guilhem, P. Languille, M. Li, S. McIntosh, A. V. Müller, J. Reiser, M. Richou, and M. Rieth. European DEMO divertor target: Operational requirements and material-design interface. *Nuclear Materials and Energy*, 9:171–176, dec 2016. ISSN 23521791. doi: 10.1016/J.NME.2016.02.005.

J. H. You, E. Visca, T. Barrett, B. Böswirth, F. Crescenzi, F. Domptail, M. Fursdon, F. Gallay, B. E. Ghidersa, H. Greuner, M. Li, A. V. Müller, J. Reiser, M. Richou, S. Roccella, and

Ch Vorpahl. European divertor target concepts for DEMO: Design rationales and high heat flux performance. *Nuclear Materials and Energy*, 16:1–11, aug 2018. ISSN 23521791. doi: 10.1016/J.NME.2018.05.012.

A. R. Raffray, J. Schlosser, M. Akiba, M. Araki, S. Chiocchio, D. Driemeyer, F. Escourbiac, S. Grigoriev, M. Merola, R. Tivey, G. Vieider, and D. Youchison. Critical heat flux analysis and RD for the design of the ITER divertor. *Fusion Engineering and Design*, 45(4):377–407, 1999. ISSN 0920-3796. doi: https://doi.org/10.1016/S0920-3796(99)00053-8. URL `http://www.sciencedirect.com/science/article/pii/S0920379699000538`.

J. Rosenfeld and J. Lindemuth. Evaluation of porous media heat exchangers for plasma facing components. *Proceedings - Symposium on Fusion Engineering*, 2:1210–1213, 1993. doi: 10.1109/fusion.1993.518540.

V. Kovalenko, V. Khripunov, A. Antipenkov, and A. Ulianov. Heat-pipes-based first wall. *Fusion Engineering and Design*, 27(C):544–549, 1995. ISSN 09203796. doi: 10.1016/0920-3796(95)90170-1.

G. A. Carlson and M. A. Hoffman. Heat pipes in the magnetic-field environment of a fusion reactor. *Journal of Heat Transfer*, 94(3):282–288, 1972. ISSN 15288943. doi: 10.1115/1.3449933.

N. L. Schwertz and M. A. Hoffman. Heat Pipe Concept for Cooling a Liquid-Pool Blanket of a Tandem Mirror Fusion Reactor. *Nuclear technology/fusion*, 4(3):479–490, 1983. ISSN 02723921. doi: 10.13182/FST83-A22797.

A. Makhankov, A. Anisimov, A. Arakelov, A. Gekov, N. Jablokov, V. Yuditskiy, I. Kirillov, V. Komarov, I. Mazul, A. Ogorodnikov, and A. Popov. Liquid metal heat pipes for fusion application. *Fusion Engineering and Design*, 42(1-4):373–379, 1998. ISSN 09203796. doi: 10.1016/S0920-3796(98)00216-6. URL `http://dx.doi.org/10.1016/S0920-3796(98)00216-6`.

P. Stephan. N5 Heat Pipes. In *VDI Heat Atlas*, pages 1503–1514. Springer, Berlin, Heidelberg, 2nd edition, 2010. ISBN 978-3-540-77877-6.

P. Norajitra, R. Giniyatulin, T. Ihli, G. Janeschitz, W. Krauss, R. Kruessmann, V. Kuznetsov, I. Mazul, V. Widak, I. Ovchinnikov, R. Ruprecht, and B. Zeep. He-cooled divertor development for DEMO. *Fusion Engineering and Design*, 82(15-24):2740–2744, 2007. ISSN 09203796. doi: 10.1016/j.fusengdes.2007.05.027.

T. Hirai, S. Panayotis, V. Barabash, C. Amzallag, F. Escourbiac, A. Durocher, M. Merola, J. Linke, Th Loewenhoff, G. Pintsuk, M. Wirtz, and I. Uytdenhouwen. Use of tungsten material for the

ITER divertor. *Nuclear Materials and Energy*, 9(2016):616–622, 2016. ISSN 23521791. doi: 10.1016/j.nme.2016.07.003. URL http://dx.doi.org/10.1016/j.nme.2016.07.003.

W. G. Anderson. Evaluation of heat pipes in the temperature range of 450 to 700 K. *AIP Conference Proceedings*, 746(July 1989):171–178, 2005. ISSN 0094243X. doi: 10.1063/1.1867132.

V. R. Barabash, G. M. Kalinin, S. A. Fabritsiev, and S. J. Zinkle. Specification of CuCrZr alloy properties after various thermo-mechanical treatments and design allowables including neutron irradiation effects. *Journal of Nuclear Materials*, 417(1-3):904–907, oct 2011. ISSN 00223115. doi: 10.1016/J.JNUCMAT.2010.12.158.

P. Norajitra, W. W. Basuki, R. Giniyatulin, C. Hernandez, V. Kuznetsov, I. V. Mazoul, M. Richou, and L. Spatafora. Recent Progress in the Development of Helium-Cooled Divertor for Demo. *Fusion Science and Technology*, 67(4):732–744, 2015. ISSN 19437641. doi: 10.13182/FST14-832.

V. Gnielinski. G7 Heat Transfer in Cross-flow Around Single Rows of Tubes and Through Tube Bundles. In *VDI Heat Atlas*, pages 725–729. Springer, Berlin, Heidelberg, 2nd edition, 2010. ISBN 978-3-540-77877-6.

T. Brahim and A. Jemni. Effect of the heat pipe adiabatic region. *Journal of Heat Transfer*, 136 (4), 2014. ISSN 00221481. doi: 10.1115/1.4025132.

N. H. Afgan, L. A. Jovic, S. A. Kovalev, and V. A. Lenykov. Boiling heat transfer from surfaces with porous layers. *International Journal of Heat and Mass Transfer*, 28(2):415–422, 1985. ISSN 00179310. doi: 10.1016/0017-9310(85)90074-2.

H.J. Kretzschmar and W. Wagner. *International Steam Tables*. Springer, Berlin, Germany, 3rd ed. edition, 2019. ISBN 9783662532171. doi: 10.1007/978-3-662-53219-5.

H. W. Coleman and W. G. Steele. *Experimentation, validation, and uncertainty analysis for engineers*. John Wiley Sons, Hoboken, N.J, 3rd ed edition, 2009. ISBN 0470168889; 9780470168882. URL https://swbplus.bsz-bw.de/bsz321464524cov.jpg.

JCGM106:2020. Guide to the expression of uncertainty in measurement - Part 6: Developing and using measurement models. *International Organization for Standardization Geneva*, JCGM GUM-6:1–103, 2020. URL https://www.bipm.org/en/publications/guides.

M. Wilhelm and S. Holger. G10 Impinging Jet Flow Heat Transfer. In 2.Edition, editor, *VDI Heat Atlas*, pages 745–751. Springer, Berlin, Heidelberg, 2010. ISBN 978-3-540-77877-6.

H. Martin. Heat and Mass Transfer between Impinging Gas Jets and Solid Surfaces. *Advances in Heat Transfer*, 13(C):1–60, jan 1977. ISSN 0065-2717. doi: 10.1016/S0065-2717(08)70221-1.

J. A. Weibel, S. V. Garimella, and M. T. North. Characterization of evaporation and boiling from sintered powder wicks fed by capillary action. *International Journal of Heat and Mass Transfer*, 53(19-20):4204–4215, sep 2010.

J. A. Weibel and S. V. Garimella. Visualization of vapor formation regimes during capillary-fed boiling in sintered-powder heat pipe wicks. *International Journal of Heat and Mass Transfer*, 55(13-14):3498–3510, 2012. ISSN 00179310. doi: 10.1016/j.ijheatmasstransfer.2012.03.021.

D. H. Min, G. S. Hwang, and M. Kaviany. Multi-artery, heat-pipe spreader. *International Journal of Heat and Mass Transfer*, 52(3-4):629–635, jan 2009. ISSN 00179310. doi: 10.1016/J.IJHEATMASSTRANSFER.2008.07.021.

D. Coso, V. Srinivasan, M.C. Lu, J.Y. Chang, and A. Majumdar. Enhanced Heat Transfer in Biporous Wicks in the Thin Liquid Film Evaporation and Boiling Regimes. *JOURNAL OF HEAT TRANSFER-TRANSACTIONS OF THE ASME*, 134(10), oct 2012. ISSN 0022-1481. doi: 10.1115/1.4006106.

P. C. Stephan and C. A. Busse. Analysis of the heat transfer coefficient of grooved heat pipe evaporator walls. *International Journal of Heat and Mass Transfer*, 35(2):383–391, 1992. ISSN 00179310. doi: 10.1016/0017-9310(92)90276-X.

D.X. Deng, Q.S. Huang, Y.L Xie, X. Huang, and X.Y. Chu. Thermal performance of composite porous vapor chambers with uniform radial grooves. *Applied Thermal Engineering*, 125: 1334–1344, oct 2017. ISSN 1359-4311. doi: 10.1016/J.APPLTHERMALENG.2017.07.108.

V. Guichet and H. Jouhara. Condensation, evaporation and boiling of falling films in wickless heat pipes (two-phase closed thermosyphons): A critical review of correlations. *International Journal of Thermofluids*, 1-2:100001, 2020. ISSN 26662027. doi: 10.1016/j.ijft.2019.100001. URL `https://doi.org/10.1016/j.ijft.2019.100001`.

J. A. Weibel and S. V. Garimella. Recent Advances in Vapor Chamber Transport Characterization for High-Heat-Flux Applications. *Advances in Heat Transfer*, 45:209–301, 2013. ISSN 00652717. doi: 10.1016/B978-0-12-407819-2.00004-9.

V. P. Carey. *Liquid Vapor Phase Change Phenomena: An Introduction to the Thermophysics of Vaporization and Condensation Processes in Heat Transfer Equipment, Third Edition*. Taylor & Francis, Boca Raton, USA, 2020. ISBN 9780429082221. doi: https://doi.org/10.1201/9780429082221. URL `https://www.taylorfrancis.com/books/mono/10.1201/9780429082221/liquid-vapor-phase-change-phenomena-van-carey`.

A. Faghri. Recent advances in the numerical analysis of heat pipes. *Computational Mechanics*, 14(5):480–491, 1994. ISSN 01787675. doi: 10.1007/BF00377600.

M. P. Mughal and O. A. Plumb. An experimental study of boiling on a wicked surface. *International Journal of Heat and Mass Transfer*, 39(4):771–777, 1996. ISSN 00179310. doi: 10.1016/0017-9310(95)00159-X.

Z. G. Qu, Z. G. Xu, C. Y. Zhao, and W. Q. Tao. Experimental study of pool boiling heat transfer on horizontal metallic foam surface with crossing and single-directional V-shaped groove in saturated water. *International Journal of Multiphase Flow*, 41:44–55, 2012. ISSN 03019322. doi: 10.1016/j.ijmultiphaseflow.2011.12.007.

D.H. Zhang, H.Y. Xu, Y. Chen, J. Wang, L.Q.and Qu, M.F. Wu, and Z.P. Zhou. Boiling heat transfer performance of parallel porous microchannels. *Energies*, 13(11), 2020. ISSN 19961073. doi: 10.3390/en13112970.

Appendix

A Impinging Jet Heat Sink and Condenser Design for Experimental Heat Pipe

To remove the power deposited on the Heat Pipe of the Evaporator Evaluation (HPEE), an external water-cooling circuit should has high heat transfer coefficient (HTC). The HTC of the coolant system for the DIV-HP is around 2.2e4 W/(m^2K) when coolant flows through the heat pipe bundles in a staggered arrangement. However, with a single heat pipe experiment, the temperature increase between the inlet and outlet of such a cooling setup is only 2 °C at the maximum heat flux. It results in a high relative uncertainty of the calorimetric power evaluation.

Due to the size constraints of the vacuum tank flange, the available cooling area for HPEE is limited to 3×10^3 mm^2 with a flat disc of 60.3 mm in diameter. It is close to the cooling area of a 200 mm long HP, around 35×10^3 mm^2.

To reduce the relative uncertainty in the calorimetric evaluation of the transported power, the temperature rise at the coolant inlet and outlet is controlled at 8 °C. Then the inlet coolant for the HPEE heat sink from the external cooling system of the KIT INR experimental hall is controlled at around 17 °C and 0.4 MPa by the pump system with a maximum flow rate of 600l/h. It means that the cooling method not only keeps the temperature rise at the inlet and outlet of the coolant high enough, but is also more efficient in cooling the HPEE so that the outer surface temperature of the HPEE condenser can be similar or even lower than that of the DIV-HP. Meanwhile, to keep the inner surface temperature of the HPEE condenser low as well, the thickness of the condenser is limited to a low value, according to the heat resistance estimate [Stephan 2010].

For such reasons, an impinging jet is an excellent choice. It provides high jet flow on the condenser surface, then flow back from an annular tube, ensuring the high temperature difference at the coolant inlet and outlet. Vertical coolant circulation in the impinging jet system also saves space so that it can go into the vacuum tank through the flange.

Three options are considered for jet arrangements [Wilhelm and Holger 2010]:

- only one single jet at center,
- square arrangement jet with four nozzles around,

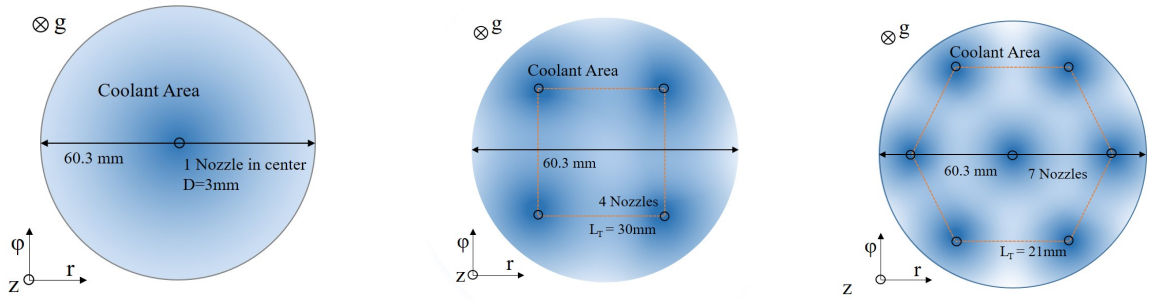

(a) (b) (c)

Figure A.1: Jet arrangement (a) single jet (b) four jet with rectangle arrangement (c) seven jet with triangle arrangement.

- triangle arrangement jet with seven nozzles with one at the center, as shown in Figure A.1:

As the heat sink influences the condenser temperature and the operation temperature (vapor temperature) through the effective heat resistance chain, the condenser surface and thickness have to be determined in the impinging jet design procedure.

A.1 Design of the Impingement Jet Heat Sink

The inlet coolant for the HPEE heat sink is controlled at around 17 °C and 0.4MPa by the pump system with a maximum flow rate of 1500 l/h. Considering the experimental requirements and system limits mentioned in the previous section, three jet arrangements are evaluated by taking into account the following aspects:

- The heat pipe operating (vapor) temperature at around 250 °C for the maximum heat flux (20 MW/m^2),
- Wall temperature is lower than 143.6 °C to avoid cooling water boiling at the condenser surface for pressures below 0.4MPa,
- Pressure losses at max: 0.1MPa (allowable pump system range).

The temperature distribution on the outer surface of the condenser is assumed to be uniform to avoid liquid condensing only on specific cold point on the inner condenser surface of the HPEE.

The four parameters for calculating the impingement jet's heat transfer coefficient are: D, the inner diameter of the nozzle; H, the distance between the nozzle and cooled surface; L_T, the distance between each nozzle, and Nn, the number of nozzles[Wilhelm and Holger 2010].

According to the impinging jet parameters optimization study from [Martin 1977], for getting a high heat transfer coefficient, the distance between the nozzle and cooled surface H can be seen as a constant with the optimum relation between the optimized parameters, where:

$$D_{opt} \approx 1/5H, \tag{A.1}$$

$$L_{T_{opt}} \approx 7/5H, \tag{A.2}$$

The average heat transfer coefficient α at the surface impinged upon by jets is defined as the heat flux divided by the difference between the fluid temperatures at the exit of the nozzle (N) and the surface (S) of the condenser, which is below the nozzle at a distance H:

$$\alpha = Q/(A(T_N - T_S)), \tag{A.3}$$

Meanwhile, the Nusselt number is a function of the the average heat transfer coefficient α, the inner diameter of the nozzle D, and thermal conductivity of the liquid λ:

$$Nu = \alpha D/\lambda, \tag{A.4}$$

From [Wilhelm and Holger 2010], for a single round nozzle (SRN), in order to estimate the integral heat transfer coefficient, the corresponding Nusselt number can be expressed as follows:

$$Nu_{SRN} = \frac{1 - \frac{1.1}{r^*}}{(r^* + 0.1(h^* - 6)} F(Re) Pr^{0.42}, \tag{A.5}$$

$$F(Re) = 2[Re(1 + 0.005Re^{0.55})]^{0.5}, \tag{A.6}$$

where $r^* = \frac{r}{D}$ and $h^* = \frac{H}{D}$, and F(Re) are power-law correlations in three different ranges of the Reynolds number $F = aRe^m$. And the dimensionless numbers:

$$Re = \frac{wD}{\nu} = \frac{4\dot{m}D}{\nu N_n \pi D^2}, \tag{A.7}$$

are Reynolds number as a function of the inner diameter of the nozzle D, the kinematic viscosity ν, and the velocity of the coolant out of the nozzles, which is calculated by flow rate of the heat

sink coolant, inner surface and the number of the nozzle: $w = (4\dot{m})/(N_n \pi D^2)$. The Prandtl number is a function of the kinematic viscosity ν and thermal diffusivity a.

$$Pr = \nu/a, \tag{A.8}$$

The Nusselt number for an array of round nozzles (ARN) is given by:

$$Nu_{ARN} = G * Re^{2/3} Pr^{0.42}, \tag{A.9}$$

$$G = \frac{d^*(1 - 2.2d^*)}{1 + 0.2(h^* - 6)d^*}[1 + (\frac{10h^*d^*}{6})^{\ 6}]^{-0.05}, \tag{A.10}$$

G is an empirical equation for integral average heat and mass transfer coefficients at the surface recommended by Polat. Here, $d^* = \sqrt{f}$, and f is the relative nozzle area, it can be found that $f = \frac{\pi D^2}{4L_T^2}$ for a square-shaped arrangement and $f = \frac{\pi D^2}{2\sqrt{3}L_T^2}$ for the triangle arrangement.

According to Equations A.3 and A.4, the condenser's outer surface temperature can be estimated with the known Nu_{SRN} or Nu_{ARN}, if a coolant temperature T_N =17 °C is assumed to:

$$T_{cond,o} = T_S = 17 + \frac{A_{evap}Q}{\alpha A_{cond}}. \tag{A.11}$$

The condenser's inner surface temperature $T_{cond,i}$ is the sum of the $T_{cond,o}$ and the temperature gradient through the condenser wall. Because the heat pipe is at the saturation state when it is working, assuming T_{vapor} equals to the condenser's inner surface temperature.

$$T_{cond,i} = T_{cond,o} + \frac{\delta_{cond}Q}{\alpha A_{cond}}. \tag{A.12}$$

where δ_{cond} is the thickness of the condenser envelope, λ is the thermal conductivity of the condenser material(CuZrZr), and A_{cond} is the area of the condenser.

A.2 Three Optional Impinging Jet Configurations

Based on the vacuum vessel used, a standard coolant tube (DN65) enters the vessel with an inner diameter of 70.3 mm. The area covered by the jet as the condenser surface has a diameter of 60.3 mm to guarantee high condenser coolant efficiency.

According to VDI heat Atlas [Kast 2010], the pressure loss caused by cross-section at the nozzle and condenser surface can be calculated as:

$$\Delta P = (1 - \frac{A_{nozzle}}{A_{cond}})^2 \frac{\rho v_{nozzle}^2}{2} = \frac{1}{2}\rho(\frac{\dot{V}_{coolant}^2}{A_{nozzle}} - \frac{\dot{V}_{coolant}^2}{A_{cond}}). \tag{A.13}$$

where $\dot{V}_{coolant}$ is the volume flow rate of the coolant, A_{cond} is the coolant area of the condenser and A_{nozzle} is the total nozzle area, which is influenced by the number of the nozzles Nn and D.

One single nozzle is arranged in the center of the coolant system just above the condenser. For the selected configuration (D = 4 mm, H= 20 mm), the calculated condenser outer surface temperature is 91 °C when heat flux is 20 MW/m^2. The heat transfer coefficient is 45969.4 W/(m^{2}K). However, the maximum pressure drop of a single nozzle arrangement is already 0.27MPa when the heat flux is 20 MW/m^2, exceeding the critical capacity of the coolant pump system.

Following the same procedure as for the single nozzle configuration, Table A.1 lists the HTC of the heat sink, the surface temperature of the outer condenser, and the pressure drop of the other two arrangements, the four nozzles with rectangular arrangement and the seven nozzles with triangle arrangements, with different inner diameter of nozzle.

Results in Table A.1 indicate that with D=4 mm, the condenser outer surface temperature is already close or even exceeds the boiling temperature limit of 143.7 °C for a heat flux of 20 MW/m^2, whether four-rectangle or seven-triangle arrangement. Hence, another 6 mm standard tube with a wall thickness of 1.5 mm with D=3 mm is planned to be used, resulting in H=15 mm and L_{Topt}=21 mm. Then, both arrangements with D=3 mm show that the condenser outer surface temperatures are well below the boiling temperature limit.

Table A.1: HTC and wall temperatures influenced by different nozzle diameter D in 7 nozzles jet arrangement.

D	Configurations	HTC of coolant [W/ (m^{2}K)]	Outer wall temperature [°C]	Pressure drop [Bar]
4	one single jet at center	45969.4	85.86	2.74
	square arrangement jet with four nozzles around	26018.57	138.66	0.17
	triangle arrangement jet with seven nozzles with one at the center	18481.74	188.27	0.056
3	square arrangement jet with four nozzles around	42025.67	92.32	0.54
	triangle arrangement jet with seven nozzles with one at the center	27495.26	130.78	0.18

However, there is no rectangle-shaped nozzle in the center of the condenser, where the HTC should be high enough to transfer heat from the vapor space. Hence, the final choice is the

triangle arrangement with seven nozzles D=3 mm. It can provide the most uniform temperature distribution on the condenser.

According to the calculation above, when seven nozzles with 3 mm inner diameter are used in impinging jet triangle arrangement, the outer condenser temperature is around 130 °C. Based on this value, the condenser inner surface temperature can be estimated with different condenser thicknesses, as presented in Figure A.2. It shows that when δ_{cond}=10 mm, the condenser inner surface temperature is around 215 °C at 20 MW/m^2. Meanwhile, to avoid liquid droplet accumulation on the inner side of the condenser, the condenser inside surface is added with a slight slope, so the final condenser thickness is 10 mm at the center and 2 mm thicker at the corner. The average of the condenser inner surface temperature, $T_{cond,i}$=224 °C.

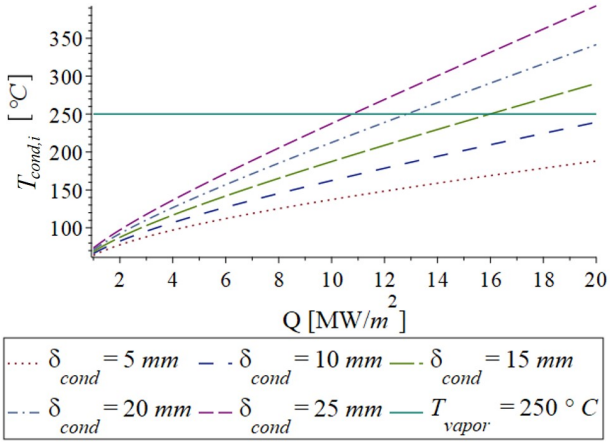

Figure A.2: Calculated inner condenser surface temperature as a function of the allied heat flux for different condenser wall thickness D=3 mm.

Figure A.3 indicates the influence of the diameter of the nozzles D and the distance between the nozzle and the condenser H on the condenser inner surface temperature.

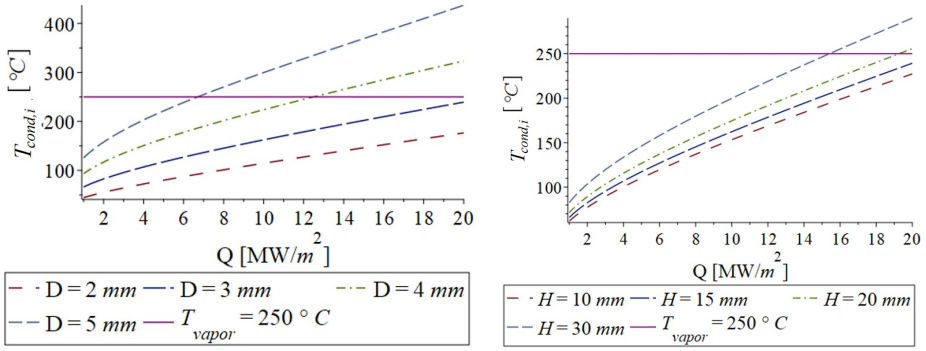

(a) (b)

Figure A.3: Calculated inner condenser surface temperature with δ_{cond}=10 mm as a function of the applied heat flux for (a)different nozzle diameters D and (b) for nozzle-condenser distance H.

It shows that the inner surface temperature exceeds 250 °C at 12 MW/m^2 when D = 4 mm, and D= 2 mm is so small for the coolant that it is easier to block. And the influence of H is not so obviously as the D.

The final heat sink system is implemented by an impinging jet featuring seven nozzles with a triangular arrangement, as shown in Figure A.4. The parameters are listed in Table A.2. And the condenser is fabricated of CuCrZr with a thickness of 10 mm and a 2 mm lower slope.

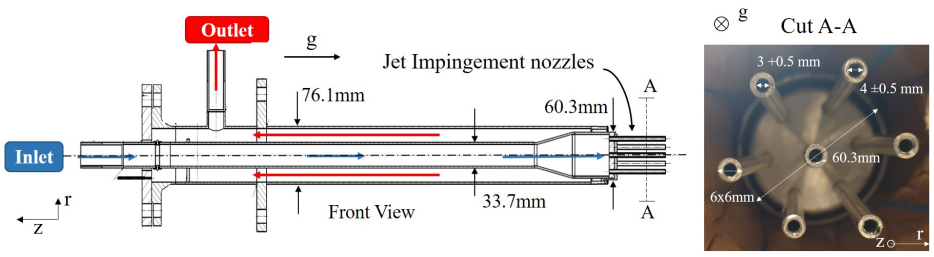

(a) (b)

Figure A.4: Impingement jet cooling system for HPEE (a) Jet cooling system with condenser surface (b) nozzles head finished.

Table A.2: Parameter of heat sink system with impinging jet.

Parameters	**Symbol**	**Value**
The outer diameter of the coolant pipe	$d_{coolant,o}$	76.1 mm
The inner diameter of the coolant pipe	$d_{cooalnt,i}$	60.3 mm
The thickness of the coolant box wall (steel)	$\delta_{coolant}$	4 mm
Number of jets	N_j	7
The inner diameter of the jet	D	3 mm
Distance between jet and bottom of HPEE	H	15 mm

Bibliography

W. Kast. L1.3 Pressure Drop in Flow Through Pipes of Changing Cross-section. In *VDI Heat Atlas*, pages 1065–1076. Springer, Berlin, Heidelberg, 2nd edition, 2010. ISBN 978-3-540-77877-6.

H. Martin. Heat and Mass Transfer between Impinging Gas Jets and Solid Surfaces. *Advances in Heat Transfer*, 13(C):1–60, jan 1977. ISSN 0065-2717. doi: 10.1016/S0065-2717(08)70221-1.

P. Stephan. N5 Heat Pipes. In *VDI Heat Atlas*, pages 1503–1514. Springer, Berlin, Heidelberg, 2nd edition, 2010. ISBN 978-3-540-77877-6.

M. Wilhelm and S. Holger. G10 Impinging Jet Flow Heat Transfer. In *VDI Heat Atlas*, pages 745–751. Springer, Berlin, Heidelberg, 2nd edition, 2010. ISBN 978-3-540-77877-6.

B Liquid Inventory of Experimental Heat Pipe and Filling Procedure

The operational heat flux applied on the DIV-HP significantly changes from 1 MW/m^2 to 20 MW/m^2. When applied heat flux increases, the temperature of the heat pipe increases, which changes the properties of the water and thickness of the condensed liquid film on the heat pipe wall. Hence, the total liquid volume in the heat pipe also changes, and the water inventory filled in the heat pipe operation differs [Guichet and Jouhara 2020].

The DIV-HP is a closed system, so the maximum amount of water should be filled in advance. However, the situation is different for the experiment mock-up HPEE since it intends to understand the operation of the evaporator, especially in a porous structure, and evaluate its performance as a function of the liquid inventory wetting the porous structure. If the mock-up is filled with liquid for the maximum loading of 20 MW/m^2, there is a risk that the liquid in excess gathers on top of the porous structure when the test starts from the low heat flux, creating a pool of water. This results in a pool boiling dominated operation over the evaporator like in a thermosyphon, rather than our intended goal - the boiling inside a porous structure.

As such, the testing strategy is to fill the mock-up progressively. Meanwhile, a reservoir containing the extra liquid in the heat pipe is necessary when heat flux changes during experiments. It sits between the condenser and evaporator just before the cylindrical part, with grooves on the wall to store the water-condensed surplus at low heat flux. While at high heat flux, a continuous liquid flow is ensured. The liquid volume variation because of the heat flux increasing decides the reservoir dimension depending on the heat flux. Assuming the liquid fills the porous structure and grooves, the main change of the liquid inventory of water (decided by water volume) depends on the condensed liquid film on the adiabatic and condenser wall and the vapor volume.

To calculate the amount of water needed for a specific heat flux, the water volume for the mock-up is divided into the following regions:

- The fully filled liquid volume in grooves and sintered porous ($H_{grooves}$ 20 mm);
- Vapor volume;
- Liquid film at the condenser and the adiabatic section varies with heat flux.

The last two volumes will change the amount of liquid water needed because the water properties are influenced by operating temperature and pressure at different heat fluxes.

B.1 Water Volume based on Heat Pipe Dimension and Film Thickness

B.1.1 The water volume in the capillary structure V_c

In HPEE, the capillary structure is combined with the grooves and sintered porous structure. There are 125 grooves with a length of 20 mm and a width of 0.3 mm. The depth of the groove is 0.65 mm with 0.5 mm plus a rounded end with a radius of 0.15 mm, as illustrated in Figure B.1 (a). The sintered porous disk has a diameter of 26.5 mm and a thickness of 2 mm, and the porosity is 0.47, as depicted in Figure B.1 (b).

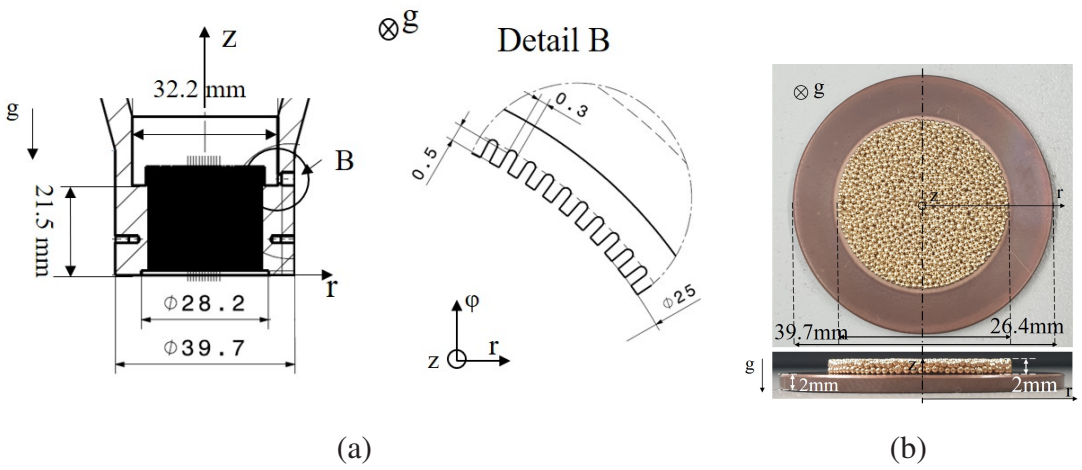

(a) (b)

Figure B.1: Dimensions of the capillary structures of HPEE-1 (a) grooves above the porous structure (b)sintered porous structure.

The total usable volume of the grooves is 487mm^3, and the volume of the sintered porous disk is 518mm^3. Assuming grooves and sintered porous are fully filled with liquid, the entire constant liquid volume in the capillary structure Vc is 1005 mm^3.

B.1.2 The water volume in vapor space V_{v-l}

The vapor volume V_{v-l} equals vapor space V_v subtracted from the volume covered by the liquid film on the condenser and the adiabatic sections, representing a tiny fraction compared with the

remaining vapor volume after it is extracted from the vapor space. Hence, the vapor volume is assumed to be the same as the vapor space, around 7.7x10^4mm^3.

During the operation, the vapor space is filled with vapor, whose density is lower than the liquid water and changes with vapor temperature. Therefore, according to the conservation of the mass, when the total liquid inventory of filling water is considered, the amount of vapor is transferred to the relative amount of liquid at the environment temperature (25 °C) during the filling procedure.

$$V_{v-l} = (V_v \rho_v(T_{operation}))/\rho_l(T_e). \tag{B.1}$$

B.1.3 The water volume V_f controlled by liquid film thicknesses

The liquid film thickness correlation according to the Nusselt number [Guichet and Jouhara 2020] is used:

$$\delta = (\frac{3}{4})^{\frac{1}{3}} (\frac{\eta_l^2}{\rho_l^2 g})^{\frac{1}{3}} Re_f^{\frac{1}{3}}, \tag{B.2}$$

$$Re_f = \frac{4\Gamma}{\eta_l}, \tag{B.3}$$

$$\Gamma = \frac{\dot{m}}{peri} = \frac{\dot{m}}{\pi D_i}. \tag{B.4}$$

Re_f: The falling film Reynolds number, which is usually given by Rohsenow[Rohsenow et al. 1998], Γ: the mass flow rate per unit periphery $\frac{\text{kg}}{ms}$ and η_l: the liquid dynamic viscosity (Pa s), where, $\dot{m} = \frac{Q}{\Delta h_v(T)}(\frac{\text{kg}}{\text{s}})$ is the mass flow rate of the falling film as a function of the applied heat flux Q (W) and enthalpy of vaporization Δh_v ($\frac{\text{J}}{\text{kg}}$). peri: the wetted perimeter (m), and D_i: the inner diameter of the HPEE(m), which changes with the height of the HPEE with the constant slope.

Besides the parameters above, the film thickness is a function of the average temperature of the inner condenser surface and the operational vapor temperature, which changes when heat flux differs. However, it is difficult to know the operational temperature, influenced by liquid film thickness on the condenser's inner surface. Hence, the liquid film thickness is simplified as a function of the temperature of the condenser's inner surface, estimated in Appendix C, and heat flux only. Figure B.2 presents the film thickness varies with the inner diameter of the HPEE under heat flux 1 MW/m^2 at the inner condenser surface's temperature of 62.5 °C until 20 MW/m^2 at the inner condenser surface's temperature of 220 °C.

It shows that the thinnest film is on the condenser part, where the $d_{cond,i}$ is 49 mm. Then, the film thickness increases from the condenser to the evaporator until $d_{cond,i}$ is 25 mm. The minimum and maximum thickness of the film with different heat flux is shown in Table B.1.

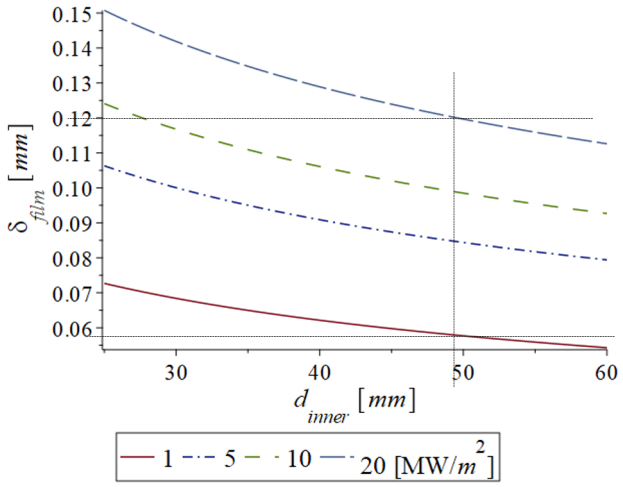

Figure B.2: Film thickness [m] as a function of the inner diameter of FHP (a) with heat flux (a) 1 MW/m^2 (62.5 °C), (b) with heat flux 20 MW/m^2 (220 °C).

Table B.1: Film thickness under different operation conditions and different diameter.

The inner diameter of HPEE [mm]	δ_{film} **at 1 MW/m^2 (62.5 °C) [mm]**	δ_{film} **at 20 MW/m^2 (220 °C) [mm]**
25	0.072	0.15
49	0.058	0.12

To simplify, the slight slope on the inner side of the condenser is ignored, and the film thickness is assumed to be constant on the flat inner condenser surface with a diameter of 49 mm and a surface area of 1885 mm^2. Hence, the liquid volume at the condenser surface (V_{fc}) is around 109.3 mm^3 at 1 MW/m^2 when a film thickness of 0.058 mm is considered, and it is around 226 mm^3 at 20 MW/m^2 when the thickness is 0.12 mm.

At the adiabatic part, the liquid film volume V_{la} is integrated by the variable film thickness δ and HPEE inner diameter d_i:

$$V_{fa} = \int_0^h \pi[(\frac{d_i}{2})^2 - (\frac{d_i}{2} - \delta)^2]dh + \delta\frac{\pi 52^2}{4} + \pi h_{cy}[(\frac{52}{2})^2 - (\frac{52}{2} - \delta)^2], \tag{B.5}$$

where both the film thickness δ and HPEE inner diameter d_i are related to the height of the HPEE, h_{cy}=56 mm in maximum, according to eq.B.2 to B.4, and slope relation $d_i = 2(\frac{25}{2} + \frac{52-25}{2*56} * h)$. The equation's first right part is the liquid volume in the adiabatic slope section, and the second part is the liquid volume in the cylindrical part.

Then, the total liquid film volume is the sum of V_{lc} and V_{la}, which equals 470mm^3 at 1 MW/m^2 and 940mm^3 at 20 MW/m^2. Both are far below the volume of vapor, justifying the assumption above.

Similar to the liquid inventory estimation of vapor volume, the liquid density varies when the operation temperature is different. The amount of the liquid calculated based on volume and properties at the high operating temperature must be transferred to the amount of liquid for filling at ambient temperature (25 °C):

$$V_l = [(V_c + V_{fc} + V_{fa}) * \rho_l(T_{cond,en,i})]/\rho_l(T_e), \tag{B.6}$$

The total liquid inventory of the water in the HPEE are :

$$V_{total} = V_{v-l} + V_l. \tag{B.7}$$

Table B.2 lists the condensed liquid volume and corresponding condensed liquid mass in the heat pipe based on the inner side condenser's temperature when applying different heat flux. The last column presents the liquid inventory filled in HPEE at an ambient temperature of 25 °C for different heat fluxes and operating conditions. It indicates that the condensed liquid volume for 20 MW/m^2 is higher than 1 MW/m^2. Hence, when the water amount filled in the heat pipe is used for 20 MW/m^2, a liquid reservoir in the HPEE is necessary to contain extra condensed liquid when the applied heat flux is low at 1 MW/m^2.

Table B.2: Liquid volume (change with heat flux input).

Applied Heat flux [MW/m^2]	**Condenser's inner surface Temperature [°C]**	**Liquid volume [ml]**	**Liquid mass [g]**	**Vapor mass [g]**	**Total mass [g]**	**Total water amount [ml] (filled at 25 °C)**
1	62	1.54	1.52	0.01	1.53	1.53
2	77	1.65	1.60	0.02	1.62	1.62
3	89	1.71	1.65	0.03	1.68	1.68
4	99	1.76	1.68	0.04	1.72	1.73
5	109	1.80	1.71	0.06	1.77	1.77
10	150	1.92	1.77	0.19	1.96	1.97
20	220	2.12	1.79	0.86	2.65	2.65

B.2 Dimension of Reservoir for Containing Extra Liquid

The liquid volume difference decides the liquid reservoir's dimension between 1 MW/m^2 and 20 MW/m^2 because the properties of the water and thickness of the liquid film on the heat pipe wall changes when applied heat flux increases. For example, at 1 MW/m^2, the total water liquid volume in the HPEE is around 1546 mm^3 (when the inner side condenser's temperature is 62 °C). At 20 MW/m^2, a liquid volume is around 2124 mm^3 (when the inner side condenser's temperature is 220 °C), so the maximum liquid volume difference is around 580 mm^3.

As shown in Figure B.3, the inner diameter of the reservoir is 26.2 mm, and the reservoir is extended to the wall with the proper width. Table B.3 lists the different outer diameters, widths, depths, and volume space for extra liquid:

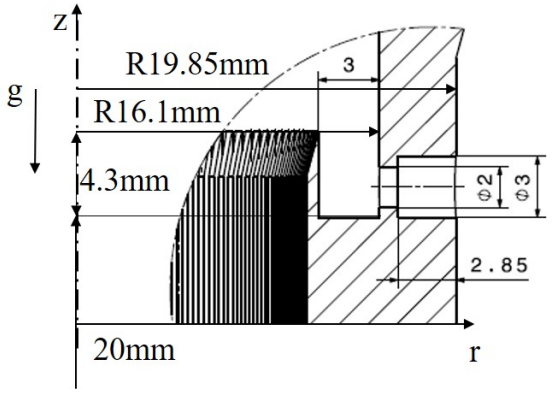

Figure B.3: Section view of Flat Heat Pipe's liquid reservoir (with a width 1 mm).

Table B.3: Different outer diameters and space for extra liquid with different widths and depth.

Width for reservoir	The outer diameter of the reservoir	Depth of reservoir	Volume (mm^3)
1 mm	28.2 mm	2.5 mm	213.5
2 mm	30.2 mm	2.5 mm	442.7
3 mm	32.2 mm	2.5 mm	687.7
3 mm	32.2 mm	3 mm	825.2

Finally, the reservoir's width and depth are 3 mm, and the outer diameter of the reservoir is 32.2 mm, which can contain liquid 825.2 mm^3.

B.3 Liquid Inventories Filled stepwise with Specific Heat Flux Range and Filling Procedure

Different from the condensed liquid volume in the heat pipe that only considers the water properties at specific applied heat flux and temperature, the water liquid inventory is the water amount filled in the heat pipe for different heat fluxes transferred into the one at the ambient temperature (25 °C), shown in the last column of Table B.2. It indicates that the liquid inventory for 20 MW/m^2 is almost twice as large as for higher than 1 MW/m^2. If the experiment is started from the low heat flux, filling the HPEE directly with the high liquid inventory for 20 MW/m^2 is unnecessary. Hence, besides the reservoir for flooding prevention, the water amount is filled in the HPEE three times, corresponding to three heat flux ranges. The first filling liquid volume is 1.5 ml, suitable for the heat flux until 1 MW/m^2. Then, the total liquid inventory is increased to 1.8 ml in the second round for heat flux from 1 to 5 MW/m^2. At the last round, the liquid inventory is 2 ml for heat flux 5-20 MW/m^2.

Furthermore, after the filling procedure, there is always 0.2 ml liquid that stays in the filling tube of the HPEE. This amount does not change as the filling tube's temperature is always around 25 °C. Hence, except for the liquid inventory corresponding to the different heat flux, 0.2 ml more liquid should be filled in the HPEE the first time. The heat flux range and their liquid inventories are listed in Table B.4.

Table B.4: heat flux range with the corresponding required liquid inventories.

heat flux range [MW/m^2]	**Liquid inventory [ml]**	**Water amount in HPEE [ml]**
0	0	0.2 in the tube
0-1	1.5	1.7
1-5	1.7	1.9
5-20	2.0	2.2

Unlike other heat pipe experiments, which fill the heat pipe only once, experiments for HPEE require a flexible filling system to realize the tests with various liquid inventories in the same mock-up. For example, the HPEE is initially filled with the lowest water inventory and tested, then experiments are conducted. After that, the liquid inventory is increased twice. Hence, the filling pipe is no mechanically closed through brazing or welding but sealed with a valve instead.

The HPEE is evacuated with pump with final pressure of 30Pa. The syringe used for injecting liquid in the HPEE is from Company Hamilton with a range of 2.5 ml and accuracy 0.05 ml, as in Figure B.4.

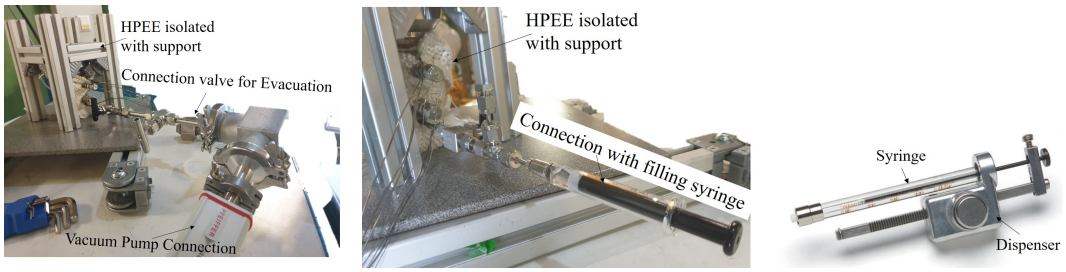

Figure B.4: HPEE filling setup: (a) evacuation with a vacuum pump; (b) filling with the syringe, (c) the PB600-1 Repeating Dispensers from Hamilton Company.

A PB600-1 repeating dispenser with an assembled syringe, which consistently dispenses samples up to 50 times with the push of a button, controls the filled liquid with higher accuracy. A 2.5 ml syringe can push 50 μl into the HPEE each time with this dispenser.

The filling procedure uses the desalinated and purified water as a working liquid. Before filling the mock-up with purified water, the air inside the HPEE is evacuated using a vacuum pump. The detailed evacuation and filling steps are explained as follows in Figure B.5 and Figure B.6.

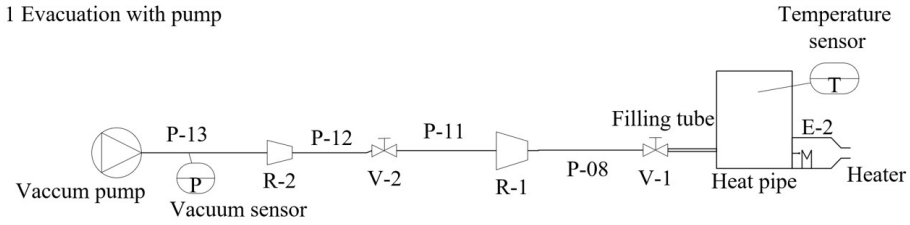

Figure B.5: PI&D diagram of water filling procedure-evacuation.

Install the heat pipe at a stable support setup (coolant tube).

1. Washing the valves and tubes with alcohol. Make sure each valve works well (leakage test)
2. Connect one end of valve V1 to the filling tube. Another end with 3 mm pipe (P-08).
3. Connect 10 mm pipe P-11 with valve V2 and pipe P-08 with the adapter R-1.
4. Then the valve V2 is connected to the vacuum pump with pipe P-12 and adapter R-2.
5. Check all valves' condition: open/ close.
6. Wash the HPEE by Helium at 3 bars to first push the air in HPEE out. (Helium is lighter than air, which will be easier to evacuate)
7. Heat the heat pipe to the operating temperature around 200 °C (attention has been paid to avoid increased thermal stress due to the non-uniform temperature ramp).

8. Open V1, V2. Evacuate the heat pipe and filling tube while the heat pipe is heated.
9. Close valves V1, V2. Remove the vacuum pump and reducer R-1 on pipe P-08. Keep the heater running.

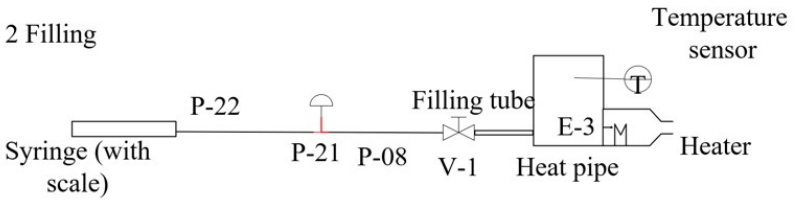

Figure B.6: PI&D diagram of water filling procedure-filling with the syringe.

1. Absorb the purified water into the syringe, avoiding air inside the syringe.
2. Connect the filled syringe with one end of the T-junction with the cap.
3. Connect another end of the T-junction to pipe P-08, check again that valve V1 is closed.
4. Open cap on T-junction, push the water in the syringe (with volume 2.5 ml and accuracy 0.05 mm) until seeing the liquid flows out from the T-junction cap.
5. Push the extra liquid out of the syringe so that the syringe only contains the proposed liquid volume for HPEE. Ensure the gas goes out, and close the cap on the T-junction.
6. Open valve V1 and push the water at the proposed volume in the syringe flowing through the filling tube to the HPEE.
7. close the valve V1, move the pipe P-08.

The HPEE is heated during the entire filing procedure to avoid liquid freezing at vacuum conditions. With such a high heating temperature, when the liquid goes into the HPEE, it will saturate immediately, producing a high pressure. It prevents more water from being added inside. If this happens, the heating temperature can be reduced a little. Steps 11 to 20 are repeated in the procedure above without heating the HPEE to put more water into the mock-up.

Because the HPEE is not heated in the repeat filing procedure, the pressure in the HPEE is low at ambient temperature. As soon as valve 1 is opened in step 10, bubbles appear in the syringe immediately because the liquid in the syringe is absorbed by HPEE directly. Due to this problem, when injecting the liquid more to 1.7 ml for HPEE-2, more liquid left in the syringe is absorbed in the HPEE with an uncertainty of 20%. That's why the syringe contains only the necessary water inventory before opening the valve afterward. Although many methods are used to avoid air remaining in HPEE, like flushing with Helium and evacuating, it might still exist in the small corner of the syringe or filing tube and valve.

B.4 Liquid Inventories Correction based on the Experimental Results

It has been found that the actual inner condenser surface's temperature and operation temperature during the experiment are higher than the inner condenser surface's temperature estimated in Appendix C. Hence, the corresponding liquid inventory estimated is lower than the experiment requirements. Table B.5 compares the difference between the estimated liquid inventories based on the inner surface condenser's temperature and the experiment's vapor temperature.

Table B.5: Liquid volume correction with the experimental results (change with heat flux input).

Applied Heat flux [MW/m^2]	Condenser's inner surface Temperature [°C]	Total water amount [ml] (filled at 25 °C)	Experimental operation Temperature [°C]	Liquid needed [ml] (filled at 25 °C)	Error
1	62	1.53	75	1.50	2%
2	77	1.62	128	1.58	2.5%
3	89	1.68	156	1.70	1.2%
4	99	1.73	187	1.92	9.9%
5	109	1.77			

It can be seen that the liquid input based on the inner surface condenser's temperature is lower than needed in experiments. However, the difference is small. 2.0 ml is enough for HPEE to work with 4MW/m^2. Even though the liquid inventory in the HPEE is lower, the HPEE still performs better than expected in the experiment.

Bibliography

V. Guichet and H. Jouhara. Condensation, evaporation and boiling of falling films in wickless heat pipes (two-phase closed thermosyphons): A critical review of correlations. *International Journal of Thermofluids*, 1-2:100001, 2020. ISSN 26662027. doi: 10.1016/j.ijft.2019.100001. URL https://doi.org/10.1016/j.ijft.2019.100001.

W. M. Rohsenow, J. P. Hartnett, and Y. I. Cho. *Handbook of Heat Transfer*. McGraw-Hill handbooks. McGraw-Hill Education, 1998. ISBN 9780070535558. URL https://books.google.de/books?id=M3pUAAAAMAAJ.

C The Analytic Model for Heat Pipe of Evaporator Evaluating

According to the known coolant temperature $T_{coolant}$ and the heat transfer coefficient of the impinging jet heat sink and HPEE's condenser design, the condenser's outer surface temperature $T_{en,o,cond}$ is calculated.

$$T_{en,o,cond} = T_{coolant} + P * h_{heatsink}. \tag{C.1}$$

With the known reference $T_{en,o,cond}$, the temperature chain of the HPEE can be predicted in the analysis model following the direction: condenser thermocouples' position, the condenser's inner surface, vapor, and evaporator temperature, by using the same analysis procedure and methodologies for the DIV-HP's temperatures estimation. This analysis model uses the HPEE's effective thermal resistance [Stephan 2010] with a specific heat flux to calculate the temperature chain, and the radial heat losses are assumed to be zero. The estimated temperatures are compared with the experiment results.

As presented in Figure C.1, due to the complexity of the HPEE structure, to calculate the effective heat resistance along the temperature chain, the HPEE is divided into eight parts.

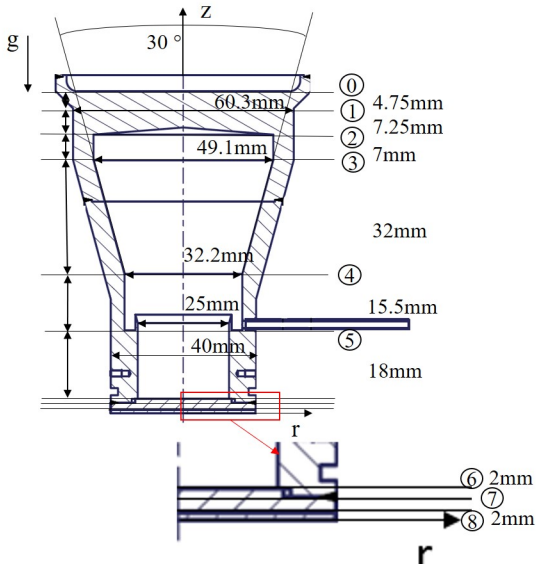

Figure C.1: Dimensions of the HPEE in eight effective thermal resistance parts.

The effective heat resistances obtained from Fourier's law $P = -\lambda A \frac{dT}{dz}$ are listed in Table C.1, where P is power, λ is the heat conductivity of the material and z is the distance of the axial direction. A is the heat transport surface related to the diameters of the HPEE's different parts.

Table C.1: The effective heat resistance formula in eight heat resistance parts.

Parts	Effective heat resistance [°C/W]	Explanations
0-1	$R_{01} = \frac{z_{01}}{\lambda_{en}\frac{\pi d_{cond}^2}{4}}$,	Cylindrical part 0-1, not included in the $T_{evap-cond}$ evaluation, because of the condenser thermocouple position, z_{01}=7 mm, and d_{cond}=60.3 mm
1-2	$R_{12} = \frac{z_{12}}{\lambda_{en}\frac{\pi d_{cond,out}^2}{4}}$,	Cylindrical part 12 with a diameter of d_{cond} =60.3 mm and a simplified thickness z_{12}=7 mm due to a conical inner surface
2-3	$R_{23} = \frac{z_{23}}{\lambda_{en}\frac{\pi d_{cond,out}^2 - d_{cond,in}^2}{4}}$,	Cylindrical cell part 2-3 with height z_{23}=7 mm and an outer diameter $d_{cond,out}$ =60.3 mm and inner diameter $d_{cond,in}$ = 49.1 mm.
3-4	$R_{34} = \int_0^{z_{34}} \frac{1}{\lambda_{en}\frac{\pi d_{adia,out}(z_{34})^2 - d_{adia,in}(z_{34})^2}{4}} dz_{34}$,	Conical cell part 3-4 with height z_{34}=32 mm, and shortest outer diameter 42 mm and shortest inner diameter 32.2 mm. The diameter increased with height z as $d_{adia,in} = 0.032 + 2 * 0.26 * z_{34}$, and $d_{adia,out} = 0.042 + 2 * 0.26 * z_{34}$, according to the conical angle tan (15°) =0.26
4-5	$R_{45} = \frac{z_{45}}{\lambda_{en}\frac{\pi d_{evap,out}^2 - d_{reservior}^2}{4}}$,	Cylindrical cell part 4-5 with height z_{45}=15.5 mm and an outer diameter $d_{evap,out}$ =40 mm and a simplified inner diameter $d_{reservoir}$ = 32 mm.
5-6	$R_{56} = \frac{z_{56}}{\lambda_{en}\frac{\pi d_{evap,out}^2 - d_{evap,in}^2}{4}}$,	Cylindrical cell part 5-6 with height z_{56}=20 mm and an outer diameter $d_{evap,out}$ =40 mm and a inner diameter $d_{evap,in}$ = 25 mm.
6-7	$R_{67} = \frac{z_{67}}{\lambda_{porous}\frac{\pi d_{porous}^2}{4}}$,	Cylindrical part 6-7 with a diameter of porous structure d_{porous} = 25 mm and a thickness z_{67}=2 mm for HPEE-1. (1.5 mm assumed got HPEE-2). It is ignored in the conductivity-only model, as it transports heat in parallel with parts 5-6 with little influence
7-8	$R_{78} = \frac{z_{78}}{\lambda_{en}\frac{\pi d_{evap,out}^2}{4}}$.	Cylindrical part 7-8 with a diameter of porous structure $d_{evap,out}$ = 40 mm and a thickness z_{78}=2 mm.

The heat pipe has two heat transfer modes. When there is no evaporation and condensation behavior in the HPEE, the heat is only transferred by the conduction of the heat pipe's CuCrZr wall. Otherwise, the heat is mainly transferred by evaporation and condensation of the 2-phase flow loop in the heat pipe, where the vapor temperature is assumed to be uniform from the condenser side to the evaporator.

To analyze the heat pipe heat transfer capability in the experiment, the analysis model evaluates the temperature difference between the condenser sensors at position '1' and the evaporator sensors at position '8' $T_{evap-cond}$ in both heat transfer modes. With the heat conduction-only mode, $T_{evap-cond}$ is the temperature chain from parts 1-8, while with evaporation and condensation mode, the temperature from parts 2-6 is uniform.

C.1 Heat Conductivity Only Model

When there is no evaporation or boiling behavior activated, the heat is considered to be transported axially through the evaporator, the adiabatic section wall, and the condenser envelope. Because the thermocouples for measuring condenser temperature are 4.75 mm below the condenser outer surface, and the thermocouples for measuring evaporator temperature are inserted on a tungsten protecting plate, sitting under evaporator CuCrZr plate, the corresponding $T_{evap-cond}$ is accounted by parts 1-8.

According to the effective heat resistance listed in Table C.1, the temperature difference between the condenser sensors and the evaporator sensors is given by

$$T_{evap-cond,conduct,only} = P * (R_{12} + R_{23} + R_{34} + R_{45} + R_{56} + R_{78}). \tag{C.2}$$

in which R_i denotes the heat resistances of the individual parts.

C.2 Heat Pipe Evaporation-Condensation Model

The temperature chain of the HPEE with evaporation-condensation behavior is also estimated based on effective heat resistance in Table C.1. However, because of the evaporation-condensation 2-phase flow in the heat pipe, vapor reaches its saturation state, and the vapor temperature in the HPEE is quasi-uniform in the entire vapor space. For simplification, the vapor temperature is

taken constant in the axial direction from parts 2-6. It is assumed to be equal to the interface temperature between the vapor and the condensed liquid that covers the inner condenser surface:

$$T_{vapor} = T_{v-l,cond} = T_{en,i,cond} + P * R_{liquid-film}. \tag{C.3}$$

where $R_{liquid-film}$ is the heat resistance of the condensed liquid film.

The outer evaporator surface temperature can also be estimated because the vapor temperature equals the vapor-porous interface temperature of the evaporator. Table C.2 lists the temperature formula from the condenser's outer surface $T_{en,o,cond}$ to the evaporator where thermocouples are installed.

Table C.2: The estimated evaporator, vapor, and condenser temperature formula in evaporation-condensation conditions.

Position	**Formula**	**Conditions**
$T_{en,o,cond}$	$T_{coolant} + P * h_{heat-sink}$,	Estimated condenser's outer surface temperature considering heat transfer coefficient of the heat sink
$T_{cond,sensor}$	$T_{en,o,cond} + P * R_{01}$,	Estimated temperature at condenser thermocouple position referred with condenser's outer surface temperature
$T_{en,i,cond}$	$T_{cond,sensor} + P * R_{12}$,	Estimated temperature of condenser's inner surface.
T_{vapor}	$T_{en,i,cond} + P * + R_{liquid-film}$,	Assuming vapor temperature is uniform, close to vapor-liquid interface temperature
T_{evap}	$T_{vapor} + P * (R_{67} + R_{78})$.	Assuming vapor temperature is uniform until the interface of the vapor and the evaporator's porous structure, and evaporator temperature increases because of the heat conductivity of the porous and Cu-CrZr plate.

In evaporation-condensation mode, the temperature difference between the condenser sensors at position '1' and the evaporator sensors at position '8' $T_{evap-cond}$ is:

$$T_{evap-cond} = T_{evap} - T_{cond} = P * (R_{12} + R_{liquid-film} + R_{67} + R_{78}). \tag{C.4}$$

C.3 Temperature Evaluation of the different Porous Material with Analytic Model

The porous material used in HPEE is bronze, while the porous material used in DIV-HP is copper, which has higher heat conductivity. Hence, the temperature of two evaporators with different capillary structures, B200 and C120, is then estimated based on the same vapor temperature, calculated with equation C.3. The effective heat conductivity of B200 is 26.8W/(mK) with the equation in [Stephan 2010] and the heat conductivity of Bronze in [Engineering ToolBox]. The heat conductivity of CuCrZr and copper follows the function of EUROFusion [EUROfusion].

Figure C.2 shows the calculated vapor temperature, the interface temperature between the porous structure and the evaporator, and the temperature of the evaporator's outer surface as a function of the applied heat flux. They indicate that the evaporator temperature increases more when the capillary structure uses B200 than when using C120 when applied heat flux increases. The evaporator temperature with B200 has already reached 450 °C, close to the temperature limitation of CuCrZr at 4 MW/m^2. While with capillary structure C120 in Figure C.2(b), the maximum evaporator temperature is around 250ºC at a heat flux of 4 MW/m^2, showing a much better performance. T

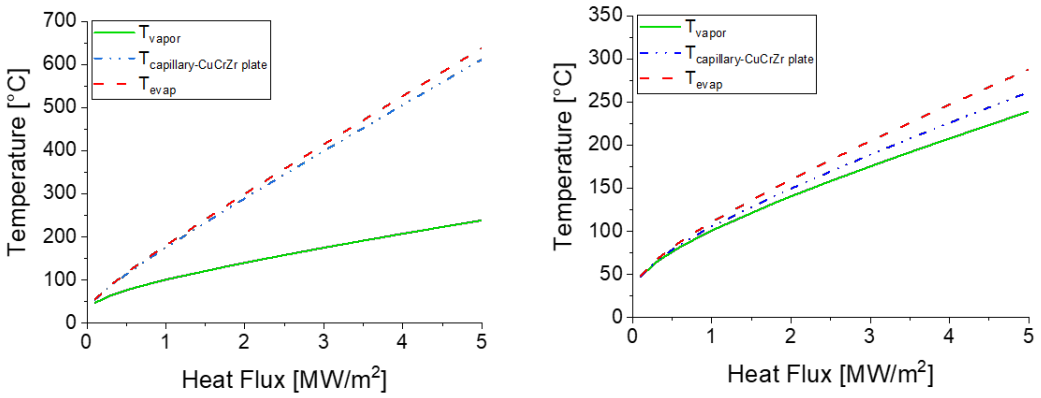

Figure C.2: Calculated capillary structure and evaporator surface temperature as a function of applied heat flux for the initial design model and different porous materials, (a) with B200;(b) with C120.

It finds that for B200 until 5 MW/m^2, the vapor temperature is already around 200 °C, and the evaporator temperature is high. It is not a big issue for B200 because the experiment ends at 4 MW/m^2. But if experiments want to go further with heat flux until 20 MW/m^2, the vapor temperature will increase rather quickly. Hence, the coolant heat sink and the condenser thickness must be optimized.

Bibliography

Engineering ToolBox. Thermal conductivities of common metals, metallic elements aand alloys. URL https://www.engineeringtoolbox.com/thermal-conductivity-metals-d_858.html.

EUROfusion. Material Property Handbook: CuCrZr. pages 1–83.

P. Stephan. N5 Heat Pipes. In *VDI Heat Atlas*, pages 1503–1514. Springer, Berlin, Heidelberg, 2nd edition, 2010. ISBN 978-3-540-77877-6.

D Calibration before Experiments

Before starting to test the mock-up, the calorimetric power is evaluated without heating power applied on the mock-up. It showed a regular oscilation on coolant temperature inlet and outlet, as it can be seen in Figure D.1 (a). These oscillations are rather regular, and the evaluated power exhibiting a sharp increase followed by a drop almost each 21 minutes, although there is no power applied. After looking in detail at the experimental set-up, it turned out that the fluctuations are caused by the changes in the hall cooling system temperature. This system is set to run following a certain hysteresis: the chiller(which is acting as a thermal sink) becomes active when the temperature reaches 18 °C and stops cooling when the temperature drops to 15 °C. Since the experiment cooling loop and the hall circuit are interfaced through a small heat exchanger, this results in an oscillation of about ± 1 °C of the water temperature.

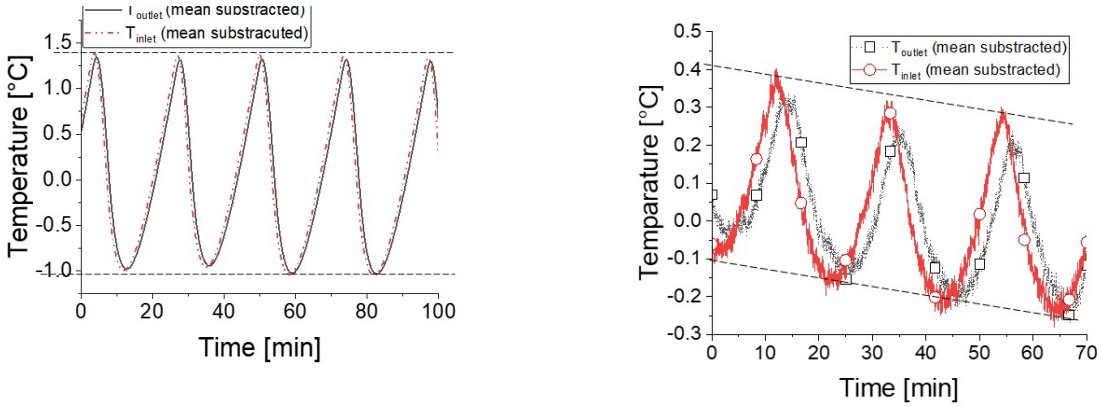

(a) (b)

Figure D.1: Measured temperature evolution of the heat sink inlet/outlet temperature with power 0W (a) initial value with dummy mock-up (b) optimized value with heat pipe mock up after implying a buffer tank, the mean value has been subtracted to put in evidence the amplitude of the oscillations.

To reduce the fluctuations in the temperature of the input water, the (plate) heat exchanger connecting the water loop to the (external) hall cooling circuit has been replaced by a thermal buffer, as shown in Figure 3.16 in Chapter 3 between the hall cooling system and the water loop for the mockup, the loop coolant (water) flowing now through a 300L tank, the heat being removed by

a spiral winding connected to the hall heat sink. This is intended damp the temperature oscillations and reduce the temperature fluctuations at the inlet of test setup.

In Figure D.1 (b), one can see that, after adding the water buffer, the amplitude of the temperature oscillations is reduced from ±1 °C to ±0.2 °C by a factor of 0.2. The average temperature reduction is caused by the external coolant machine, which cools the water in the buffer continuously.

As the flow rate through the cooling system changes, the time lag changes as well. By estimating the length of the heat sink's coolant flow path as shown in Figure D.2, the duration for one particle to pass through form the inlet to the outlet is assumed with different flow rate with equation D.1.

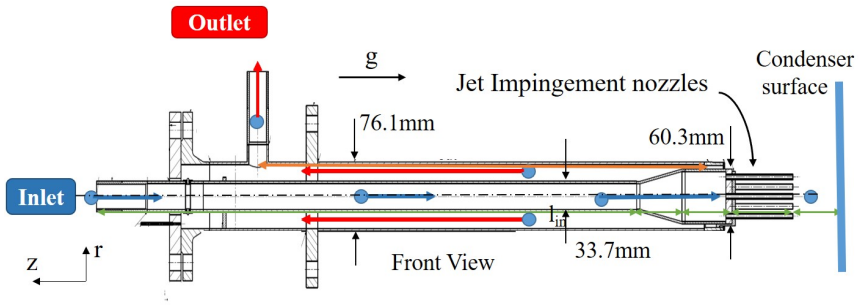

Figure D.2: Heat sink cooling loop dimensions.

$$t = l_{in}/v_{in} + l_{out}/v_{out}. \tag{D.1}$$

From the drawing, the length of the inlet part l_{in} is 1008.5 mm, and the length of the outlet part l_{out} is 832.5 mm. and the velocity of the inlet part $v_{in} = \dot{V}/A_{in}$ = 44 mm/s, and the velocity of the outlet part $v_{out} = \dot{V}/A_{out} - A_{in}$ = 9.3 mm/s. The results is listed in Table D.1.

Table D.1: Caculated time lag of the measurements at coolant inlet and outlet.

Flow rate l/h	**calculated time lag dt_{loop} [s]**
100	102.86
200	51.43
300	34.29
400	25.72
500	20.57

List of Figures

List of Tables

List of the publications

Articles

1. W. Wen, B. E. Ghidersa, W. Hering, J. Starflinger, and R. Stieglitz, “Heat pipe technology based divertor plasma facing component concept for European DEMO,” Fusion Eng. Des., vol. 164, 2021, doi: 10.1016/j.fusengdes.2020.112184.
2. W. Wen, B.-E. Ghidersa, W. Hering, J. Starflinger, and R. Stieglitz, “Heat Pipe-Based DEMO Divertor Target Concept: High Heat Flux Performance Evaluation,” J. Nucl. Eng., vol. 4, no. 1, pp. 278–296, 2023, doi: 10.3390/jne4010021.
3. W. Wen, B.-E. Ghidersa, W. Hering, J. Starflinger, and R. Stieglitz, “Experimental investigation of a porous evaporator for a Heat Pipe-based DEMO Divertor Target concept”, IEEE Transactions on Plasma Science (TPS), pages 1–6, 2024, doi: 10.1109/TPS.2024.3371572.

Posters

1. Heat pipe technology based divertor plasma facing component concept for European DEMO. 31st Symposium on Fusion Technology (SOFT2020), Virtual Edition, (September 2020).
2. Heat Pipe-Based DEMO Divertor Target Concept: High Heat Flux Performance Evaluation. 32nd Symposium on Fusion Technology (SOFT2022), Dubrovnik, Croatia, (September 2022).
3. Experimental investigation of operating limits of a porous evaporator for a Heat Pipe-based DEMO Divertor Target concept. 30th IEEE Symposium on Fusion Engineering (SOFE2023), Oxford, UK, (July 2023).

Acknowledgements

I would like to express my sincere gratitude to all those who have contributed to the completion of this doctoral dissertation.

First and foremost, I would like to express my deepest gratitude to my late supervisor, Prof. Dr.-Ing. Robert Stieglitz (†) for his unwavering support and invaluable guidance. His expertise and insight have been instrumental in shaping the direction of my work, which will forever inspire my journey forward.

I am deeply thankful to Prof. Dr.-Ing. Xu Cheng for stepping in and providing invaluable guidance and support during the final stages of my research.

I am also grateful to Prof. Dr.-Ing. Jörg Starflinger for agreeing to be the co-examiner on my doctoral committee, his constructive feedback and valuable suggestions have significantly enriched the quality of this dissertation.

Heartfelt thanks to my technical supervisor, Dr.-Ing. Bradut-Eugen Ghidersa who has shared his insights, ideas, and encouragement, as well as my colleges who works with me, creating a stimulating intellectual atmosphere.

Special thanks go to the EUROfusion Consortium Programme and KHYS for providing financial support during my doctoral studies. Then, I would like to acknowledge the Karlsruhe Institute of Technology (KIT) and the Institute for Neutron Physics and Reactor Technology (INR) for providing a conducive research environment and access to resources essential for the successful completion of this study.

My gratitude extends to my family for their unwavering support, understanding, and patience during the challenging phases of this academic endeavor. Your love and encouragement have been my strength.

Lastly, I want to express my appreciation to all the participants who generously contributed their time and insights to this study. Without their cooperation, this research would not have been possible.

In conclusion, this dissertation is the culmination of the efforts and support of many individuals and organizations, and I am sincerely grateful to each and every one of them.